



US Department  
of Transportation

**Federal Railroad  
Administration**

# **Engineering Studies on Structural Integrity of Railroad Tank Cars Under Accident Loading Conditions**

---

Office of Research and  
Development  
Washington, DC 20590

NOTICE

This document is disseminated under the sponsorship of the Department of Transportation in the interest of information exchange. The United States Government assumes no liability for its content or use thereof.

NOTICE

The United States Government does not endorse products or manufacturers. Trade or manufacturers' names appear herein solely because they are considered essential to the object of this report.

REPORT DOCUMENTATION PAGE			Form Approved OMB No. 0704-0188	
Public reporting burden for this collection of information is estimated to average 1 hour per response, including the time for reviewing instructions, searching existing data sources, gathering and maintaining the data needed, and completing and reviewing the collection of information. Send comments regarding this burden estimate or any other aspect of this collection of information, including suggestions for reducing this burden, to Washington Headquarters Services, Directorate for Information Operations and Reports, 1215 Jefferson Davis Highway, Suite 1204, Arlington, VA 22202-4302, and to the Office of Management and Budget, Paperwork Reduction Project (0704-0188), Washington, DC 20503.				
1. AGENCY USE ONLY (Leave blank)	2. REPORT DATE October 2009	3. REPORT TYPE AND DATES COVERED Final Report – August 2008		
4. TITLE AND SUBTITLE Engineering Studies on Structural Integrity of Railroad Tank Cars Under Accident Loading Conditions			5. FUNDING NUMBERS EB034/RR-28	
6. AUTHOR(S) D.Y. Jeong, Y.H. Tang, H. Yu, M.L. Lyons, J.E. Gordon, O. Orringer, and A.B. Perlman				
7. PERFORMING ORGANIZATION NAME(S) AND ADDRESS(ES) U.S. Department of Transportation Volpe National Transportation Systems Center Research and Innovative Technology Administration Cambridge, MA 02142-1093			8. PERFORMING ORGANIZATION REPORT NUMBER	
9. SPONSORING/MONITORING AGENCY NAME(S) AND ADDRESS(ES) Federal Railroad Administration Office of Research and Development 1200 New Jersey Ave., SE Washington, D.C. 20590			10. SPONSORING/MONITORING AGENCY REPORT NUMBER  DOT/FRA/ORD-09/18	
11. SUPPLEMENTARY NOTES				
12a. DISTRIBUTION/AVAILABILITY STATEMENT  This document is available on the FRA Web site at <a href="http://www.fra.dot.gov/">http://www.fra.dot.gov/</a> .			12b. DISTRIBUTION CODE	
13. ABSTRACT (Maximum 200 words)  This report describes research conducted to support the Federal Railroad Administration (FRA) in addressing safety recommendations made by the National Transportation Safety Board (NTSB) regarding a train derailment that occurred near Minot, North Dakota on January 18, 2002. Engineering studies entailing analysis and testing are described, which include (1) analysis of derailment dynamics based on lumped-parameter models, (2) analysis of the structural behavior of tank car components (such as the head and shell) based on finite element modeling, (3) tank car steels characterization based on laboratory testing of samples obtained from tank cars. Specific details of the research are described. Conclusions based on the research findings to date are outlined.  The research began to provide FRA with technical support in responding to recommendations made by the NTSB following the Board's investigation of the Minot accident. Research results are now being applied to support: (1) rulemaking proposed by FRA and the Pipeline and Hazardous Materials Safety Administration to ensure the safe transport of hazardous materials by tank cars and (2) an industry research-and-development effort, called the Next Generation Rail Tank Car Project that was formed to develop and implement new improved designs for tank cars carrying hazardous materials.				
14. SUBJECT TERMS Accidents, closing speed, finite element analysis, derailment dynamics, hazardous materials, impact loads			15. NUMBER OF PAGES 90	16. PRICE CODE
17. SECURITY CLASSIFICATION OF REPORT Unclassified	18. SECURITY CLASSIFICATION OF THIS PAGE Unclassified	19. SECURITY CLASSIFICATION OF ABSTRACT Unclassified	20. LIMITATION OF ABSTRACT	



## **Preface**

The Federal Railroad Administration (FRA), Office of Research and Development, sponsored the work described in this report. Specifically, this work was conducted and managed by the Structures and Dynamics Division of the Volpe National Transportation Systems Center (Volpe Center) through a Project Plan Agreement with FRA. Moreover, this work is carried out through the Volpe Center's Tank Car Structural Integrity Project in FRA's Rail Equipment Safety Research Program. Ms. Claire Orth (retired) was the Chief of the Equipment and Operating Practices Division. Mr. Francisco González, III is the Project Manager for research on railroad tank cars. Mr. Eloy Martinez also provided technical direction to this project.

Part of the work described in this report, specifically the full-scale tank car shell impact tests, was also conducted in support of an industry research-and-development effort called the Next Generation Rail Tank Car (NGRTC) Project. Dow Chemical Company, Union Pacific Railroad, and Union Tank Car Company are the industry sponsors of this collaboration. In January 2007, FRA signed a Memorandum of Cooperation with the industry sponsors of the NGRTC Project to share research information. Transport Canada and the Department of Homeland Security also participated in this project through Memoranda of Cooperation.

Professor Christopher Barkan of the University of Illinois at Urbana-Champaign is acknowledged for his assistance in providing access to computers at the National Center for Supercomputing Applications.

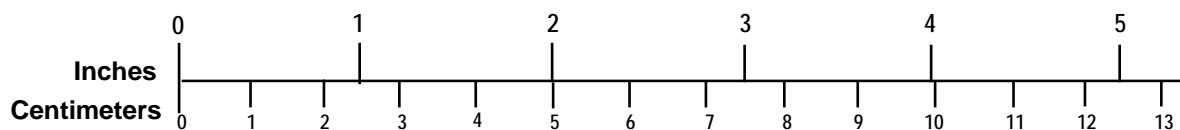
# METRIC/ENGLISH CONVERSION FACTORS

## ENGLISH TO METRIC

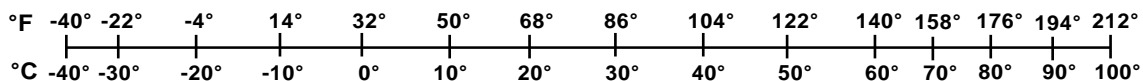
## METRIC TO ENGLISH

<b>LENGTH (APPROXIMATE)</b> 1 inch (in) = 2.5 centimeters (cm) 1 foot (ft) = 30 centimeters (cm) 1 yard (yd) = 0.9 meter (m) 1 mile (mi) = 1.6 kilometers (km)	<b>LENGTH (APPROXIMATE)</b> 1 millimeter (mm) = 0.04 inch (in) 1 centimeter (cm) = 0.4 inch (in) 1 meter (m) = 3.3 feet (ft) 1 meter (m) = 1.1 yards (yd) 1 kilometer (km) = 0.6 mile (mi)
<b>AREA (APPROXIMATE)</b> 1 square inch (sq in, in <sup>2</sup> ) = 6.5 square centimeters (cm <sup>2</sup> ) 1 square foot (sq ft, ft <sup>2</sup> ) = 0.09 square meter (m <sup>2</sup> ) 1 square yard (sq yd, yd <sup>2</sup> ) = 0.8 square meter (m <sup>2</sup> ) 1 square mile (sq mi, mi <sup>2</sup> ) = 2.6 square kilometers (km <sup>2</sup> ) 1 acre = 0.4 hectare (he) = 4,000 square meters (m <sup>2</sup> )	<b>AREA (APPROXIMATE)</b> 1 square centimeter (cm <sup>2</sup> ) = 0.16 square inch (sq in, in <sup>2</sup> ) 1 square meter (m <sup>2</sup> ) = 1.2 square yards (sq yd, yd <sup>2</sup> ) 1 square kilometer (km <sup>2</sup> ) = 0.4 square mile (sq mi, mi <sup>2</sup> ) 10,000 square meters (m <sup>2</sup> ) = 1 hectare (ha) = 2.5 acres
<b>MASS - WEIGHT (APPROXIMATE)</b> 1 ounce (oz) = 28 grams (gm) 1 pound (lb) = 0.45 kilogram (kg) 1 short ton = 2,000 pounds (lb) = 0.9 tonne (t)	<b>MASS - WEIGHT (APPROXIMATE)</b> 1 gram (gm) = 0.036 ounce (oz) 1 kilogram (kg) = 2.2 pounds (lb) 1 tonne (t) = 1,000 kilograms (kg) = 1.1 short tons
<b>VOLUME (APPROXIMATE)</b> 1 teaspoon (tsp) = 5 milliliters (ml) 1 tablespoon (tbsp) = 15 milliliters (ml) 1 fluid ounce (fl oz) = 30 milliliters (ml) 1 cup (c) = 0.24 liter (l) 1 pint (pt) = 0.47 liter (l) 1 quart (qt) = 0.96 liter (l) 1 gallon (gal) = 3.8 liters (l) 1 cubic foot (cu ft, ft <sup>3</sup> ) = 0.03 cubic meter (m <sup>3</sup> ) 1 cubic yard (cu yd, yd <sup>3</sup> ) = 0.76 cubic meter (m <sup>3</sup> )	<b>VOLUME (APPROXIMATE)</b> 1 milliliter (ml) = 0.03 fluid ounce (fl oz) 1 liter (l) = 2.1 pints (pt) 1 liter (l) = 1.06 quarts (qt) 1 liter (l) = 0.26 gallon (gal) 1 cubic meter (m <sup>3</sup> ) = 36 cubic feet (cu ft, ft <sup>3</sup> ) 1 cubic meter (m <sup>3</sup> ) = 1.3 cubic yards (cu yd, yd <sup>3</sup> )
<b>TEMPERATURE (EXACT)</b> $[(x-32)(5/9)]\text{ }^{\circ}\text{F} = y\text{ }^{\circ}\text{C}$	<b>TEMPERATURE (EXACT)</b> $[(9/5)y + 32]\text{ }^{\circ}\text{C} = x\text{ }^{\circ}\text{F}$

## QUICK INCH - CENTIMETER LENGTH CONVERSION



## QUICK FAHRENHEIT - CELSIUS TEMPERATURE CONVERSION



For more exact and or other conversion factors, see NIST Miscellaneous Publication 286, Units of Weights and Measures. Price \$2.50 SD Catalog No. C13 10286

Updated 6/17/98

## Contents

1.	INTRODUCTION .....	1
2.	ANALYSIS OF DERAILMENT DYNAMICS .....	5
2.1	Review of Previous Research .....	5
2.2	Purpose-Built and ADAMS Models .....	6
2.3	Sensitivity Studies.....	7
2.4	Closing Speeds and Impact Forces .....	13
2.5	Discussion and Summary.....	20
3.	STRUCTURAL FINITE ELEMENT ANALYSIS .....	23
3.1	Verification .....	24
3.1.1	Sensitivity Studies.....	25
3.1.2	Static Case Studies.....	37
3.1.3	Dynamic Case Studies .....	39
3.2	Validation.....	41
3.2.1	Head Impacts .....	42
3.2.2	Shell Impacts.....	48
3.2.3	Unnotched Charpy Tests.....	54
3.3	Discussion and Summary.....	59
4.	TANK CAR STEELS CHARACTERIZATION.....	65
4.1	Basic Material Characterization.....	66
4.2	High-Rate Fracture Toughness .....	70
4.3	Pendulum Impact Testing of Bulk Fracture Behavior .....	77
4.4	Discussion and Summary.....	79
5.	CONCLUSIONS.....	81
6.	REFERENCES .....	83
	APPENDICES	
A	NTSB RECOMMENDATIONS FROM THE MINOT ACCIDENT .....	88
B	ESTIMATION OF SAMPLE SIZE AND CONFIDENCE LEVEL .....	89

## Figures

1.	Number of Accidents per Year with at least One Car Releasing Hazmat from FRA RAIRS Database .....	1
2.	TIH Tank Cars Releasing Lading in Accidents by Year, 1965-2005 [1].....	2
3.	Accident-Caused Releases in TIH Tank Cars, 1965-2005 [1] .....	2
4.	Derailment Buckling Patterns .....	7
5.	Relative Effect of Parameters on Number of Derailed Cars using Purpose-Built Model .....	9
6.	Relative Effect of Parameters on Number of Derailed Cars using ADAMS Model .....	9
7.	Relative Effect of Parameters on Maximum Closing Speed using Purpose-Built Model .....	10
8.	Relative Effect of Parameters on Maximum Closing Speed using ADAMS Model .....	10
9.	Relative Effect of Parameters on Peak Coupler Force Purpose-Built Model .....	11
10.	Relative Effect of Parameters on Peak Coupler Force ADAMS Model .....	11
11.	Effect of Train Speed on Number of Derailed Cars from Different Models .....	12
12.	Effect of Ground Friction on Number of Derailed Cars from Different Models .....	13
13.	Characteristic Motions as Possible Sources of Impact.....	13
14.	Maximum Closing Speeds Based on Difference in Translational Velocity.....	14
15.	Maximum Closing Speeds Based on Difference in Angular Velocity.....	15
16.	Maximum Coupler Forces for First 40 Cars of 100-Car Train .....	16
17.	Closing Speeds for Initial Contact .....	17
18.	Impact Forces for Initial Contact .....	18
19.	Gross Motions of Rail Cars and Post-Derailment, Car-to-Car Impacts .....	18
20.	Closing Speeds for Secondary Contact .....	19
21.	Impact Forces for Secondary Contact .....	20
22.	Simulated and Generalized Car-to-Car Impact Scenarios.....	21
23.	Stills from Surveillance Video of an Actual Train Derailment.....	22
24.	Schematic of Dynamic Simulations for Sensitivity Studies.....	27
25.	Schematic of Static Analysis for Sensitivity Studies .....	27
26.	Comparison of Force-Indentation Results.....	30
27.	Contours of Equivalent Plastic Strain using Solid Elements .....	31
28.	Contours of Equivalent Plastic Strain using Shell Elements.....	31
29.	Comparison between Static and Dynamic Finite Element Analyses .....	32
30.	Comparison between Static and Dynamic Finite Element Analyses .....	33

Figures (continued)

31.	Contours of Equivalent Plastic Strain from Dynamic Analysis using Shell Elements .....	33
32.	Comparison Force-Indentation Curves from Static Analysis using Shell Elements .....	34
33.	Comparison Force-Indentation Curves from Dynamic Analysis using Shell Elements .....	35
34.	Force-Indentation Curves from Static and Dynamic Analysis using Solid and Shell Elements.....	35
35.	Comparison of Force-Indentation Curves for Center Loaded Ellipsoidal Cap.....	38
36.	Comparison of Force-Indentation Curves for Cylindrical Shell .....	38
37.	Comparison between Static and Dynamic FEA for Head Indentation.....	40
38.	Comparison between Static and Dynamic FEA for Shell Indentation.....	40
39.	Dynamic Lumped-Mass Model for Tank Car Impacts .....	41
40.	Impact Force as a Function of Closing Speed for Head Impacts .....	41
41.	Rigid-Deformable Finite Element Model of Tank Container .....	42
42.	Comparison between Calculated and Measured Impact Forces.....	47
43.	Comparison between Calculated and Measured Residual Dent Depths .....	47
44.	Comparison between Calculated and Measured Residual Dent Widths .....	48
45.	Position of Tank Car in Full-Scale Tests .....	49
46.	Comparison of Force-Time Histories for Test 0 .....	50
47.	Comparison of Force-Time Histories for Test 1 .....	51
48.	Comparison of Force-Indentation Curves for Test 1 .....	52
49.	Comparison of Force-Time Histories for Test 2 .....	53
50.	Schematic of Failure Initiation Envelope based on Stress Triaxiality .....	55
51.	Schematic of Linear Strain Softening .....	56
52.	Comparison of BFCM data for Normalized TC-128B with FEA assuming Bao-Wierzbicki Criterion.....	56
53.	Comparison of Different Failure Criteria with BFCM Test Data for TC-128B Tank Car Steel .....	57
54.	Comparison of Measured and Calculated Fracture Energies for Different Steels (Blunt Striker) .....	58
55.	Percent Variation in Impact Energy with Parameter Changes .....	59
56.	Force-Indentation Characteristic for Shell Impact .....	60
57.	Typical FEA Mesh for Full-Scale Shell Impact Simulations.....	61
58.	Generalized Impact Scenarios Examined by FEA .....	62
59.	Distribution of Steels in Pre-1989 Pressure Tank Car Fleet .....	66
60.	Cumulative Distribution of Pressure Tank Car Fleet and Tank Cars used for Testing.....	67
61.	CVN Data for Cars Involved in Three Different Accidents.....	69
62.	Fracture Toughness Master Curve Applied to Shell Data from Retired Cars.....	73

**Figures (continued)**

63. Fracture Toughness Master Curve Applied to Shell Data from Minot Cars.....74

64. High-Rate Fracture Toughness as a Function of CVN Energy at 0°F.....76

65. High-Rate Fracture Toughness as a Function of CVN Energy at -50°F.....77

66. Oversized, Nonstandard Pendulum Impactor.....77

67. BFCM Test Specimen .....78

68. Impact Tups Used in BFCM Tests .....78

69. Fracture Energies for TC-128B Measured in BFCM Tests .....79

## Tables

1.	Baseline Parameters for Sensitivity Studies on Derailment Dynamics Models.....	7
2.	Mechanical Properties and Constants Assumed for Tank Car Steels .....	24
3.	Parameters for Simulated Head Impact Sensitivity Studies.....	26
4.	Results from Sensitivity Analyses using ABAQUS .....	28
5.	Results from Sensitivity Analyses using LS-DYNA .....	29
6.	Details of Simulated Tank Car Head Impact Tests .....	42
7.	Material Properties Assumed for Tank Car Head .....	43
8.	Comparison between FEA and RPI-AAR Head Impact Tests with 100% Outage .....	43
9.	Effect of Modeling Assumptions on Results at Impact Speed of 6 mph .....	44
10.	Effect of Modeling Assumptions on Results at Impact Speed of 11.5 mph .....	45
11.	Comparison between FEA and RPI-AAR Head Impact Tests with 2% Outage .....	46
12.	Summary of Full-Scale Shell Impact Test .....	49
13.	Indenter Face Dimensions .....	49
14.	Comparison of Maximum Forces in Assurance Test .....	51
15.	Comparison between Test 1 and FEA.....	52
16.	Tank Car Configurations Examined by FEA .....	63
17.	Estimated Range of Puncture Velocity and Associated Kinetic Energy for Generalized Head Impact Scenario .....	63
18.	Estimated Range of Puncture Velocity and Associated Kinetic Energy for Generalized Shell Impact Scenario .....	64
19.	Summary of Tensile Test Measurements for TC-128B .....	68
20.	Tensile Property Specifications for TC-128B.....	68
21.	Summary of CVN Impact Energies (ft-lb) at Three Temperatures.....	68
22.	Summary of High-Rate Fracture Toughness Data for Retired Cars .....	72
23.	Summary of High-Rate Fracture Toughness Data from Minot Cars .....	72
24.	Estimated Reference Temperatures.....	75
25.	Estimated Tolerance Limits for High-Rate Fracture Toughness (in ksi- $\sqrt{\text{in}}$ ) .....	75

## Executive Summary

On behalf of the Federal Railroad Administration (FRA), the Volpe National Transportation Systems Center (Volpe Center) conducts and manages research on structural integrity of railroad tank cars under accident loading conditions. The research began to provide the FRA with technical support in responding to recommendations made by the National Transportation Safety Board (NTSB) following the Board's investigation of a derailment that occurred near Minot, North Dakota, on January 18, 2002. Research results are now being applied to support: (1) rulemaking proposed by FRA and the Pipeline and Hazardous Materials Safety Administration to ensure the safe transport of hazardous materials (hazmat) by tank cars and (2) a research-and-development effort, called the Next Generation Rail Tank Car (NGRTC) Project, that was formed to develop and implement new improved designs for tank cars carrying hazmat.

The Volpe Center developed a multiphase approach to assess the risks associated with accidents in which railroad tank cars carrying hazardous materials might be involved. Engineering studies entailing analysis and testing are being conducted:

- 1) *Derailment Dynamics*—Physics-based computer simulation models are developed to examine the gross motions of rail cars in a generalized derailment. Moreover, the derailment dynamics model is used to estimate closing speeds that occur when derailed cars separate from the train and collide with one another.
- 2) *Structural Finite Element Analysis*—Dynamic, nonlinear (i.e., elastic-plastic material behavior with large deformations) finite element analysis models are developed to estimate the structural response of the tank car shell and end cap to an assumed scenario (i.e., penetrator shape, initial closing speed, and effective collision mass). The structural finite element analyses are carried out using commercial finite element software.
- 3) *Tank Car Steels Characterization*—A laboratory testing program was conducted to examine the mechanical properties of different steels obtained from either retired railroad tank cars or those involved in accidents. The tests were carried out by Southwest Research Institute under a task order contract with the Volpe Center.

This report describes the engineering studies to examine the structural integrity of railroad tank cars under extreme loading conditions that may be experienced in accidents. Specific details of the research are described.

Major conclusions based on the results to date are summarized as follows for each of phase of research.

### *Derailment Dynamics*

Sensitivity studies using the lumped-parameter models developed for derailment dynamics indicate that train speed and friction have the most significant effect on the derailment outcome in terms of either the number of derailed cars, maximum closing speed, or peak coupler force.

For flat terrain and train speeds not exceeding roughly 40 mph, the maximum closing speeds between cars engaging in post-derailment collisions appear to average about one-half the initial train speed.

### *Structural Response*

The nonlinear finite element analysis (FEA) models developed to examine force-indentation behavior for head and shell deformations were verified through various comparisons.

Dynamic, nonlinear FEA for shell impacts with fluid-structure interaction were validated with data obtained from full-scale tank car tests.

Based on comparisons between FEA and full-scale shell impact test data, peak impact forces and maximum indentations depend on impact speed. In addition, indenter size appears to have a relatively weak effect on the force-indentation characteristic, but a strong effect on puncture.

Finite element procedures will remain useful for predicting structural response of any new car designs that might differ from current practice. Research employing these procedures is ongoing to develop alternative or improved designs for tank cars carrying hazardous materials

### *Tank Car Steels Characterization*

No clear trends were observed between chemical composition, tensile properties, Charpy impact energies, or fracture toughness values and tank car build date.

The extent of scatter observed in the measurements of fracture toughness was quite large, which obscures making definitive conclusions regarding toughness variation with age.

The large scatter makes it unlikely that a practical specification of minimum fracture toughness can be devised to guarantee the prevention of unstable fracture in railroad tank cars subject to derailment forces. A specification of average fracture toughness is possible and could serve to decrease the population of cars at risk of fracture.

## 1. Introduction

The safe transport of hazardous materials (hazmat) by railroad tank cars is a key concern of the Federal Railroad Administration (FRA). Moreover, the objective of FRA-sponsored research is to maintain tank integrity over a broad range of loading conditions that vary from the normal operating environment to rare events such as accidents.

Data from FRA's Railroad Accident/Incident Reporting System (RAIRS) indicates that the number of accidents per year with at least one car releasing hazmat has decreased significantly since the late 1970s (Figure 1). The decrease is attributed to improvements in tank car designs and to Federal regulations that instituted requirements for head shield, thermal protection, and double shelf couplers—each of which reduces the likelihood of rupturing a tank car during an accident.

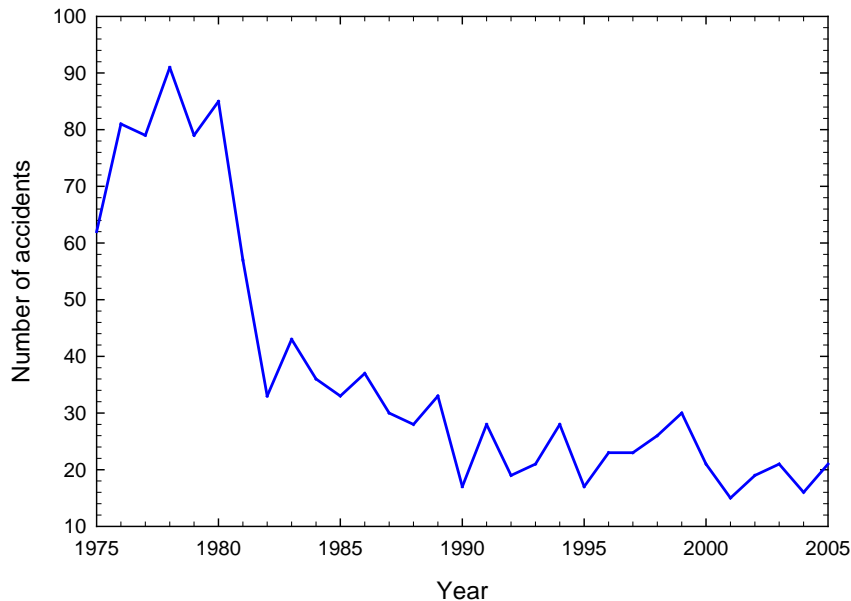


**Figure 1. Number of Accidents per Year with at least One Car Releasing Hazmat from FRA RAIRS Database**

Data on damage to tank cars involved in accidents is also maintained by the Railroad Tank Car Safety Research and Test Project, sponsored by the Railway Supply Institute (RSI) and the Association of American Railroads (AAR). Figure 2 shows a similar trend in the number of accident-caused releases from tank cars carrying specific lading called toxic inhalation hazardous (TIH) materials [1]. Between 1965 and 2005, a total of 252 tank cars released TIH in 176 accidents. Figure 3 shows the causes of lading loss and the number of gallons lost associated with these releases. For example, roughly less than half of the releases are caused by failures in the head and the shell of the tank car, but head and shell failures resulted in over 85 percent of the gallons lost. Failures to valves and fittings account for about one-third of the number of accident-caused releases, but less than 5 percent of the total gallons of lost lading.

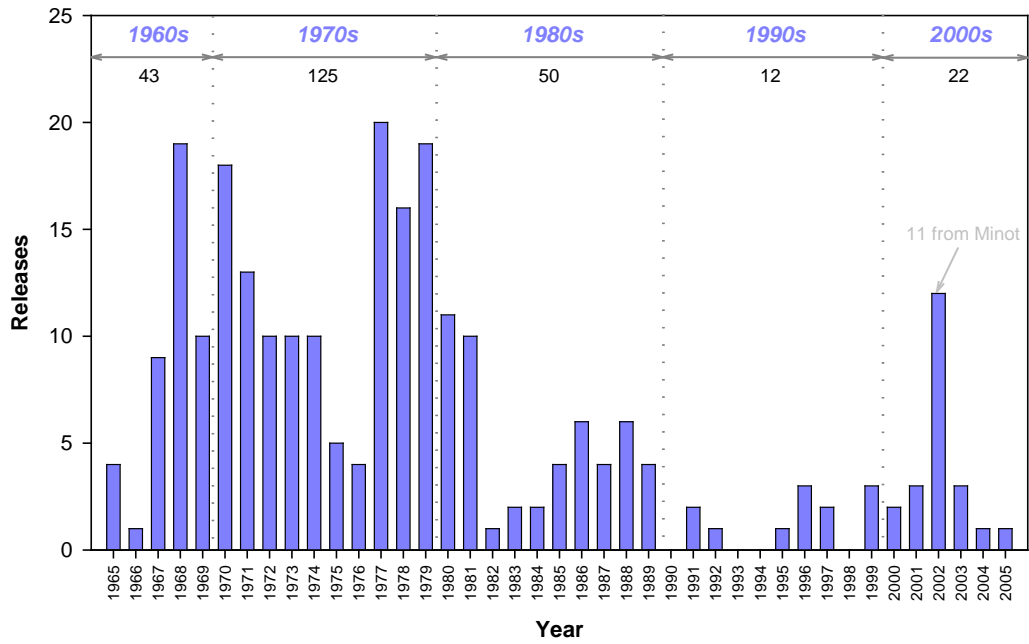


Figure 2. TIH Tank Cars Releasing Lading in Accidents by Year, 1965-2005 [1]

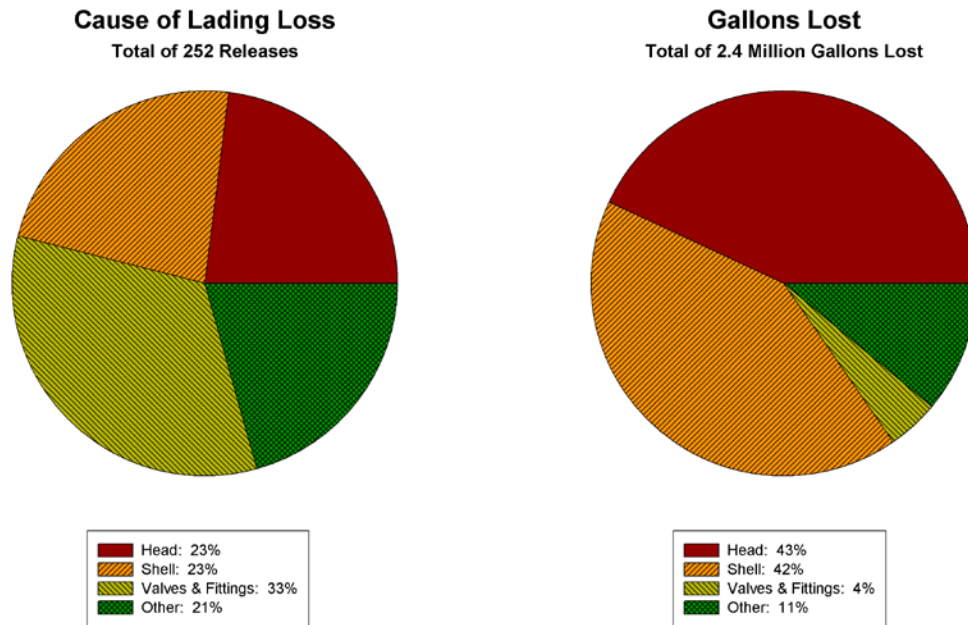


Figure 3. Accident-Caused Releases in TIH Tank Cars, 1965-2005 [1]

Significant accidents involving the release of hazmat are investigated by the National Transportation Safety Board (NTSB). Based on findings from their accident investigations, the NTSB issues recommendations that are intended to prevent similar accidents from occurring.

Three recent accidents have focused attention on the structural integrity of railroad tank cars under accident loading conditions:

- On January 18, 2002, a freight train traveling about 41 miles per hour (mph) derailed near Minot, North Dakota. Five tank cars carrying anhydrous ammonia catastrophically ruptured, which resulted in one fatality, evacuation of the nearby town, property damage exceeding \$2 million, and over \$8 million on environmental remediation [2]. Figure 2 shows that 11 tank cars in this accident released lading, which account for all but one of the total TIH releases for the entire year of 2002 and for half of the total TIH releases between 2000 and 2005 (inclusive).
- On June 28, 2004, a freight train traveling about 45 mph struck the side of a car in another freight train that was entering a siding while traveling about 20 mph in the opposite direction. The collision occurred near Macdona, Texas and resulted in 39 derailed cars, breach of a tank car containing chlorine, three fatalities, and total (i.e., property and environment) damages exceeding \$7 million [3].
- On January 6, 2005, a freight train traveling about 47 mph through Graniteville, South Carolina encountered an improperly lined switch that diverted the train from the mainline onto a side track where it collided with an unoccupied, parked train. Among the derailed freight cars were three tank cars, one of which was breached, releasing chlorine. This accident resulted in nine fatalities; evacuation of about 5,400 people; and total damages exceeding \$6.9 million [4].

Sponsored by the FRA Office of Research and Development, the Volpe National Transportation Systems Center (Volpe Center) conducts and manages research to examine the structural integrity of railroad tank cars. Before the Minot derailment, FRA-sponsored research focused on maintaining tank integrity under normal operating conditions (e.g., metal fatigue and crack propagation). After Minot, research began to support FRA in responding to recommendations made by the NTSB following the Board's investigation of the accident. The NTSB safety recommendations from the Minot derailment are listed in [Appendix A](#).

Research results are now being applied to support: (1) rulemaking proposed by the FRA and the Pipeline and Hazardous Materials Safety Administration, and (2) an industry-sponsored research-and-development effort called the Next Generation Rail Tank Car (NGRTC) Project [5]. Dow Chemical Company, Union Pacific Railroad, and Union Tank Car Company are the industry sponsors of this project. The NGRTC Project began in 2006 with the objective to develop and implement new improved designs for railroad tank cars carrying hazardous materials. In January 2007, FRA signed a Memorandum of Cooperation with the industry sponsors of the NGRTC Project to share research information. Transport Canada and the U.S. Department of Homeland Security also participate in this project through the Memorandum of Cooperation.

The Volpe Center developed a multiphase approach to assess the risks associated with accidents in which railroad tank cars carrying hazardous materials might be involved. Engineering studies entailing analysis and testing are being conducted:

- 1) *Derailment Dynamics*–Physics-based computer simulation models are developed to examine the gross motions of rail cars in a generalized derailment. Moreover, the derailment dynamics model is used to estimate closing speeds that occur when derailed cars separate from the train and collide with one another.
- 2) *Structural Finite Element Analysis*–Dynamics, nonlinear (i.e., elastic-plastic material behavior with large deformations) finite element analysis models are developed to estimate the structural response of the tank car shell and end cap to an assumed scenario (i.e., penetrator shape, initial closing speed, and effective collision mass). The structural finite element analyses are carried out using commercial finite element software (e.g., ABAQUS and LS-DYNA).
- 3) *Tank Car Steels Characterization*–A laboratory testing program was conducted to examine mechanical behavior of different steels obtained from either retired railroad tank cars or those involved in accidents (e.g., Minot). The testing program was carried out by Southwest Research Institute under a task order contract with the Volpe Center.

This report describes these engineering studies to examine the structural integrity of railroad tank cars under extreme loading conditions that may be experienced in accidents. Specific details of the research are described. Conclusions based on the research findings are presented.

## 2. Analysis of Derailment Dynamics

Physics-based models are developed to calculate the gross motions of rail cars during a train derailment. The inputs to the analysis include train make-up and initial train speed. The objective of this modeling phase is to estimate the ranges of closing speeds and incidence angles between cars impending to collide with a loaded tank car. Moreover, the results from the models developed in this phase will be used as initial conditions to more detailed structural finite element models.

In this phase of the modeling research, the verification and validation activities are: deriving the equations of motion for rail cars in a derailment, comparing results from alternative methods that implement the numerical solution to the derived equations of motion, and comparing the present modeling results to those developed from previous work.

### 2.1 Review of Previous Research

Previous research on modeling of rail accidents can be roughly divided into two categories: (1) investigations of vehicle-track interaction and (2) studies of the actions between cars. The objective of research in the first category is to understand the mechanisms of derailment (e.g., wheel climb, excessive lateral-to-vertical wheel load ratio, etc.) The results from vehicle-track interaction models are not directly applicable to the present work, but they can provide some useful information regarding modeling techniques. Past research in the second category is directly applicable to the present work, and has been conducted through two approaches: (a) development of special purpose models and (b) development of models using commercial general purpose software for multibody dynamics.

A special purpose model was developed in the 1970s to examine the gross motions of rail cars in a train derailment [6]. Each car in this planar (i.e., two-dimensional) analysis was assumed to behave as a rigid body of finite length but zero width. A major limitation of this model was that the cars were assumed to remain coupled during the derailment. Another special purpose model was later developed under the sponsorship of Transport Canada (TC) that allowed the cars to decouple, but the criterion for decoupling was incomplete [7] and [8]. The Transport Canada model included provisions for: tangent or curved track, initial derailment at either the lead or trailing truck of the first car off the track, and potential for tank car rollover based on a vertical-to-horizontal force ratio criterion. More recently, a planar model was developed at Queen's University [9], in which the differential equations of motion were derived from Lagrange's equations and were solved numerically using a special-purpose computer program written in FORTRAN.

Commercial general purpose software for multibody dynamics has been used to develop a three-dimensional model to examine train crashes [10]. Specifically, a software package called DADS (Dynamic Analysis Design Simulation) was used to calculate the gross motions for a 20-car train.

None of the previous models made any provisions to calculate relative closing speed, which is a key variable in assessing collision damage.

## **2.2 Purpose-Built Model and ADAMS Model**

A planar (i.e., two-dimensional) purpose-built model to calculate the gross motions of rail cars during a derailment scenario is developed in the present work. The differential equations of motion are derived via Newton's laws of physics. Car motions are defined with respect to a fixed (i.e., non-rotating) and right-handed reference frame. The mathematical formulation is presented in reference 11. The equations of motion are solved numerically via a FORTRAN computer code.

Analysis of derailment dynamics is also carried out using a commercially available general purpose software program for rigid-body dynamics called ADAMS (Automatic Dynamic Analysis of Mechanical Systems) [12].<sup>1</sup> ADAMS allows the user to create objects, forces, and constraints within the modeling environment, and solves for the resulting motions without the user explicitly deriving the equations of motion. Another advantage of using ADAMS is the graphical interface and post-processing tools that readily display output information

Rail cars are constructed in ADAMS as a cylindrical part with an arbitrary radius of 9 feet (ft). The length of the cylinder depends on whether it represents a tank or a locomotive. The locomotive is approximately 60 ft, and tank cars are slightly longer at about 65 ft. A planar constraint, connecting the car center of mass to the ground, is used to limit the car's motion to the x-z plane. A planar constraint is only required on one in a train consist as constraints in the couplers limit the motion of subsequent cars.

In both the purpose-built and ADAMS models, the entire train consist is given an initial velocity in the longitudinal direction and the derailment is modeled with an initial angular velocity and an associated lateral velocity applied on the lead car. The car's motion is resisted by a frictional force applied at the car's trucks, which increases as the truck passes the point of derailment.

Both models include two types of friction: (1) on-track coefficient of friction is an approximation of the maximum frictional force associated with emergency braking and (2) off-track coefficient of friction is an estimate of the complicated resistive forces present when the cars derail.

Couplers are characterized by a length, a dead band, stiffness, and maximum swing angle. The coupler length defines the neutral distance between cars. The coupler dead band is the distance the coupler length can displace before a restoring force is applied.

---

<sup>1</sup> Gross motions of cars in a derailment can also be modeled using LS-DYNA, a commercial finite element code for dynamic nonlinear analysis. The application of LS-DYNA for dynamic structural analysis is described in the next section of this report.

The restoring force is proportional to the coupler stiffness. The maximum swing angle is the angle at which the restoring moment begins to be applied.

In general, the motion of the train consist in a derailment begins with an initial rotation imparted to the lead car and with all cars traveling at a given initial speed. The lead car swings out in the direction of the initial rotation, with higher off-track frictional forces applied at the truck opposing the direction of motion. As the cars derail, the coupler forces between cars create a moment couple. The many highly coupled interactions cause an irregular buckling pattern, which generally occurs in two forms, either as an alternating pile-up as shown in Figure 4(a) or as a curved string of displaced cars as shown in Figure 4(b). The direction of travel is left to right in these figures.



(a) Alternating-Direction Buckling Pattern

(b) Curved String of Displaced Cars

**Figure 4. Derailment Buckling Patterns**

### 2.3 Sensitivity Studies

Sensitivity studies were conducted using the purpose-built (i.e., FORTRAN) model for derailment dynamics [11]. Baseline parameters were developed and varied one factor at a time to examine their relative effect on the following metrics: (1) the number of derailed cars in the simulation, (2) maximum closing speeds, and (3) peak coupler forces. The baseline parameters for the sensitivity studies are listed in Table 1.

**Table 1: Baseline Parameters for Sensitivity Studies on Derailment Dynamics Models**

<i>Parameter</i>	<i>Value</i>
Number of cars in train make-up (train length)	60 cars
Car weight	150,000 lb
Initial longitudinal train speed	37 mph
Initial angular velocity	0.2 radians per second
On-track (rail) coefficient of friction	0.15
Off-track (ground) coefficient of friction	0.50

Each parameter was varied from its baseline value by  $\pm 20$  percent and  $\pm 50$  percent while the remaining inputs including car length and width and coupler characteristics were set equal to their respective baseline values.

Figure 5 shows the relative effect of changing each parameter on the number of derailed cars calculated using the purpose-built model. The baseline case results in 13 cars derailed from the 60-car train. Clearly train speed has the greatest effect on the number of derailed cars. Increasing the initial train speed by 50 percent over the baseline increases the number of derailed cars from 13 to 24. Decreasing the initial train speed by 50 percent below the baseline decreases the number of derailed cars from 13 to 6. Friction also has a significant effect on the number of derailed cars. The relative difference between the ground and rail friction coefficients is proportional to the force required to decelerate the train consist. Greater differences in friction coefficients lead to larger braking forces. Moreover, friction forces have an inverse relationship compared to the other inputs. That is, increasing friction decreases the derailment severity in terms of the number of derailed cars, while increasing the value of the other parameters increases the number of derailed cars.

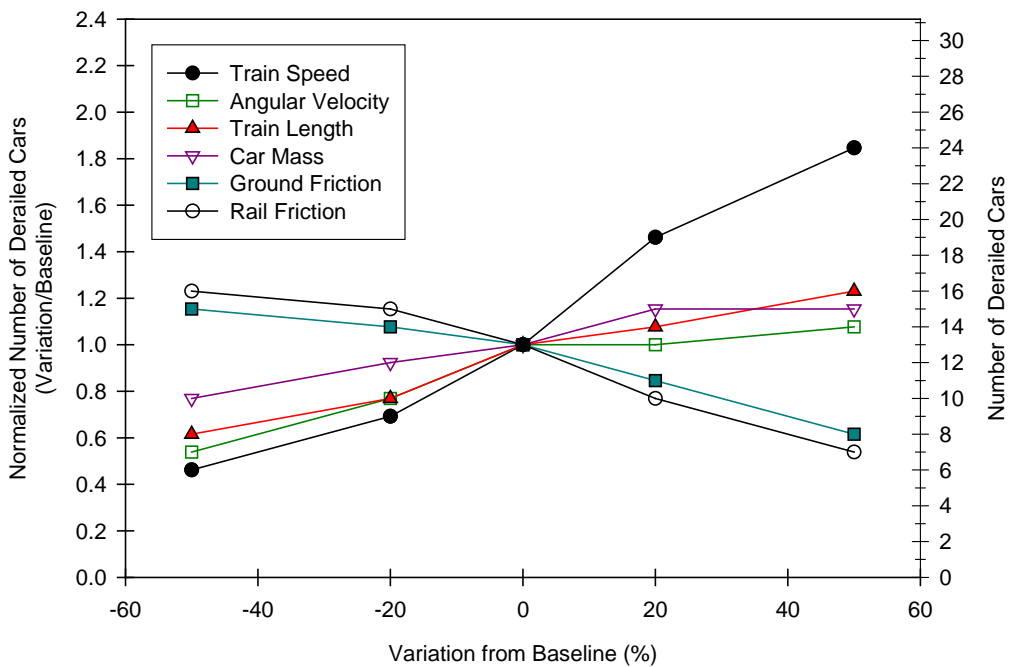
Figure 6 shows similar results for the number of derailed cars calculated using the ADAMS model. The ADAMS model also calculates 13 derailed cars for the baseline case, but shows slightly more derailed cars as the train speed increases. The ADAMS results also show a slightly greater effect of friction on the number of derailed cars than the purpose-built model.

Figure 7 shows the relative effect of changing each parameter on the maximum closing speed calculated using the purpose-built model. The baseline case results in a maximum closing speed of 19 mph. Train speed has the most significant effect on maximum closing speed. Increasing the initial train speed by 50 percent over the baseline increases the maximum closing speed by almost 60 percent. Decreasing the initial train speed by 50 percent below the baseline decreases the maximum closing speed by about 30 percent. Ground friction has a moderate effect on closing speed. Increasing ground friction by 50 percent increases the maximum closing speed by more than 20 percent. Changing the other input parameters varies the maximum closing speed by, at most,  $\pm 15$  percent.

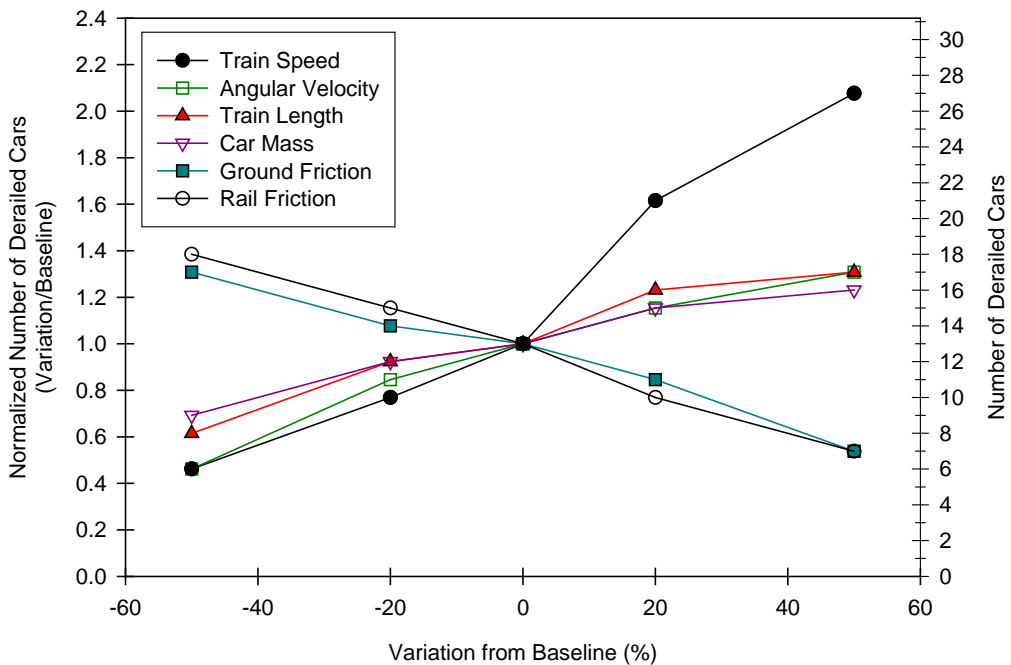
Figure 8 shows the variations in maximum closing speeds calculated using the ADAMS model, which are similar to those using the purpose-built model.

Figure 9 shows the relative effect of changing each parameter on the peak coupler force calculated using the purpose-built model. The peak coupler force corresponding to the baseline case is 1,821 kips. Increasing the initial train speed by 50 percent increases the peak coupler force by almost twice.

Figure 10 shows the results from the ADAMS model. The baseline case corresponds to a peak coupler force of 1,858 kips, which is slightly higher than the baseline calculated by the purpose-built model. Again, the variations in peak coupler forces calculated using the ADAMS model are similar to those calculated using the purpose-built model.



**Figure 5. Relative Effect of Parameters on Number of Derailed Cars using Purpose-Built Model**



**Figure 6. Relative Effect of Parameters on Number of Derailed Cars using ADAMS Model**

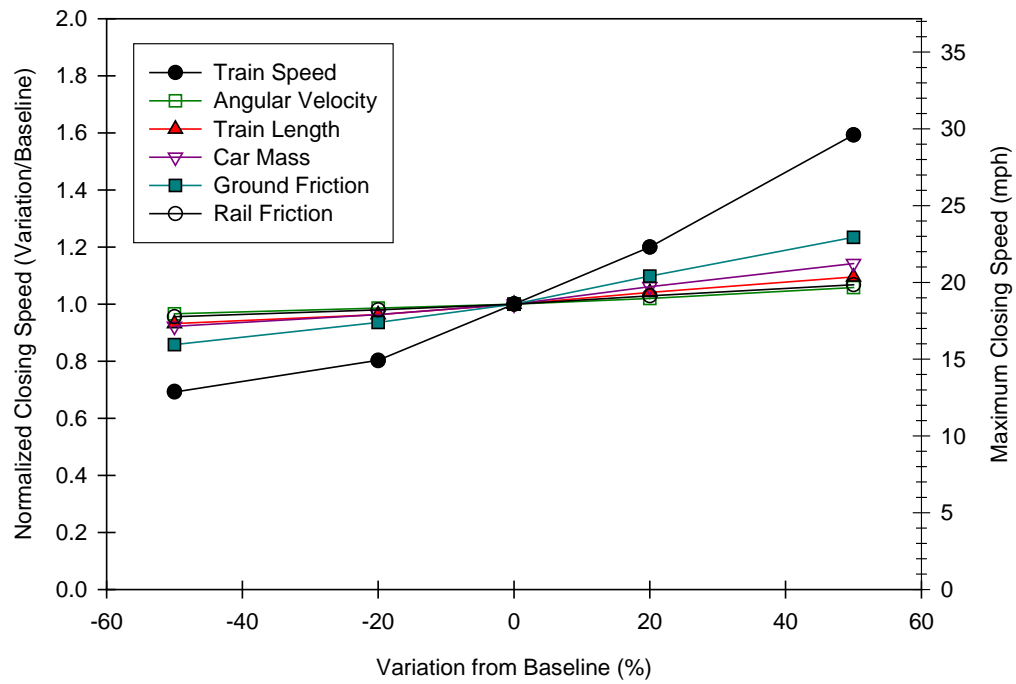


**Figure 7. Relative Effect of Parameters on Maximum Closing Speed using Purpose-Built Model**

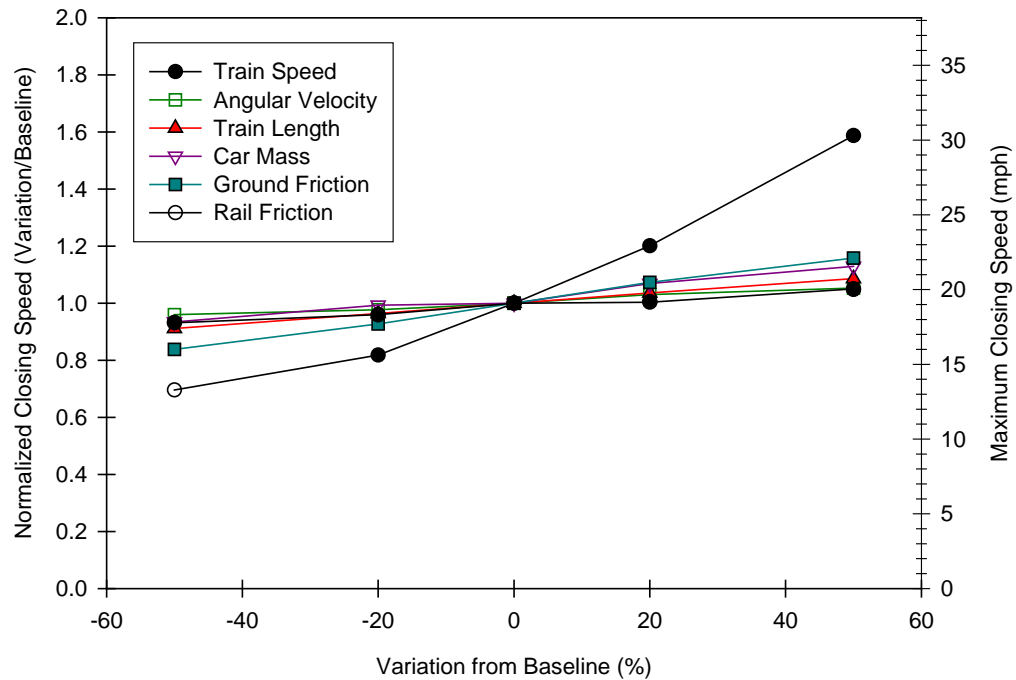


**Figure 8. Relative Effect of Parameters on Maximum Closing Speed using ADAMS Model**

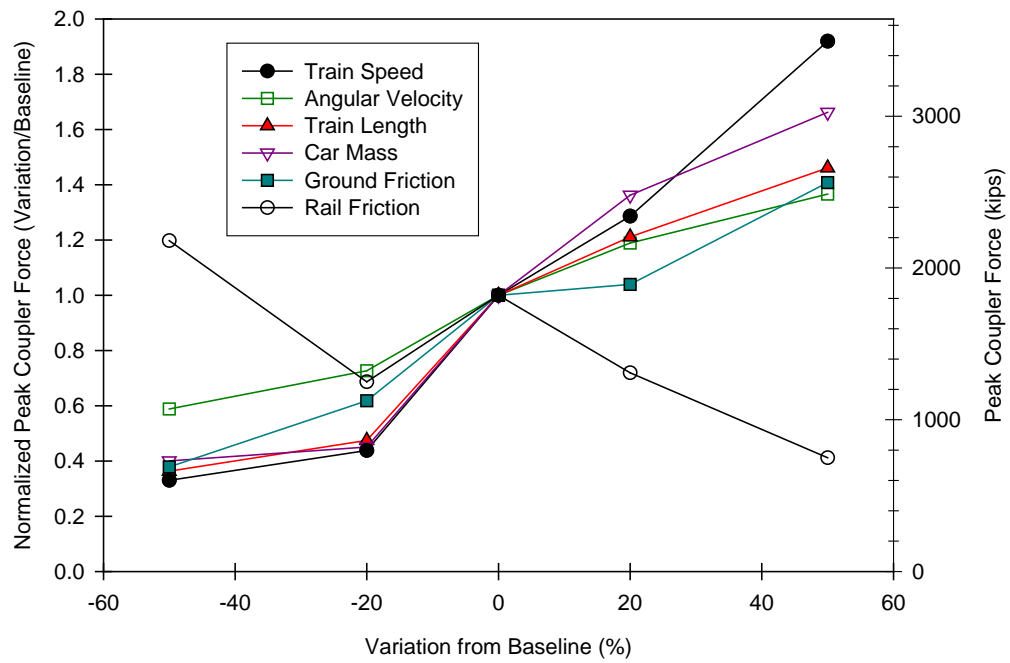


**Figure 9. Relative Effect of Parameters on Peak Coupler Force using Purpose-Built Model**

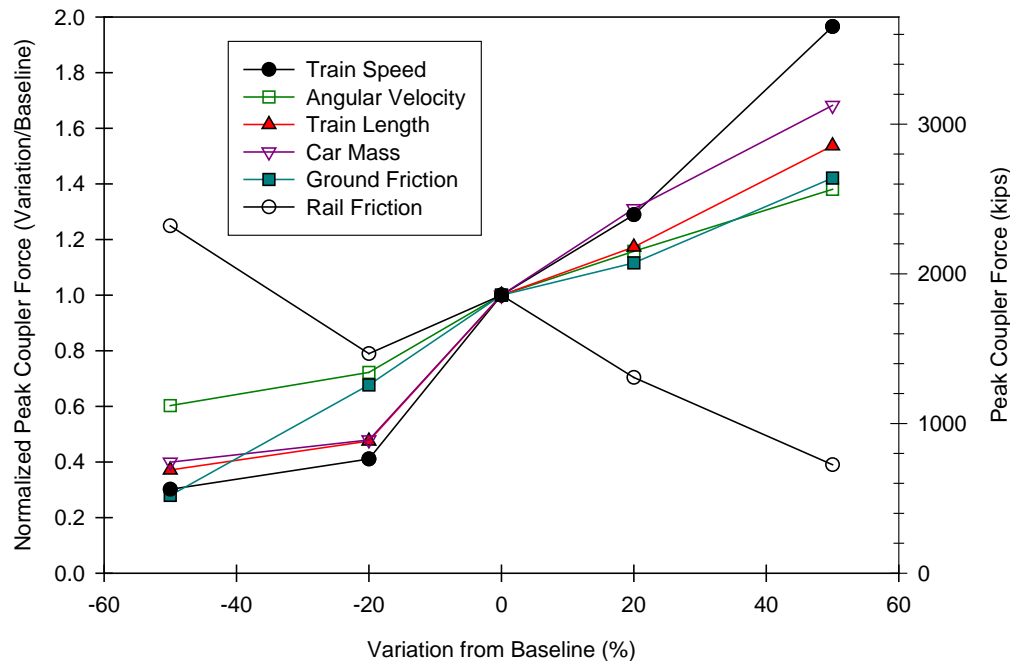


**Figure 10. Relative Effect of Parameters on Peak Coupler Force using ADAMS Model**

The sensitivity analyses using both the purpose-built and ADAMS models indicate that train speed and friction have the most significant effect on derailment severity in terms of either number of derailed cars, maximum closing speed, or peak coupler force. The results from the sensitivity studies are compared to those from previous work to validate the derailment dynamics models. For example, Figure 11 shows the effect of train speed on the number of derailed cars as calculated by three different models: the purpose-built model, the ADAMS model, and the Queen’s University (QU) special purpose model [9]. Although the baseline parameters are somewhat different in the parametric studies for each derailment dynamics model, the relative effect of train speed of the number of derailed cars is consistent.

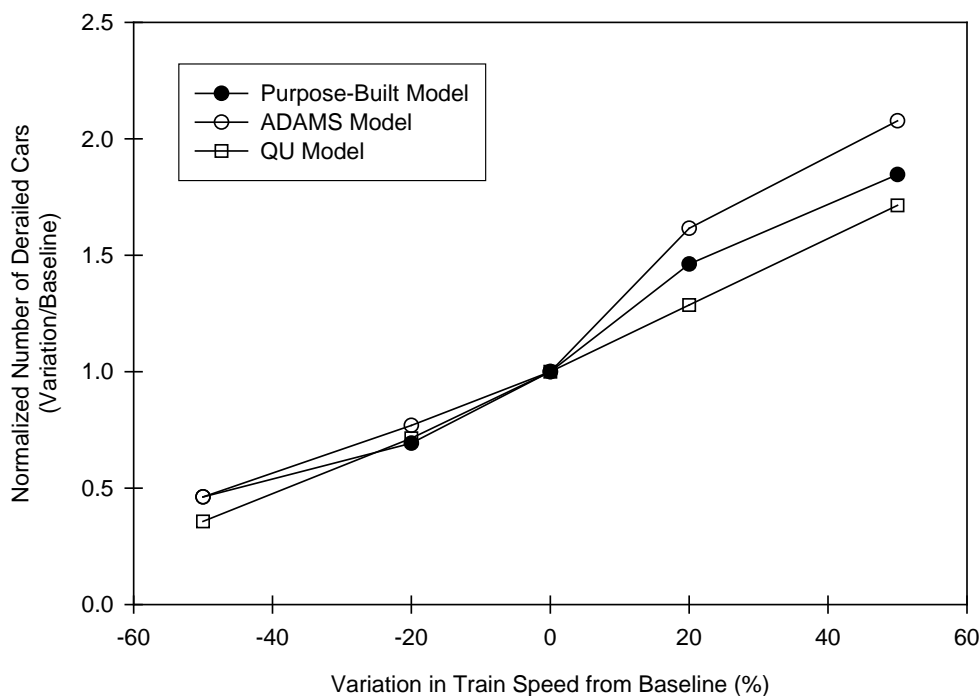


**Figure 11. Effect of Train Speed on Number of Derailed Cars from Different Models**

Figure 12 shows the effect of ground friction on the number of derailed cars, as calculated from the different models. The results from the purpose-built and ADAMS models are comparable. All three models show that ground friction has a strong effect on the number of derailed cars. Moreover the number of derailed cars increases as the off-track or ground coefficient of friction is increased.

In the development of the special purpose model by Queen’s University, results from the derailment dynamics were compared to a derailment that occurred in Mississauga, Ontario, Canada on November 10, 1979 [13]. The Queen’s model reproduced the number of derailed cars in that derailment (24 cars).

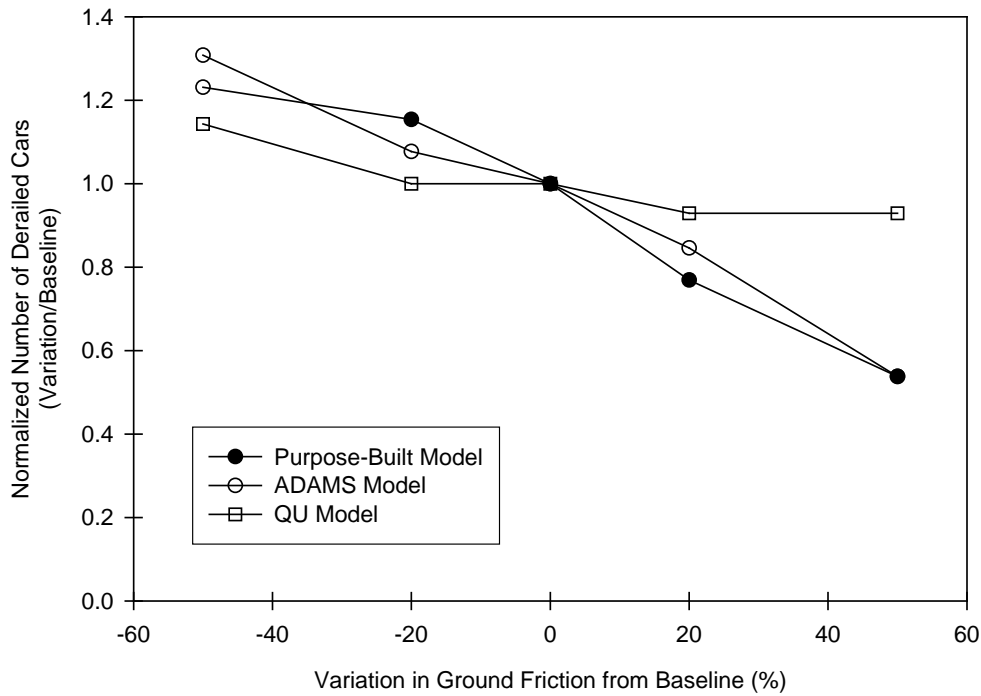


**Figure 12. Effect of Ground Friction on Number of Derailed Cars from Different Models**

## 2.4 Closing Speeds and Impact Forces

In this section, the closing speeds of adjacent cars calculated by the ADAMS model are examined. Moreover, the kinematics from a 100-car train identified two characteristic motions as possible sources of impact, which are shown in Figure 13. The first mode occurs from the relative difference in the absolute translational velocities of adjacent cars. The second mode of possible collision occurs as the cars buckle.



(a) Difference in Translational Velocities

(b) Difference in Angular Velocities

**Figure 13. Characteristic Motions as Possible Sources of Impact**

In the first characteristic motion, differences in the on- and off-track coefficients of friction and coupler interactions cause the velocities of the cars to fluctuate. When the

lead car is slower than the trailing car at a given time, the distance between cars decreases until the coupler resists the motion.

The trailing car's translational velocity is subtracted from the leading car's to obtain the first car's velocity relative to the second. The relative velocity is considered positive if the lead car is moving faster than the trailing car and negative if the trailing car is moving faster. Therefore, negative relative velocity represents the closing speed between the two cars. The maximum closing speeds for the first 40 cars in the analysis of a 100-car train are shown in Figure 14. Maximum closing speeds may occur at any given distance between adjacent cars, but closer inspection of the kinematics indicates that they generally occur when the coupler is at its minimum length.

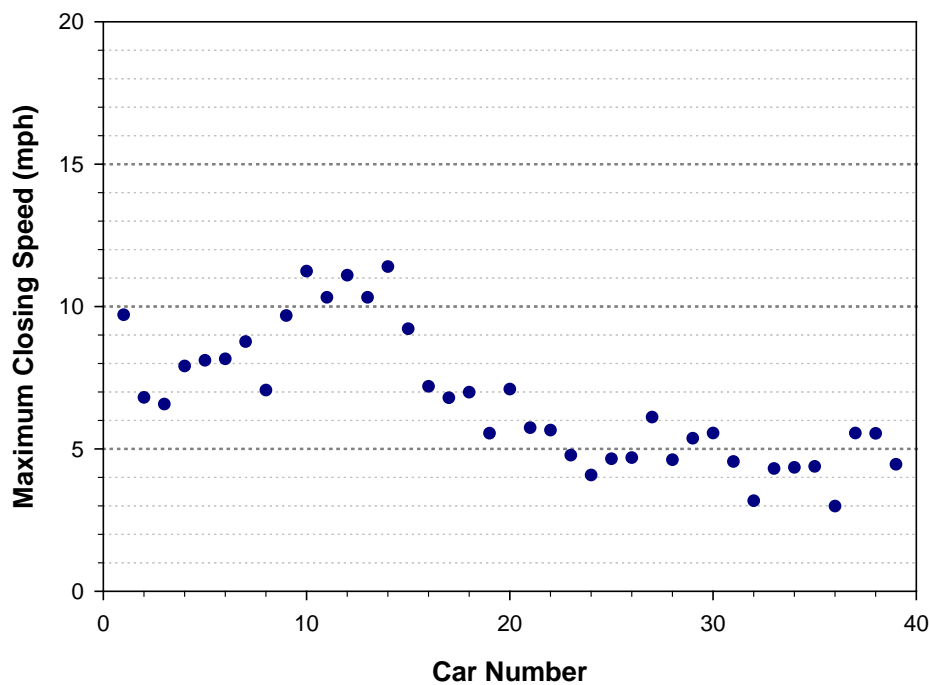


**Figure 14. Maximum Closing Speeds Based on Difference in Translational Velocity**

The closing speeds tend to increase from the front of the train (where the derailment is initiated) to the middle of the derailed cars. The maximum closing speed is slightly more than 11 mph on the 14th car. The values then drop off to the end of the derailed cars. The largest closing speeds of the non-derailed cars fluctuate and are bounded between 3 and 6 mph, which are significantly lower than those of the derailed cars. The times at which the maximum closing speeds occur vary greatly with no trend, but all occur between 5 and 10 seconds into the simulation.

In the second characteristic mode of possible collision, the cars derail in an alternating direction and tend to collapse on each other. The closing speed is determined by first taking the magnitude of the difference of the adjacent cars' angular velocities (the sign of the relative velocity is ignored since cars can collapse in either the positive or negative

angular direction). Then, the relative angular velocity is multiplied by half the car length to calculate the speed at the ends of the cars, which is the location where the closing speed is the highest. At the time of the maximum closing speed, the cars are not necessarily in an alternating buckling pattern. But closer inspection of the kinematics indicates that the maxima generally occur as the cars reach their maximum buckling. The cars also rotate about their center of gravity, meaning that adjacent cars would not impact by pure rotation. Some translational displacement is also required to bring the cars into contact.

Determining how fast cars may collapse on each other provides an estimate of the maximum closing speeds. Figure 15 shows the results of this calculation for the first 40 cars. As with the closing speeds found from the relative translational speed of the cars, the buckling action of the cars produces higher closing speeds at the front of the train. These closing speeds are generally larger than those produced from the difference in translational velocity, with a maximum of 19.6 mph. The closing speeds begin to drop off for the non-derailed cars and do not vary greatly, averaging about 3.5 mph for the 16 non-derailed cars shown in Figure 15.

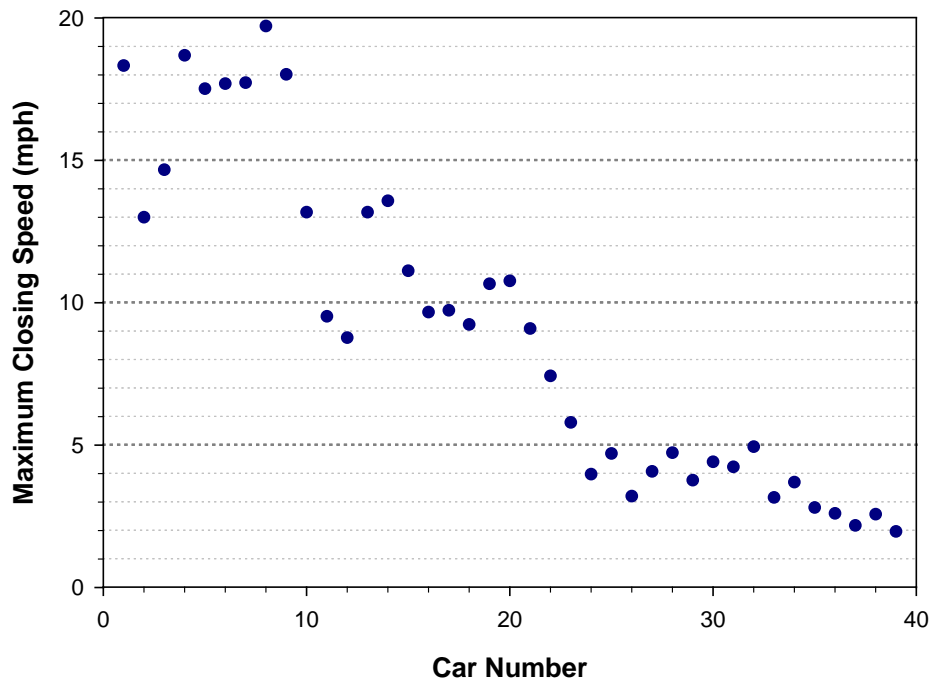


**Figure 15. Maximum Closing Speeds Based on Difference in Angular Velocity**

The closing speeds shown in the two previous figures ignore any effect that breaking of the couplers may have on the rotation. Moreover, additional criteria or analyses are needed to calculate impact forces.

For example, impact forces may be represented by the coupler forces. Although the coupler generally prevents adjacent cars from impacting, the coupler forces would likely

result in an impact event for relatively large forces. Figure 16 shows the maximum coupler forces calculated from the 100-car train ADAMS model. These results, however, only provide an approximation of the impact forces that may be expected because breaking of the coupler was not included in this analysis. Also, the force levels are only valid relative to the other impact forces. Moreover, these results indicate locations of the highest values. The actual quantities would vary depending on factors such as the coupler stiffness. The maximum coupler forces generally correspond with the maximum closing speed with the values increasing from the first car to the 13th car at 7.9 million pounds of force. The maximum coupler forces then begin to decrease to the end of the derailed cars. Large forces can be seen throughout the remaining consist and vary between about 2 million and 5 million pounds of force.

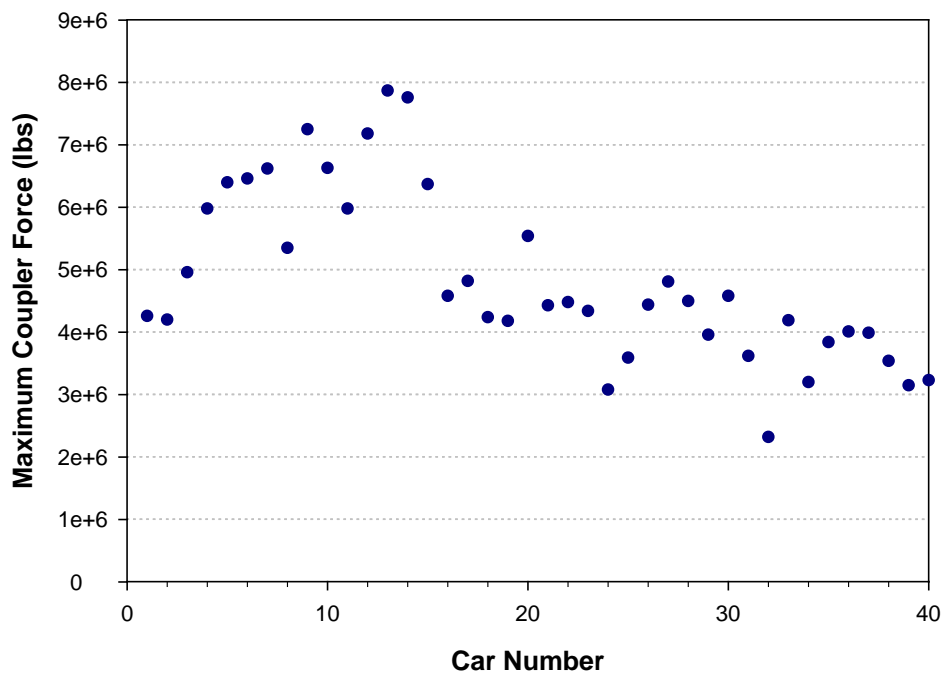


**Figure 16. Maximum Coupler Forces for First 40 Cars of 100-Car Train**

Another ADAMS model is used to examine interactions between decoupled cars. A train consist of 30 cars with a 70-car equivalent lumped mass on the 30th car is carried out which allows coupler breaks and contact forces to occur for the first 10 cars in the train consist. The contact between cars is categorized as either initial or secondary contact. Initial contacts occur just after the cars decouple. Secondary contact includes all impacts that occur after the cars have been decoupled.

As the first car in the train consist rotates and passes the point of derailment, it begins to slow. Its rear coupler eventually reaches the maximum displacement and breaks. The car continues to slow until the second car impacts it in the rear. This sequence of events sets off a chain reaction of decoupling and impact, which propagates down the train consist.

Figure 17 shows the closing speeds associated with initial impacts. The closing speeds are relatively low for the lead cars since the difference in speed for the first and second car is only a result of off-track friction applied to the first car. The values then sharply rise as the contact force of the first car striking the second creates a much larger difference in speed between the second and third cars in the consist. The effect of slowing cars propagates back and the closing speeds continue to increase. The maximum closing speed of about 18 mph occurs between the last two cars with contact forces applied.

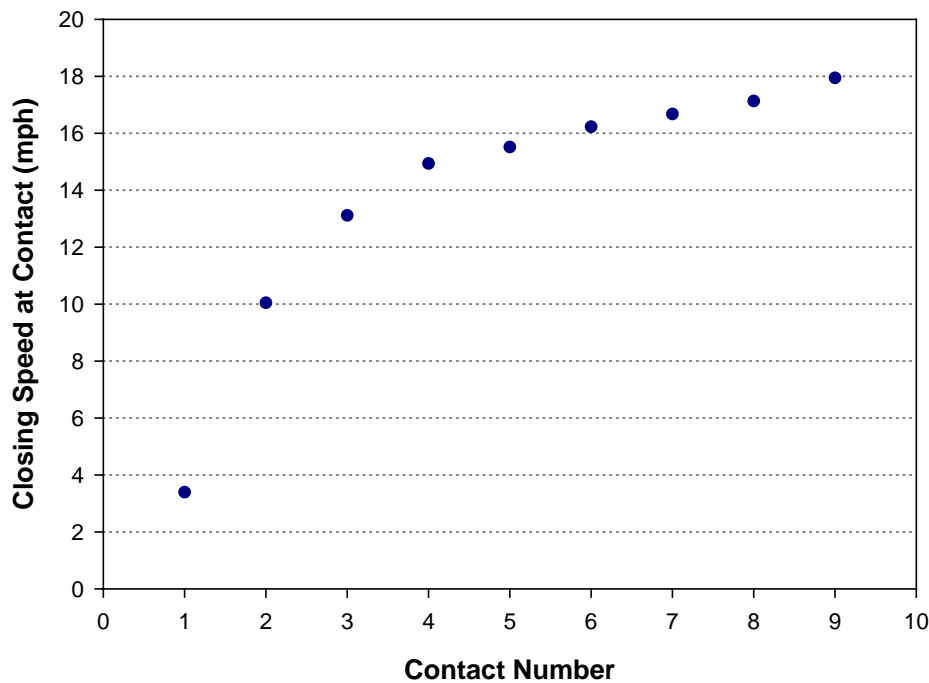


**Figure 17. Closing Speeds for Initial Contact**

The corresponding impact forces for initial contact follow a similar general trend, as shown in Figure 18. These impact forces are estimated values based upon assumed values for spring stiffness of the contact force, and are only valid relative to other forces. Moreover, these results suggest that the maximum closing speeds and maximum impact forces for initial contact are somewhat correlated.

Secondary impacts are less orderly than the initial contact. Small differences in the timing of the decoupling, the lead car's initial rotation, and the fact that the 11th car cannot decouple, cause the cars to have a non-uniform motion. The action of the secondary contact on gross motions of rail cars in this generalized derailment scenario is shown in Figure 19. In total, there are eight secondary impacts of significance. The cars remain in order corresponding to their original position in the train consist. The time at which the secondary impacts occur is also shown in the figure. Also, the figure calls out the car-to-car interactions for each contact event. For example, the secondary impact at 6.79 seconds corresponds to the cars 3 and 4 contacting each other.

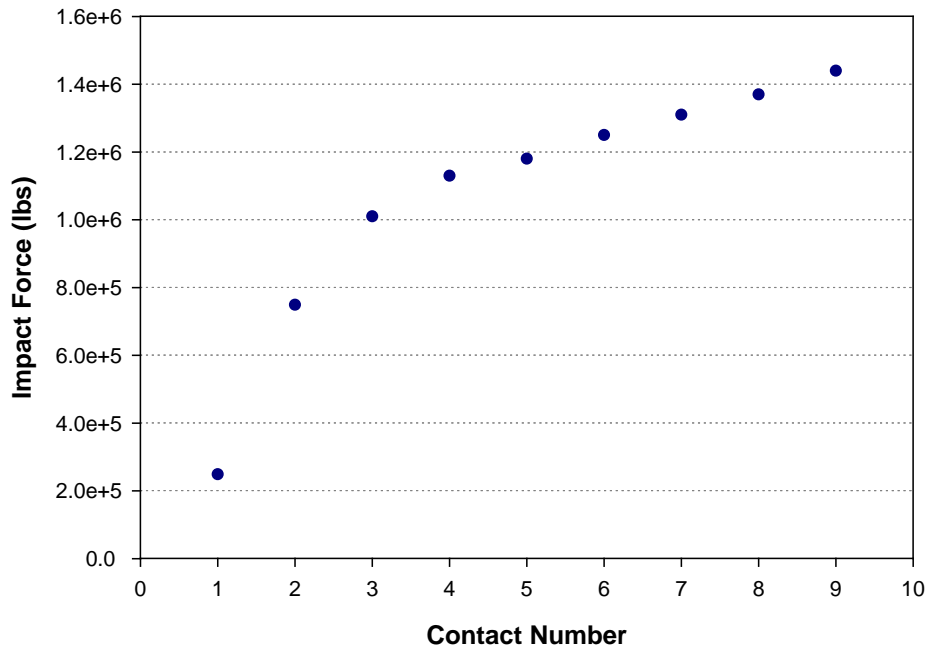


**Figure 18. Impact Forces for Initial Contact**

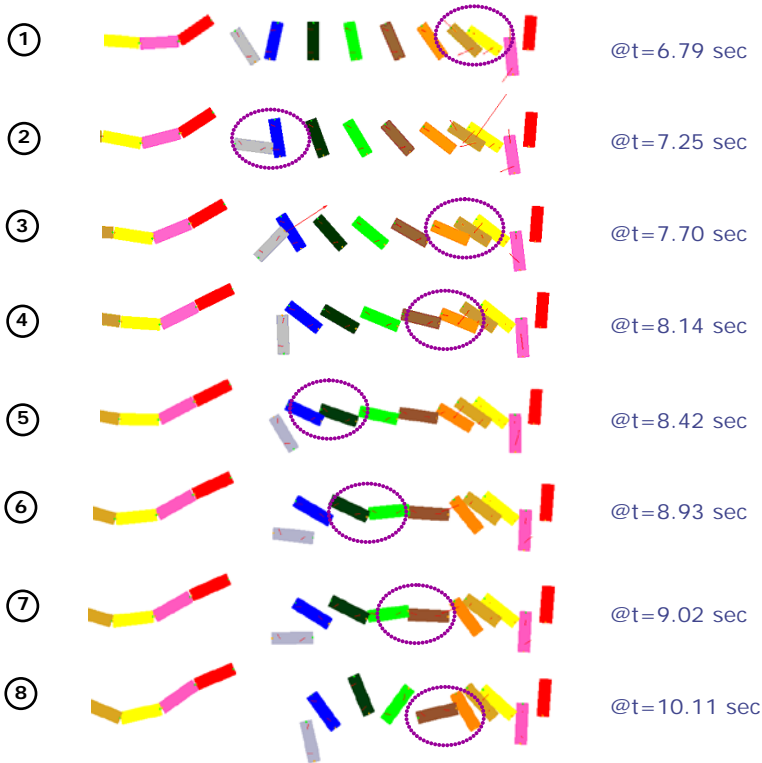


**Figure 19. Gross Motions of Rail Cars and Post-Derailment, Car-to-Car Impacts**

Figure 20 shows the closing speeds corresponding to the secondary or post-derailment, car-to-car impacts. The closing speeds at impact vary between a minimum of 9 mph and a maximum of 51 mph. Although initial contact involved relatively little difference in angular velocity, it appears that secondary contact is generally associated with larger differences in angular velocity, which results in larger closing speeds.

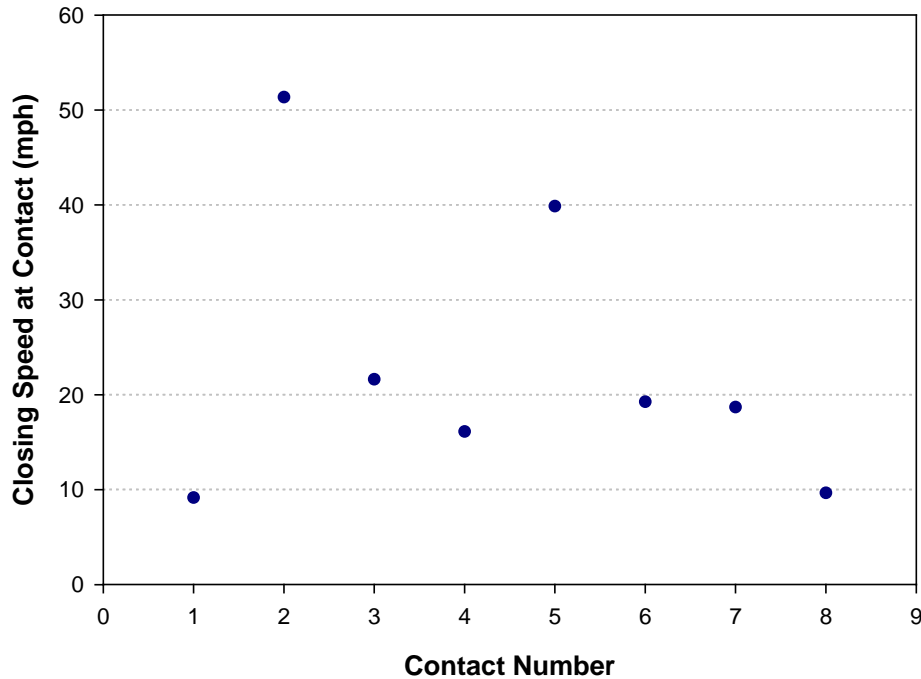


**Figure 20. Closing Speeds for Secondary Contact**

The impact forces from secondary contact also exhibit a large variance, as shown in Figure 21. Unlike the initial impact forces, the secondary interactions do not indicate a correlation between the closing speeds and impact forces. Also, the majority of forces are significantly lower than initial impacts, with a maximum secondary impact force of 1.6 million pounds. The lack of correlation between closing speeds and impact forces demonstrates the chaotic nature of post-derailment, car-to-car impacts.

The results presented in this section for impact forces are estimations based upon the analysis of derailment dynamics. The calculation of impact forces is further refined by analyzing the structural response of tank car components to various collision scenarios through finite element analysis, which is described in the next section of this report.

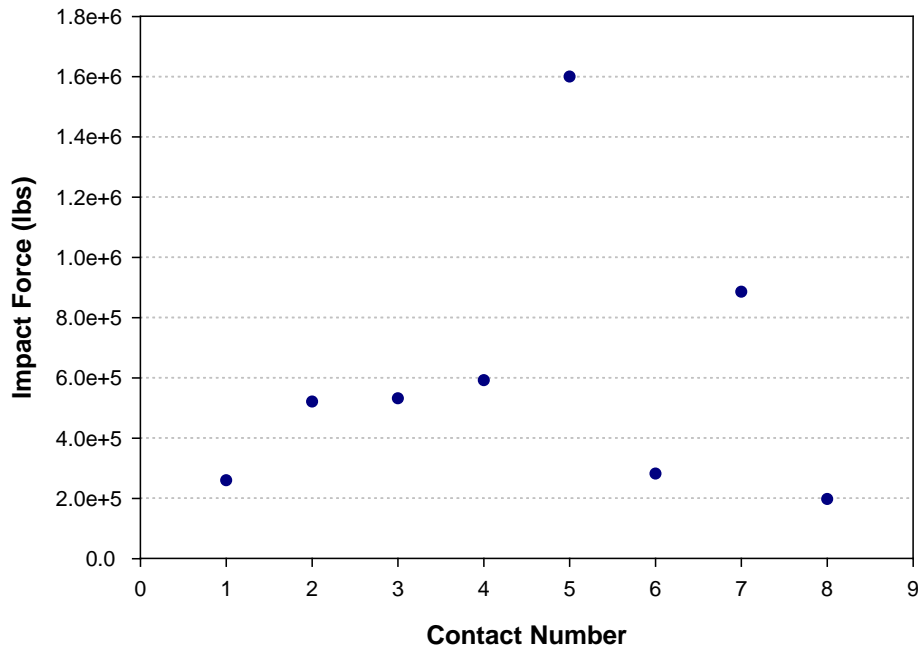


**Figure 21. Impact Forces for Secondary Contact**

## 2.5 Discussion and Summary

Lumped-parameter models were developed to examine the gross motions of rail cars in generalized train derailments. Two different models were developed for this purpose, a purpose-built FORTAN model and a model developed using commercial software called ADAMS, which produced similar results for the same inputs. The similarity of results from the two models suggests that the dynamics are being correctly calculated for the assumed scenarios.

However, the assumptions at best provide only a simplified representation of actual conditions. For example, the actual terrain at a derailment site is unlikely to be perfectly level; also, the effective friction between derailed rail cars and the ground is likely to vary. Thus, the models provide a general representation but do not reproduce specific derailment events.

Nevertheless, the general results can provide some useful insights. For example, the closing velocities between cars engaging in post-derailment collisions appear to average about half the initial speed of the train.

Another general result is that train speed appears to be the most important variable. When the assumed train speed is increased by a factor of 3 (18 to 54 mph) in a series of cases, the derailment dynamics models calculate following outcomes: (1) the number of derailed cars increased by a factor of 4, (2) maximum closing speed for car-to-car

collisions increases by a factor of 2.5, and (3) peak collision force increases by a factor of 6.

The derailment dynamics models are used to examine post-derailment, car-to-car impacts. That is, rail cars collide with other cars as they come off the tracks in the simulated derailment. Moreover, the simulations produce car-to-car impacts that generally occur in accidents leading to the release of hazardous materials; namely, head and shell impacts. Figure 22 shows three particular instants in time from a generalized derailment simulation in which the post-derailment, car-to-car impacts can be simplified to a head impact and two shell impacts, one near the center of the tank and one near an end. Moreover, the simplified or generalized car-to-car impacts scenarios are used to examine the response of the tank structure for a prescribed closing speed.

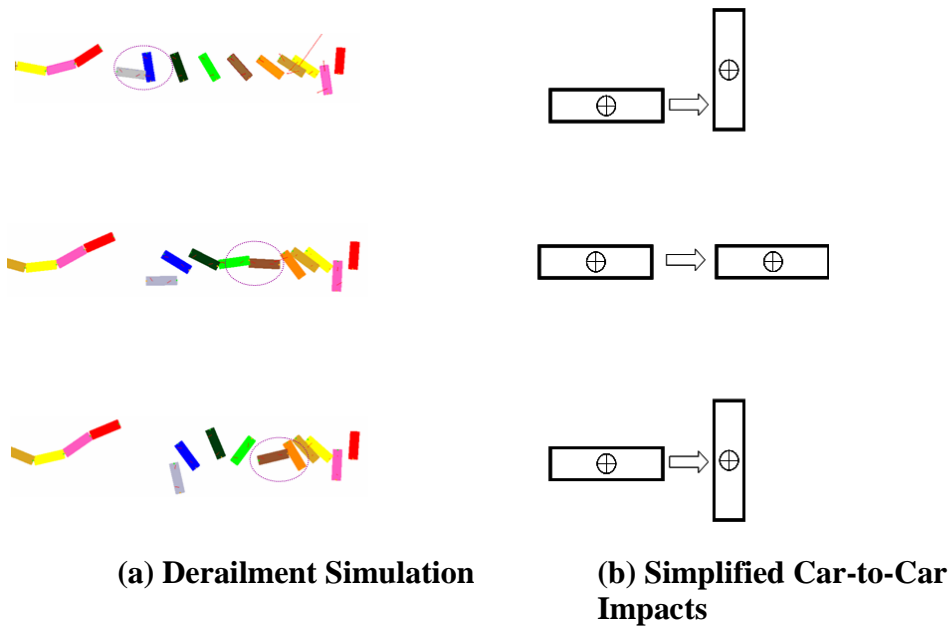


**Figure 22. Simulated and Generalized Car-to-Car Impact Scenarios**

Figure 23 shows still photographs taken from a surveillance video that captured the occurrence of an actual freight train derailment. The sequence of the stills shows the evolution of the derailment pile-up and car-to-car impacts, which are similar to those produced by the derailment dynamics models. The similarity between actual and simulated car-to-car collisions provides confidence in the models for derailment dynamics, and suggests that they have been verified and validated.

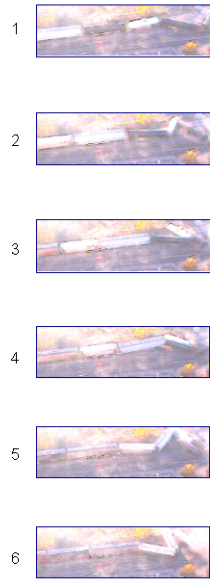


**Figure 23. Stills from Surveillance Video of an Actual Train Derailment**

### 3. Structural Finite Element Analysis

The physics of impact are modeled using dynamic, nonlinear finite element analysis (FEA). In the present context, nonlinear means elastic-plastic material behavior with large deformations. Finite element models of different tank car components, such as the head and the shell of the tank, are developed to examine their structural behavior when impacted by different objects (such as couplers, wheels, etc.). In general, structural behavior is quantified as force as a function of indentation, or force-indentation characteristic. Moreover, two commercial general-purpose finite element software programs for linear and nonlinear, static and dynamic analysis are used for this purpose: LS-DYNA [14] and ABAQUS [15].

The development of computational models that include impact dynamics as well as nonlinear material behavior is labor intensive. The combination of finite difference in time and nonlinear material behavior makes it difficult in practice to obtain good model performance without assuming extremely small time steps, which affects computational time. Therefore, the primary technical challenge in the present work is to develop an accurate and efficient model within practical computational limits.

Solutions to structural behavior in dynamic, nonlinear FEA are achieved through direct integration methods, also referred to as step-by-step methods, which use a finite difference approximation to replace the time derivative at various time steps. The finite difference methods for direct integration can be either implicit or explicit. Implicit integration requires an iterative solution process to ensure equilibrium at each time step, and is unconditionally stable. The iterative process may require high computational time. No iterations are performed in explicit integration, but the time step assumed in the solution must be smaller than the critical time step for the solution to be stable. Moreover, explicit integration is conditionally stable. The critical time step varies during the solution process because it depends on the geometry and material conditions that change during the analysis. The number of time steps for explicit integration may be 100 to 10,000 times more than would be used in an implicit calculation. If a step size larger than the critical time step is assumed in an explicit calculation, errors can accumulate and grow, ultimately leading to numerical instability of the solution.

In linear problems, numerical instabilities in finite element analysis are self-evident because the solution grows without limit. In nonlinear problems, with elastic-plastic or other energy dissipating materials, extra energy introduced into the system by numerical instabilities may be dissipated by plastic work, which makes it possible for the instability to be arrested. An arrested instability, which may be in error by 10 to 100 percent or more, may appear to be reasonable [16].

Elastic-plastic material behavior is generally modeled using the Ramberg-Osgood equation for strain as a function of stress:

$$\varepsilon = \frac{\sigma}{E} + \left( \frac{\sigma}{K} \right)^n \quad (1)$$

where  $\varepsilon$  is the strain,  $\sigma$  is the stress, and  $E$  is the modulus of elasticity (30,000 ksi assumed for tank car steel). Also,  $n$  and  $K$  are material constants. Table 2 lists the assumed values of these constants for different tank car steels. The table also lists the assumed values for yield strength and ultimate tensile strength, which correspond to the minimum requirements for these steels.

**Table 2. Mechanical Properties and Constants Assumed for Tank Car Steels**

	$n$	$K$ (ksi)	Yield Strength (ksi)	Tensile Strength (ksi)
TC-128B	9.41	96.8	50	81
AAR M-115	6.65	73.1	30	60
A516-70	8.08	82.0	38	70
A710	20.4	104.3	80	90
HPS70	11.9	118.2	75	96
HPS100	20.8	137.3	107	119

The various activities to build credibility into computational models are collectively referred to as Verification and Validation (V&V). The V&V activities described in this report are developed with specific objectives for each modeling phase, and do not adhere to any specific recommended guidelines or standards.<sup>2</sup> In this context, verification means assessing the accuracy of the solution from the computational models by comparison with known solutions. Validation means assessing the accuracy of a computational simulation by comparison with data. Moreover, verification deals with the mathematics associated with the model, and validation deals with the physics of the model [17]. Clearly verification and validation are separate activities, but verification precedes validation.

Head indentation models are validated through comparisons with data obtained from head impact tests conducted by the Railway Progress Institute (RPI) and the Association of American Railroads (AAR) Tank Car Safety Research and Test Project in the 1970s [19]. Shell indentation models are validated through comparisons with measurements from full-scale shell impact tests that were conducted as part of the Next Generation Rail Tank Car Project [20] in 2007.

### 3.1 Verification

A numerically stable and accurate solution within practically reasonable computational times is affected by choices made in the modeling development regarding type of element, mesh density (element aspect ratio), and order of quadrature (i.e., fully

<sup>2</sup> Professional organizations, such as the American Institute of Aeronautics and Astronautics and the American Society of Mechanical Engineers (ASME) [18] are actively developing guidelines for assessing the credibility of modeling and simulation in computational fluid dynamics and solid mechanics, respectively.

integrated elements or reduced integration to calculate element stiffness). Regular shapes generally provide greatest accuracy. Thus, in a good mesh, most elements would be approximately square in two dimensions or cubes in three dimensions. Moreover, grid or mesh convergence is a part of the verification process in the development of FEA models. Sensitivity studies are conducted to examine the effect of varying element type, element aspect ratio, and order of integration or quadrature on the calculations of force-indentation behavior. In addition, FEA results are compared with known closed-form solutions to relatively simple structures (i.e., flat circular plates and ellipsoidal caps).

### **3.1.1 Sensitivity Studies**

Numerical experiments are conducted to examine the effect of development options on force-indentation behavior and computational times. The effect of these options on equivalent plastic strain is also examined, which is necessary in order to develop a criterion for material failure. Moreover, the development options that are examined in these numerical experiments or sensitivity studies are:

- (1) Commercial FEA Code: Do ABAQUS and LS-DYNA give comparable results?
- (2) Static and Dynamic Analyses
- (3) Element Type: Solid or Shell Elements
  - (a) Element aspect ratios and through-the-thickness layers for solid elements
  - (b) Element sizes and through-the-thickness integration points for shell elements
- (4) Integration Scheme: Full or Reduced Integration

Generally speaking, shell elements are commonly used to model thin-walled structures. Shell elements are formulated to include or neglect transverse shear deformations which affect resistance to bending. When shell elements are used, the number of integration points through the thickness must be specified to calculate the element stiffness via numerical integration (i.e., quadrature). A shell element may be regarded as a special form of a solid element made thin in one direction. Alternatively, three-dimensional solid elements may be used but the number of elements through the thickness must be chosen judiciously to account for bending properly.

In principle, finer mesh and more integration points tend to provide more accurate solutions in finite element modeling, but increase computational time. Modeling options are also restricted by available computer resources. The following in-house computers were used in the sensitivity studies:

- (1) Dual Intel Xeon (64 bit), 2×3.6 GHz, 8 GB Memory,
- (2) Dual Intel Xeon (32 bit), 2×3.4 GHz, 4 GB Memory, and
- (3) Intel Xeon (32 bit), 3.4 GHz, 2 GB Memory.

Finite element models of a tank car head impacted by a rigid coupler are developed for the sensitivity studies. The relevant parameters of the head impact models are listed in

Table 3.

**Table 3. Parameters for Simulated Head Impact Sensitivity Studies**

<i>Parameter</i>	<i>Value</i>
Tank head diameter	83 inches
Head thickness	0.4375 inch
Aspect ratio of ellipsoidal cap	2 to 1
Tank car weight	40,900 lb
Ram car weight	128,900 lb
Material	AAR M-115
Impact location	Center of head
Impact speed	8.5 mph

Simplifying assumptions are made in the sensitivity studies. For example, a fixed boundary condition is applied along the interface between the impacted head and the remaining structure which is not modeled. The backup cars are not included in the model. The ram car is modeled as a rigid body with a distributed mass. Scanned images of a coupler deformed during an accident are digitally processed to generate the shape of the impactor. Although the shape of the coupler is asymmetrical, a quarter-symmetric model of the tank car head was modeled for simplicity.<sup>3</sup>

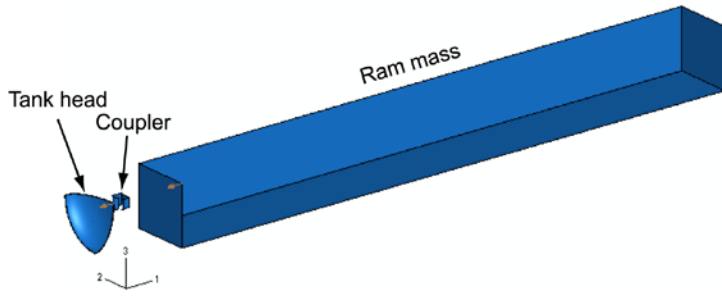
Figure 24(a) shows a schematic of the entire dynamic simulation. Figure 24(b) shows a zoomed view of the impact zone. Similarly, static analyses are conducted on the same tank car head (Figure 25) with the same boundary conditions as the dynamic simulations. In the static analyses, a traction load is applied over a circular area (93 square inches (in)) at the center of the head.

Both static and dynamic analyses are conducted to calculate the global force-indentation response and the distribution of equivalent plastic strain. In the static analyses, force is a resultant of the traction load. In the dynamic analyses, force is derived from the contact force output. The simulation time for the dynamic analyses is set to 0.35 seconds.

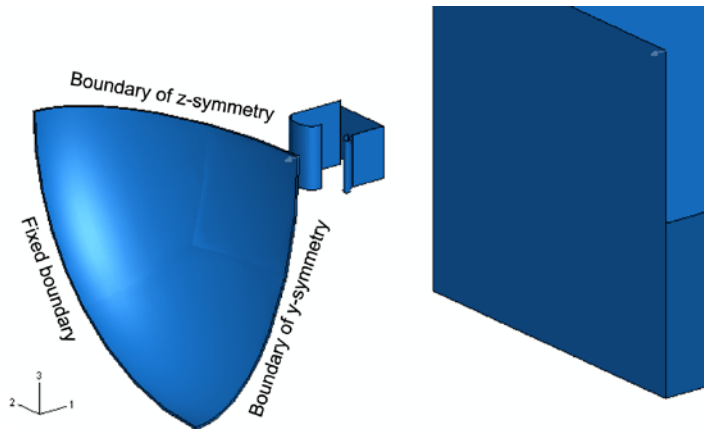
Table 4 lists the results from the sensitivity analyses using ABAQUS. The analyses are grouped according to analysis type (static or dynamic), element type (solid or shell), integration scheme (full or reduced), element aspect ratio for solid elements or element size for shells, and through the thickness characteristics (number of layers for solids and number of integration points for shells). For each analysis case, the exact computational or CPU time was recorded. The CPU time in the table was rounded to the nearest day or week. Similarly, Table 5 shows the results from the sensitivity analyses using LS-DYNA.

---

<sup>3</sup> Strictly speaking, the asymmetrical shape of the coupler does not warrant a quarter-symmetric model. This approach is reasonable for the purpose of comparative studies.



(a) Full View



(b) Zoomed View

**Figure 24. Schematic of Dynamic Simulations for Sensitivity Studies**

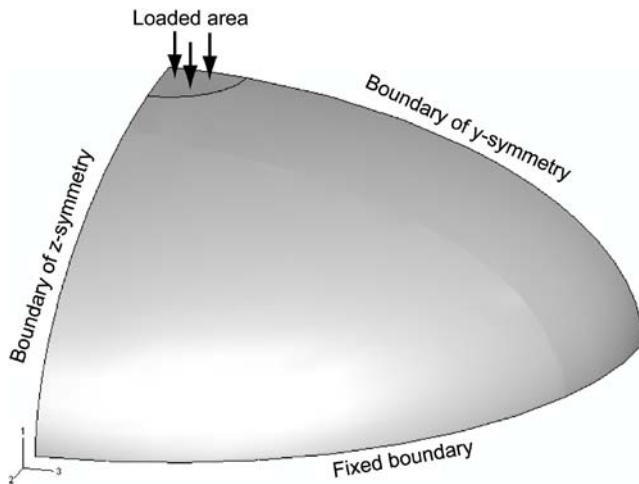


**Figure 25. Schematic of Static Analysis for Sensitivity Studies**

**Table 4. Results from Sensitivity Analyses using ABAQUS**

Analysis type	Element type	Integration scheme	Element aspect ratio or size <sup>(1)</sup>	Through the thickness characteristics	CPU time
Static	Solid	Full	1:1	1 layer	<1 day
				2 layers	1-3 days
				3 layers	1-2 weeks <sup>(2)</sup>
	Shell	Full	1 <i>t</i>	2 points	<1 day
				3 points	<1 day
				4 points	<1 day
				5 points	<1 day
			0.5 <i>t</i>	3 points	1-3 days
Dynamic	Solid	Full	1:1	1 layer	<1 day
			2:1	2 layers	1-3 days
		Reduced with enhanced hourglass control	1:1	1 layer	<1 day
			1:1	2 layers	3-7 days
			2:1	2 layers	<1 day
			3:1	3 layers	1-3 days
			4:1	2 layers	<1 day
			4:1	4 layers	1-3 days
	Shell	Full	2 <i>t</i>	3 points	<1 day
			1 <i>t</i>	2 points	1-3 days
				3 points	
				4 points	
				5 points	<1 day <sup>(3)</sup>
				6 points	<1 day
			7 points	<1 day	
15 points <sup>(4)</sup>	<1 day				
0.5 <i>t</i>	3 points	3-7 days <sup>(5)</sup>			
1 <i>t</i> with 0.5 <i>t</i> local refinement <sup>(6)</sup>	5 points	1-3 days			
1 <i>t</i> with <i>t</i> /3 local refinement <sup>(7)</sup>	5 points	1-2 weeks			

<sup>(1)</sup> Refers to general characteristics of a mesh, whereas individual element characteristics may vary.

<sup>(2)</sup> Estimated for the simulation to reach a force level of 400 kips. Owing to an unknown system error, actual simulation was aborted after about 4.5 days with partial result obtained with a maximum force of 187 kips.

<sup>(3)</sup> Mass scaling technique was employed to increase the stable time increment from  $3.8 \times 10^{-7}$  to  $8 \times 10^{-7}$ , thus decreasing the CPU time from 1-3 days to <1 day. The resulting mass increase is 0.44 lb or 0.19 percent of the head mass.

<sup>(4)</sup> Simpson's rule was applied in this case, whereas Gauss quadrature was applied in all the other shell cases.

<sup>(5)</sup> Mass scaling technique was employed to increase the stable time increment from  $1.7 \times 10^{-7}$  to  $4 \times 10^{-7}$ , thus decreasing the CPU time from an estimated 2 weeks to 5.7 days. The resulting mass increase is 0.42 lbs or 0.18 percent of the head mass.

<sup>(6)</sup> A 10×10-square-inch area in the impact center was meshed with a characteristic element size of 0.5*t*, whereas the remaining mesh was transitioned to a characteristic element size of 1*t*.

<sup>(7)</sup> A 10×10-square-inch area in the impact center was meshed with a characteristic element size of *t*/3, whereas the remaining mesh was transitioned to a characteristic element size of 1*t*.

**Table 5. Results from Sensitivity Analyses using LS-DYNA**

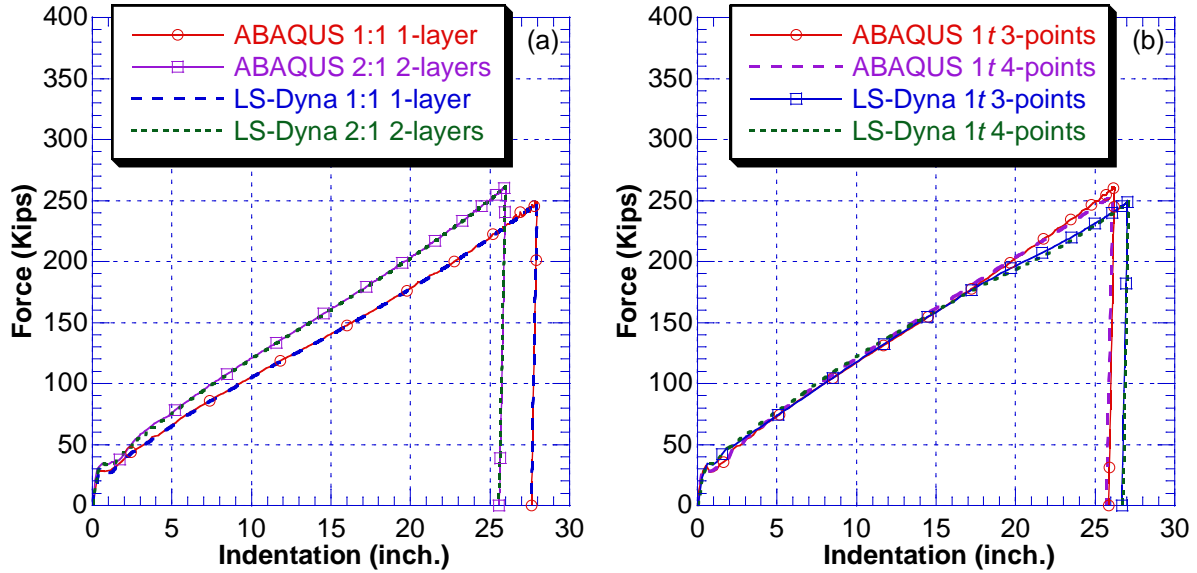
Analysis type	Element type	Integration scheme	Element aspect ratio or size	Through the thickness characteristics	CPU time
Dynamic	Solid	Full	1:1	1 layer	<1 day
			2:1	2 layers	<1 day
			1:1	2 layers	3-7 days
			1:1	3 layers	2 weeks
		Reduced w/ default hourglass control	2:1	2 layers	<1 day
			4:1	2 layers	<1 day
	8:1		2 layers	<1 day	
	Shell	Full	1t	2 points	<1 day
				3 points	<1 day
				4 points	<1 day
5 points				<1 day	

Static analyses were conducted using ABAQUS/Standard. For solid elements, only 1:1 aspect ratio was considered, and 1 to 3 layers of elements were developed. For shell elements, two element sizes were considered:  $1t$  and  $0.5t$ , where  $t$  is the head thickness. The number of integration points for the shell elements ranged from 2 to 5. CPU times for analyses using shell elements were comparable to those using solid elements with similar mesh refinement.

Dynamic analyses were conducted using ABAQUS/Explicit and LS-DYNA. In certain cases, the dynamic analyses for solid elements used reduced integration. At the same level of mesh refinement, a dynamic analysis is generally more time consuming than a static analysis.

### Commercial Codes

Comparisons between results from ABAQUS and LS-DYNA verify the accuracy of both codes. Figure 26(a) shows results from dynamic analyses using solid elements with two different meshes (1:1 element aspect ratio and 1 layer of elements through the thickness compared with 2:1 element aspect ratio and 2 layers) from both codes. Figure 26(b) shows results from dynamic analyses using shell elements with different integration points through the thickness. The full-integration scheme is used to produce the results shown in these figures. Moreover, ABAQUS and LS-DYNA produced results that are nearly indistinguishable in the solid element cases. In the shell element cases, results from ABAQUS and LS-DYNA are nearly identical up to an indentation of about 17 in, beyond that the LS-DYNA results appear to be more compliant, with lower maximum forces and higher maximum and residual indentations, than the ABAQUS results. The differences in maximum forces and maximum and residual indentations between the two programs are within 6 percent.



(a) Using Solid Elements

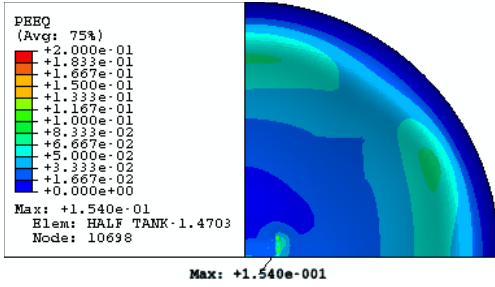
(b) Using Shell Elements

**Figure 26. Comparison of Force-Indentation Results**

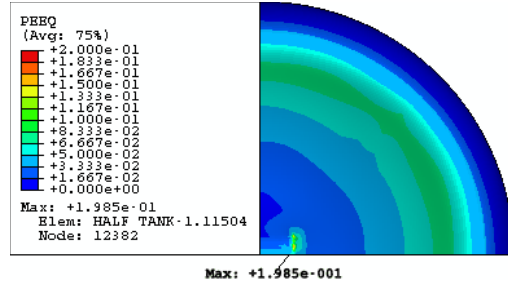
Figure 27 compares contours of equivalent plastic strain from different meshes using solid elements. Figure 28 compares contours from using shell elements. More specifically, residual equivalent plastic strains are plotted in these contours. The upper limit of the contour plots was set to 0.2 in all cases. The two finite element programs using either solid or shell elements predicted the same location of maximum equivalent plastic strain; for instance, along the coupler's shorter edge in contact with the tank head. In the case of solid elements, the general trends of the distributions for equivalent plastic strain over the entire domain of interest are similar. In the case of shell elements, however, the maximum equivalent plastic strains are similar in magnitude but the contour distributions appear to show larger variations.

### Static and Dynamic Analyses

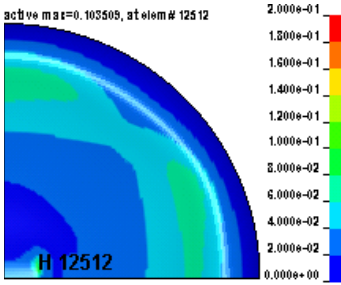
Figure 29 compares the force-indentation responses obtained from static and dynamic finite element analyses. Figure 29(a) shows the results using 1 or 2 layers of solid elements through the thickness of the tank head and an element aspect ratio of 1:1. Figure 29(b) shows the results using shell elements with an element size of  $1t$  and 3 integration points through the thickness. Dynamic responses are expected to be stiffer than static responses due to inertial and frictional effects especially at larger indentations. The dynamic stiffening is evident in the shell element and 1-layer solid element cases, but the 2-layer solid element case displays the opposite; i.e., the static response is somewhat stiffer than the dynamic case. Use of solid elements will be discussed further in subsequent subsections.



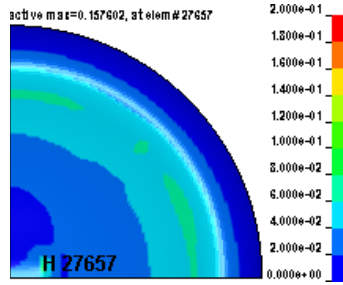
(a) ABAQUS Solid 1:1 1-layer



(b) ABAQUS Solid 2:1 2-layers

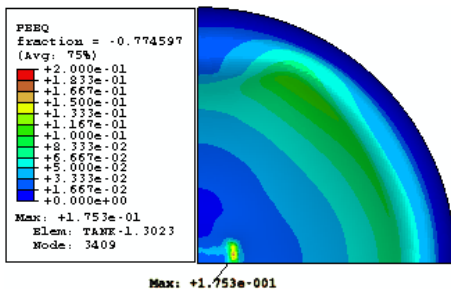


(c) LS-DYNA Solid 1:1 1-layer

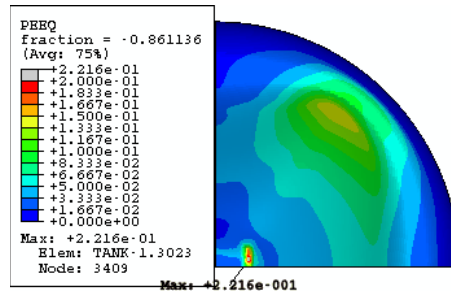


(d) LS-DYNA Solid 2:1 2-layer

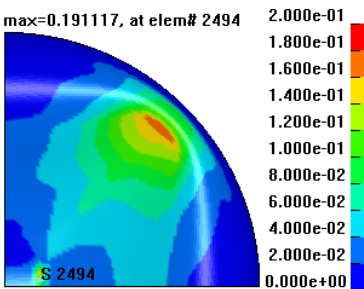
**Figure 27. Contours of Equivalent Plastic Strain using Solid Elements**



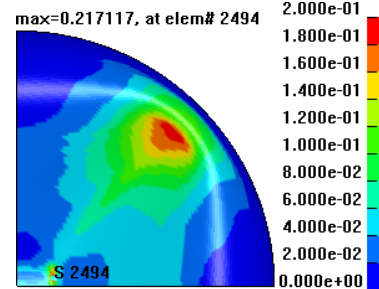
(a) ABAQUS Shell 1t 3-points



(b) ABAQUS Shell 1t 4-points

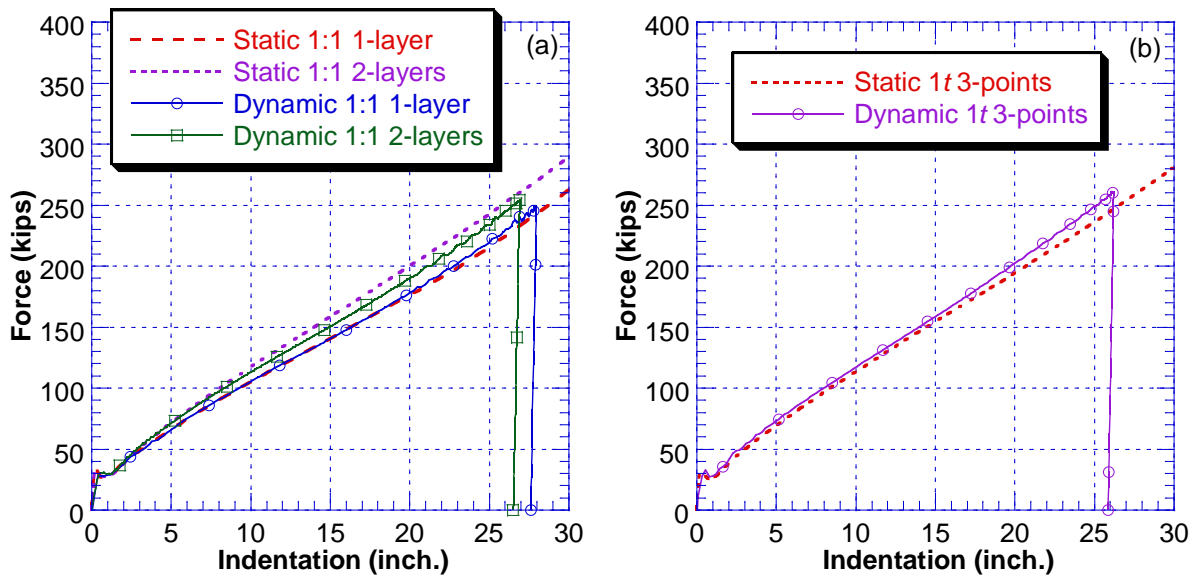


(c) LS-DYNA Shell 1t 3-points



(d) LS-DYNA Shell 1t 4-points

**Figure 28. Contours of Equivalent Plastic Strain using Shell Elements**



(a) Using Solid Elements

(b) Using Shell Elements

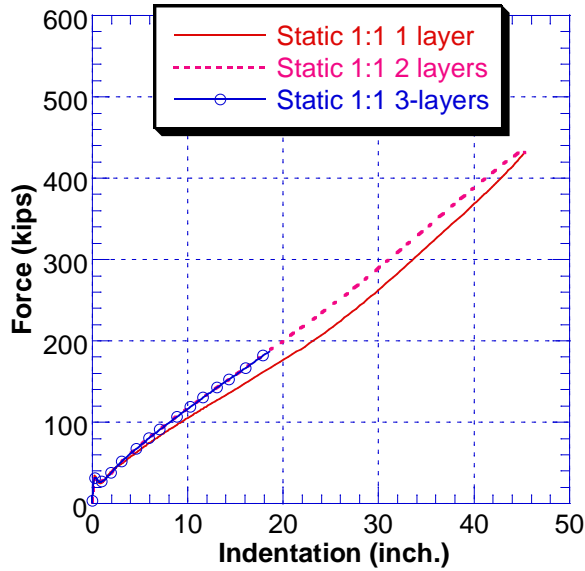
**Figure 29. Comparison between Static and Dynamic Finite Element Analyses**

### Solid elements

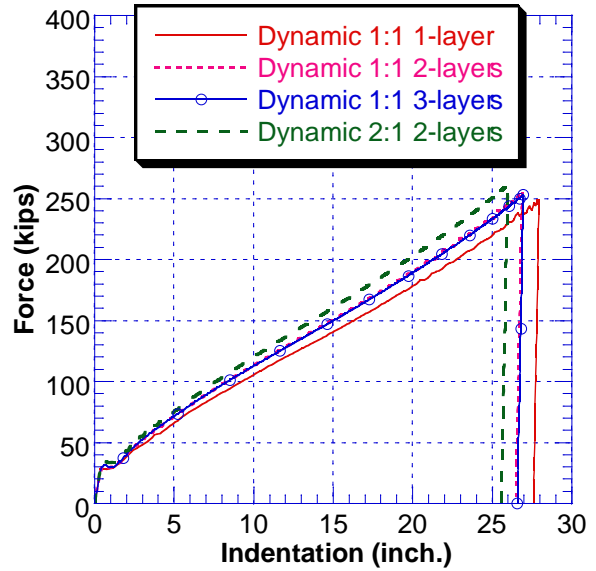
Figure 30 compares results using solid elements with different meshes in both static and dynamic analyses. In the static case, the curve for 3 layers of elements through the thickness is incomplete for the reason stated in footnote (2) of Table 4. The available results for 2 and 3 layers of elements through the thickness are nearly identical, suggesting that results are converging as the characteristic element size becomes smaller. This is true in both static and dynamic analyses.

Stiffer responses are expected for poor element aspect ratios due to shear locking. This is confirmed by the results for the dynamic analyses. The force-indentation curve corresponding to a 2:1 element aspect ratio is stiffer than the others.

Figure 31 shows the contour plots for equivalent plastic strain from dynamic analyses using four different meshes. While all four contour plots show strain localization in the same general area at which impact occurs, the distribution over the whole domain is somewhat different in each. The contour plots for 2 and 3 layers of elements through the thickness with an aspect ratio of 1:1 show similar maximum values for equivalent plastic strain and somewhat similar distributions over the whole domain.

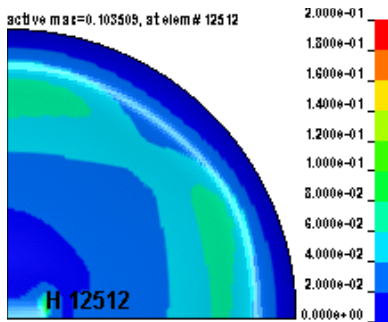


(a) Static Analysis

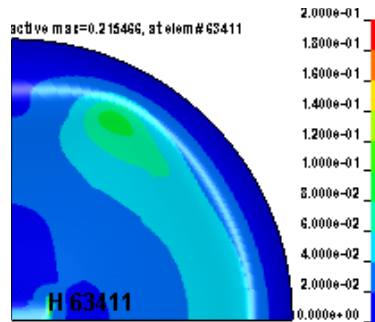


(b) Dynamic Analysis

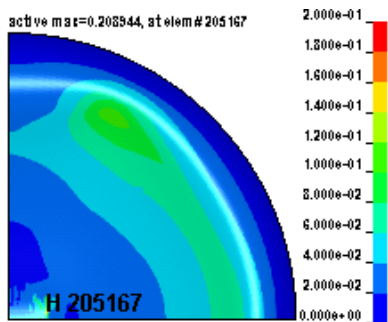
**Figure 30. Comparison between Static and Dynamic Finite Element Analyses**



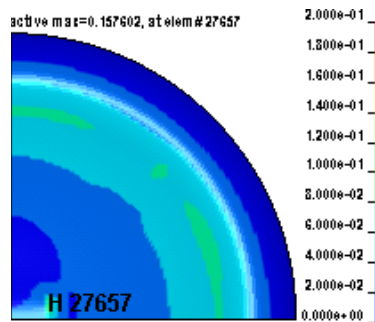
(a) Solid 1:1 1-layer



(b) Solid 1:1 2-layers



(c) Solid 1:1 3-layers



(d) Solid 2:1 2-layers

**Figure 31. Contours of Equivalent Plastic Strain from Dynamic Analysis using Shell Elements**

## Shell Elements

Sensitivity to mesh size and the number of integration points through the thickness was examined for shell elements. Figure 32 compares static analyses for (a) a fixed mesh size (equal to  $1t$ ) and varying number of integration points through the thickness (between 2 and 5), and (b) a fixed number of integration points (equal to 3) and varying mesh sizes ( $0.5t$  and  $1t$ ). Figure 33 shows the same comparison for dynamic analysis (with an additional mesh size of  $2t$ ). Based on the global force-indentation behavior, convergence appears to be achieved with three integration points and a mesh size of  $2t$ . The noise in the curve for an element size of  $0.5t$  is attributed to increased time increments as a result of mass scaling as described in footnote (5) of Table 4.

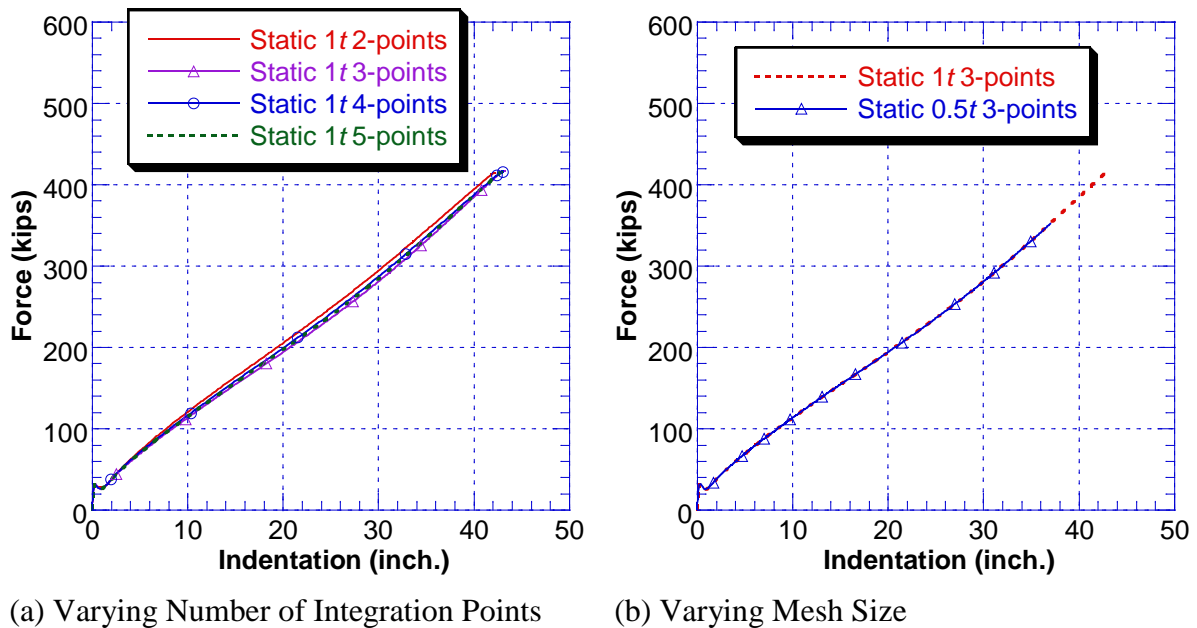
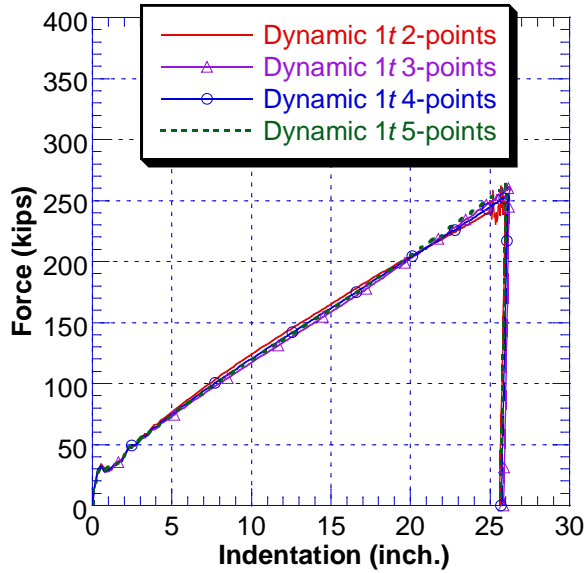


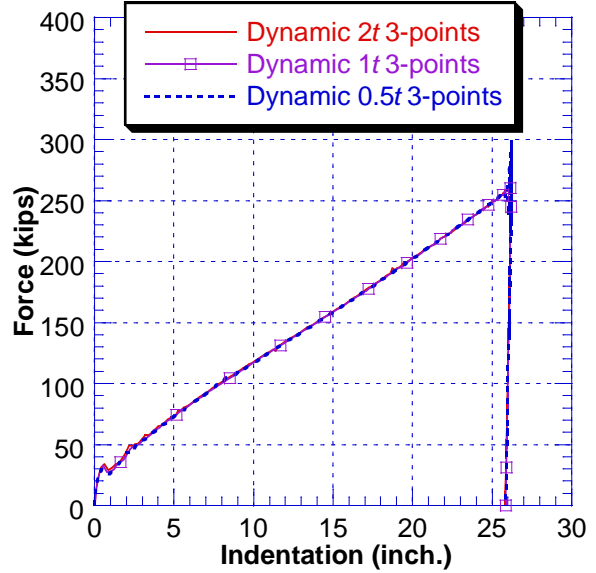
**Figure 32. Comparison Force-Indentation Curves from Static Analysis using Shell Elements**

## Solid versus Shell Elements

Figure 34 compares force-indentation curves obtained from (a) static analyses and (b) dynamic analyses using typical meshes for solid and shell elements. The static results shown in Figure 34(a) are almost identical.

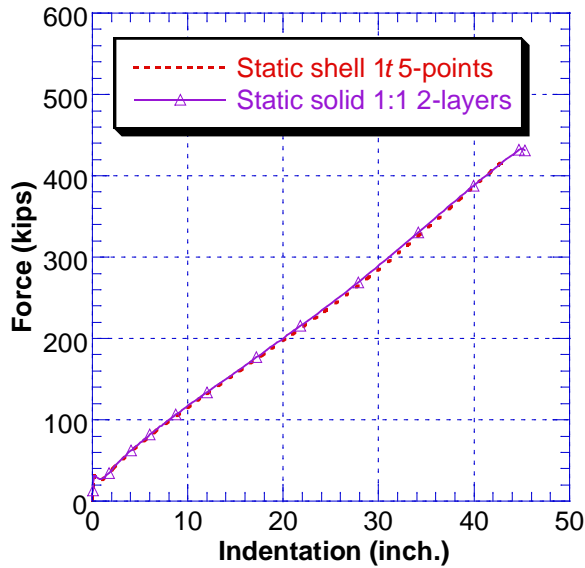


(a) Fixed Mesh Size and Varying Integration Points Through the Thickness

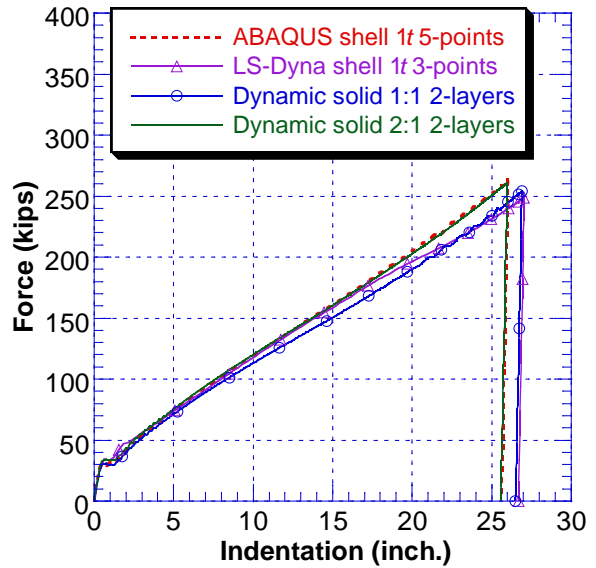


(b) Fixed Number of Integration Points and Varying Mesh Size

**Figure 33. Comparison Force-Indentation Curves from Dynamic Analysis using Shell Elements**



(a) Static Analyses



(b) Dynamic Analyses

**Figure 34. Force-Indentation Curves from Static and Dynamic Analysis using Solid and Shell Elements**

## Full versus Reduced Integration

Quadrature is used in finite element analysis to calculate the volume of each element which in turn is needed to determine the element stiffness. If the element shape is regular (i.e., straight edges) and cube-like (in three-dimensions), the element volume and stiffness can be calculated accurately. As the element shape deviates from a cube (i.e., as the height-to-width ratio, or element aspect ratio, increases), the element tends to stiffen and lose accuracy. A lower-order quadrature rule, called reduced integration, may be desirable. Since the expense of generating a stiffness matrix by numerical integration is proportional to the number of sampling points, using fewer sampling points means lower cost. A low-order rule tends to soften an element because strain energy of higher order deformation modes is not accounted for. However an inherent danger in using low-order integration is that zero-energy deformation modes may arise.

Single-point integration elements combined with various hourglass control methods may produce global force-indentation curves that are similar to those obtained using fully integrated elements, but the distributions for equivalent plastic strain are inconsistent. The so-called enhanced hourglass control in ABAQUS appears to provide reasonable strain distributions but the global force-indentation curves are much stiffer than LS-DYNA. Use of reduced integration elements is recommended only for qualitative studies.

## Summary

Based upon the foregoing verification studies, the following conclusions regarding the estimation of global force-indentation curves were drawn.

- (1) The solid element formulations in ABAQUS and LS-DYNA produce nearly identical results in dynamic analyses.
- (2) The solid element results converge at a characteristic element size of  $0.5t$  (1:1 element aspect ratio, two layers through the thickness), in both static and dynamic analyses.
- (3) The results using shell element in ABAQUS converge at a characteristic element size of  $1t$  and 3 integration points through the thickness, in both static and dynamic analyses.
- (4) Results from static analyses using solid and shell elements are in good agreement.
- (5) Using solid elements, the structural response tends to stiffen as the element aspect ratio increases, most likely due to the shear locking effect.
- (6) Maximum forces and indentations calculated using ABAQUS solid elements are within 4 percent ABAQUS shell element results.
- (7) Maximum forces and indentations calculated by LS-DYNA using shell elements are within 6 percent of ABAQUS shell element results.

In addition, the following conclusions regarding the contours of equivalent plastic strain based on ABAQUS shell analyses are drawn.

- (1) Six Gaussian integration points through the thickness are recommended.

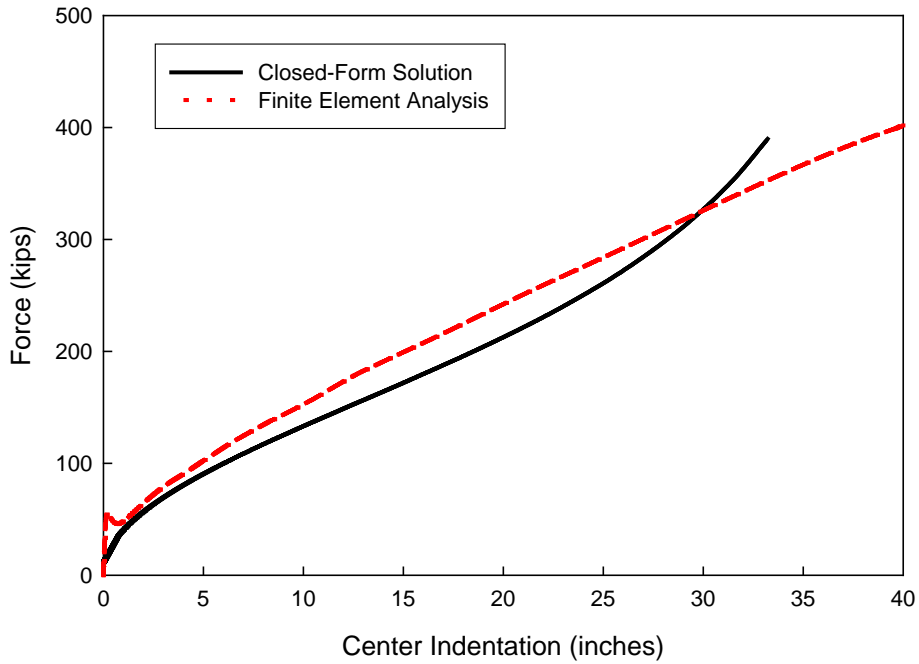
- (2) The predicted locations of the maximum equivalent plastic strain are consistent for element sizes less than or equal to  $1t$ .
- (3) The magnitude of the maximum equivalent plastic strain increases as the mesh becomes finer.
- (4) A separate sensitivity analysis is needed to examine the mesh sensitivity on assumed failure criteria.

### **3.1.2 Static Case Studies**

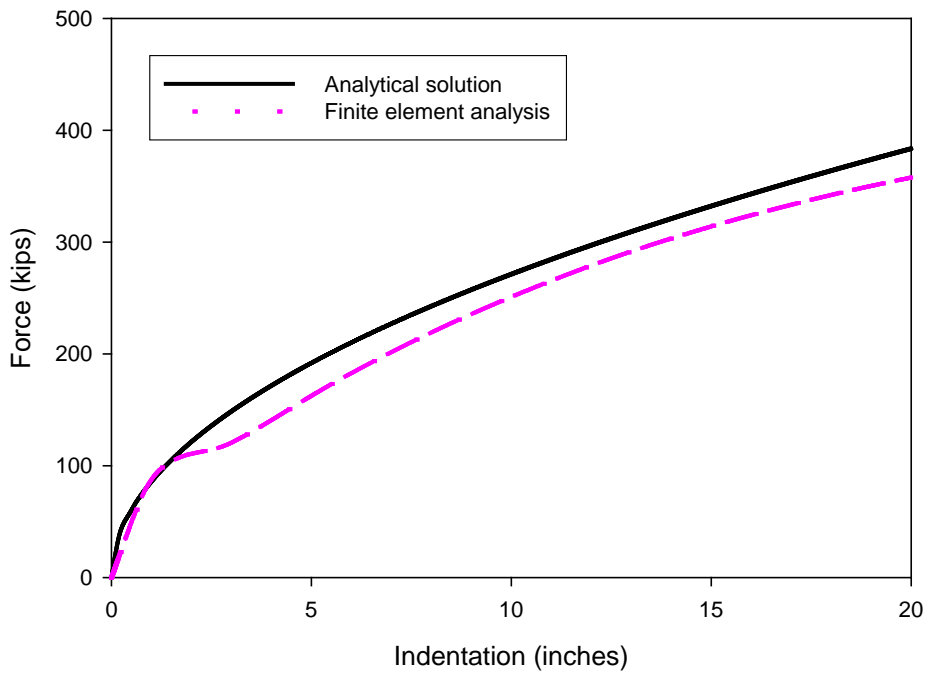
As part of the verification process, results from static FEA models are compared to known closed-form solutions for relatively simple cases. The verification case for the head deformation model is the rigid-plastic collapse of an ellipsoidal cap with a concentrated load applied at its apex. An analytical solution to the rigid-plastic rotationally symmetric deformation of a non-pressurized hemispherical shell was developed by de Oliveria and Wierzbicki [21]. The solution was modified for ellipsoidal shells.

Figure 35 compares the force-deflection response from the closed-form solution and the finite element analysis. The ellipsoidal cap has an aspect ratio (major-axis length to minor-axis length) of 2 to 1, diameter of 87.5 in, thickness of 0.5 in. In the FEA model, the applied load is distributed over a 1-square-foot area at the center of the cap. In the closed-form solution, the applied load is assumed to be a concentrated load applied at the center of the shell. The closed-form solution also assumes a flow stress, which is a material property used to define the rigid-plastic limit. In the present case, the flow stress is assumed to be equal to the yield strength of the material (30 ksi). The solution algorithm in the finite element analysis uses Riks method [22], which is efficient when the static load-deflection curve is expected to exhibit snap-through or snap-back behavior. Considering the differences in applied loading (concentrated versus distributed load) and material behavior (rigid-plastic versus elastic-perfectly-plastic), the comparison appears to show reasonable agreement.

Wierzbicki and Suh [23] developed theoretical analyses of large plastic deformation of cylindrical tubes subjected to various loading conditions, including lateral loads, which may be used as a verification case for the shell impact model. The closed-form solution is sensitive to the assumed boundary conditions. Figure 36 compares the force-indentation curve obtained from the closed-form solution for a cylinder subjected to lateral loading with a static, nonlinear finite element calculation. The cylinder is assumed to be supported by a rigid surface on the side opposite from the applied load, and is free to slide and rotate at its ends.



**Figure 35. Comparison of Force-Indentation Curves for Center Loaded Ellipsoidal Cap**



**Figure 36. Comparison of Force-Indentation Curves for Cylindrical Shell**

### **3.1.3 Dynamic Case Studies**

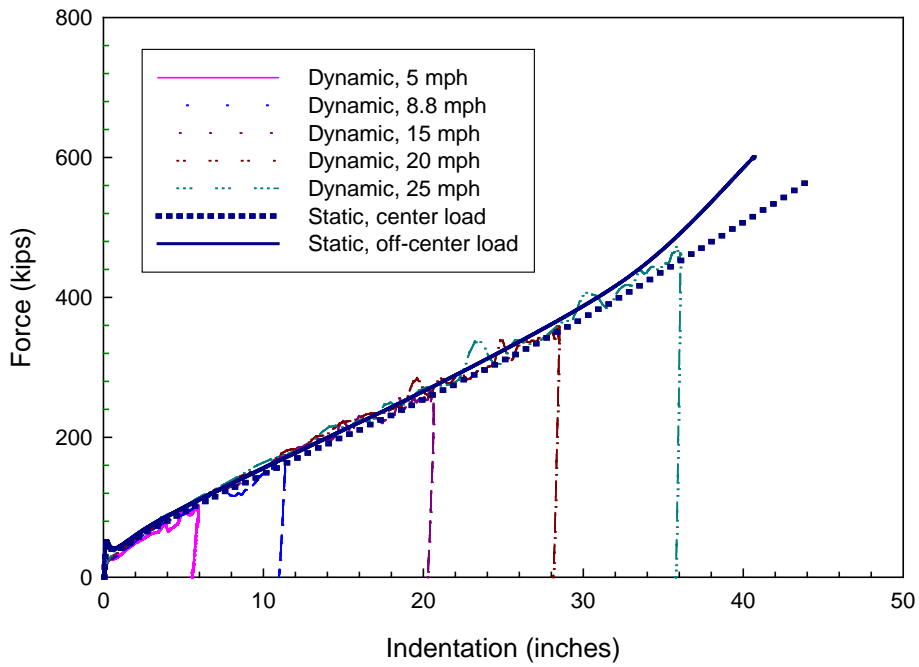
Results from static and dynamic FEA are compared for additional verification of the modeling development. Figure 37 shows force-indentation curves for head impacts calculated by static and dynamic FEA. In the dynamic cases, off-center impacts are simulated at five different speeds. In the static cases, the location of load application was varied. Moreover, the figure shows that static and dynamic FEA produce practically the same force-indentation characteristic for head impacts. Similarly, Figure 38 shows that static and dynamic FEA calculate similar force-indentation characteristics for shell impacts.

The combination of finite difference in time to capture dynamics and nonlinear stress-strain analysis to capture elastic-plastic material behavior makes it difficult in practice to obtain good model performance without assuming extremely small time steps in FEA. Therefore, lumped-mass modeling was conducted to verify the dynamic, nonlinear FEA. For example, the spring characteristic in Figure 39 may represent the structural stiffness of the tank car head. Moreover, static nonlinear FEA is used to calculate the force-indentation curve for an ellipsoidal end cap, which is then used as the spring characteristic in the dynamic lumped-mass model.

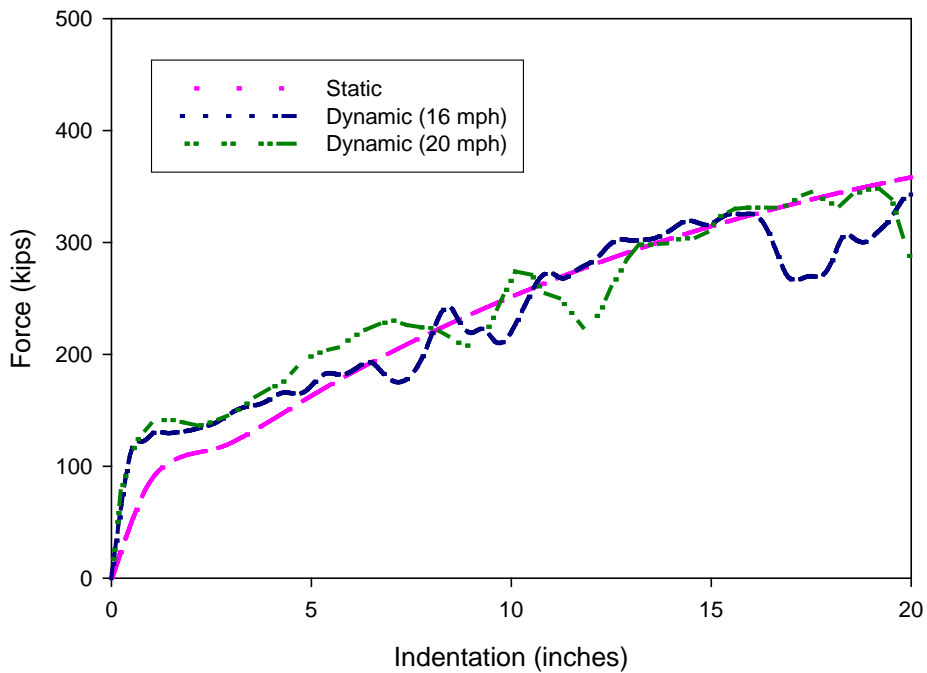
Another alternative method to examine the structural response of the tank car head to impact is semi-empirical analysis. In addition to conducting tank car head impact tests, the RPI-AAR Tank Car Safety Research and Test Project conducted regression analyses with the head impact test data to develop equations for estimating impact force and indentation as functions of impact velocity or closing speed. The theoretical basis of these equations is Hertz contact. The equations derived from the regression analyses in combination with the theory of Hertz contact are referred to as the semi-empirical equations.

Figure 40 shows results from three different methods to calculate impact force as a function of closing speed on empty tank heads: (1) the solid line represents results from the semi-empirical equations; (2) the open square symbols represent results from the dynamic lumped-mass model; and (3) the solid triangles represent results from the dynamic, nonlinear FEA. The solid circles represent the test measurements.

Comparison of the dynamic nonlinear FEA calculations with the semi-empirical formula developed by the RPI-AAR shows that the latter accurately predicts the peak collision force for engagements at closing speeds from 7 to 15 mph. Also, for closing speeds from 15 to 25 mph, the RPI-AAR semi-empirical formula predicts forces somewhat greater than those predicted by the finite element analyses.



**Figure 37. Comparison between Static and Dynamic FEA for Head Indentation**



**Figure 38. Comparison between Static and Dynamic FEA for Shell Indentation**

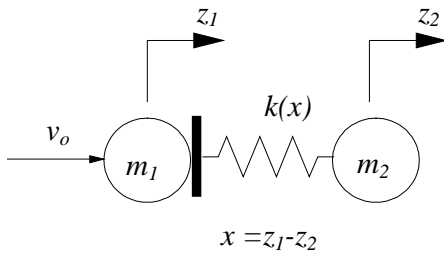


**Figure 39. Dynamic Lumped-Mass Model for Tank Car Impacts**

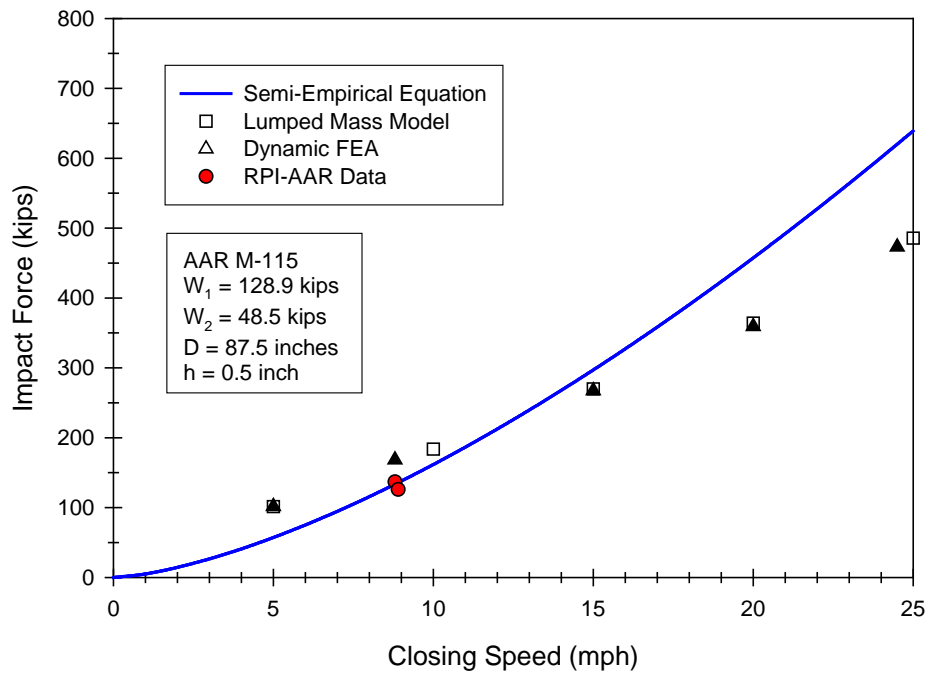


**Figure 40. Impact Force as a Function of Closing Speed for Head Impacts**

### 3.2 Validation

With appropriate choices in element type (shell vs. solid), element aspect ratio, and order of quadrature, results from the dynamic, nonlinear FEA models are compared to impact forces and indentations measured in tests. For head impacts, results from the FEA models are compared to data from tests conducted by the RPI-AAR Tank Car Safety Research and Test Project during the 1970s [19]. For shell impacts, FEA results are compared to data from tests conducted as part of the Next Generation Rail Tank Car project [20].

### 3.2.1 Head Impacts

Dynamic nonlinear (i.e., elastic-plastic material behavior with large deformations) finite element analysis was conducted using LS-DYNA3D (version 970) to simulate three impact speeds: 6, 8.8, and 11.5 mph. The analysis modeled a rigid coupler impacting an elastic-plastic ellipsoidal tank car head (i.e. end cap). The finite element mesh of the end cap comprised two layers of 8-noded hexahedron elements through the thickness of the tank car head with a nominal element aspect ratio of 8 to 1. Moreover, the explicit finite element solver with reduced integration to formulate the element stiffness was used in the finite element analysis. To minimize computational time, the tank container was modeled by a large area of rigid material and a smaller area of deformable material at impacted end of the tank (Figure 41). The impacting coupler was modeled as a rigid part with its density adjusted to reflect the weight of the entire ram car. All simulations were terminated after 0.25 seconds. Table 6 lists the relevant details of the RPI-AAR tank car head impact tests that were simulated by the FEA.

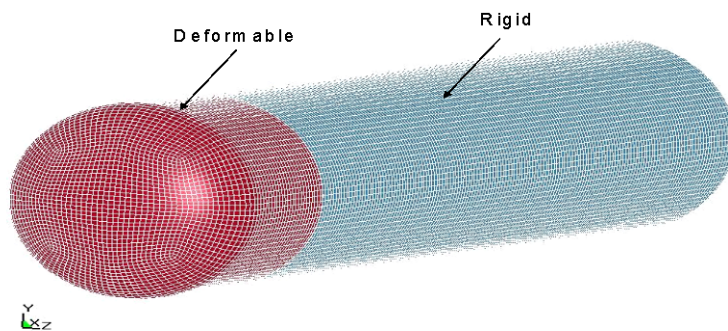


**Figure 41. Rigid-Deformable Finite Element Model of Tank Container**

**Table 6. Details of Simulated Tank Car Head Impact Tests**

<i>Parameter</i>	<i>Value</i>
Impact location	1/3 down from center
Ram car weight	128,706 lb
Tank car weight	45,325 lb
Diameter	87.5 inches
Aspect ratio of ellipsoidal cap	2 to 1
Head thickness	0.5 inch
Outage	100%

The end caps in the tank car impact tests were made from AAR M-115 steel. Table 7 lists material properties assumed in the FEA for this tank car steel. Additional assumptions regarding material behavior were listed previously in Table 2.

**Table 7. Material Properties Assumed for Tank Car Head**

<i>Property</i>	<i>Value</i>
Density, $\rho$	0.283 lb/in <sup>3</sup>
Poisson's ratio, $\nu$	0.3

The RPI-AAR tank car head impact test data include measurements for residual dent depth, residual dent width, and maximum coupler force. Table 8 compares the results from the dynamic, nonlinear FEA with the test data for the three different impact speeds. The calculated residual dent depths are within 20 percent of the measurements. Although the FEA consistently underestimates the residual dent widths, the calculated widths are within 25 percent of the measurements. The FEA underestimates the maximum coupler forces at impact speeds of 8.8 and 11.5 mph, but the calculated impact forces are within 10 percent of the measurements. At 6 mph, however, the calculated maximum coupler force overestimates the test result by more than 80 percent.

**Table 8. Comparison between FEA and RPI-AAR Head Impact Tests with 100 Percent Outage**

(a) Residual Dent Depth (inches)

Impact Speed (mph)	Test	FEA	% diff
6.0	6.5	6.7	+3%
8.8	13.5	11.0	-19%
11.5	16.0	15.0	-6%

(b) Residual Dent Width (inches)

Impact Speed (mph)	Test	FEA	% diff
6.0	53	43	-19%
8.8	62	54	-13%
11.5	80	60	-25%

(c) Maximum Coupler Impact Force (kips)

Impact Speed (mph)	Test	FEA	% diff
6.0	59	108	+83%
8.8	137	151	+10%
11.5	208	192	-8%

The most conspicuous results are those at the impact speed of 6 mph. Numerical experiments are conducted to examine the effect of various modeling assumptions on the calculations at this impact speed. The variations in modeling assumptions include: element type, integration scheme (i.e., reduced versus fully integrated elements), and mesh density. Mesh density is related to the assumed element aspect ratio. In the case of shell elements, the number of integration points through the thickness is a modeling variable. In the case of solid elements, the number of layers through the thickness is related to the element aspect ratio.

Table 9 lists the various cases exercised in the numerical experiments for an impact speed of 6 mph. The table also shows the relative effect of the modeling assumptions on the calculated residual dent depths and maximum coupler forces. Considering only the cases with shell elements, the calculated maximum coupler forces vary by less than 9 percent while the calculated dent depths vary by less than 4 percent. Much larger variations in the calculated results are evident when solid elements are used. The calculated results using solid elements are not sensitive to mesh density with reduced integration. Conversely, the calculated results using solid elements are sensitive to mesh density when fully integrated elements are used. Table 10 lists the cases and results for an impact speed of 11.5 mph.

**Table 9. Effect of Modeling Assumptions on Results at Impact Speed of 6 mph**

Element Type	Integration Scheme	Element Aspect Ratio	Through Thickness Attribute	Residual Dent Depth (inches)	Residual Dent Width (inches)	Maximum Coupler Force (kips)	Max. Eff. Plastic Strain
Shell	Reduced	4:1	2 points	6.4	41	108	0.04
			4 points	6.5	41	107	0.06
			8 points	6.5	40	107	0.07
		1:1	2 points	6.3	40	110	0.10
			5 points	6.4	40	108	0.15
	Full	4:1	2 points	6.3	41	113	0.04
			4 points	6.4	40	110	0.05
			8 points	6.4	41	110	0.06
		1:1	2 points	6.3	41	112	0.10
		5 points	6.6	42	108	0.14	
Solid	Reduced	8:1	2 layers	6.6	45	108	0.04
		2:1	2 layers	6.7	42	107	0.11
	Full	8:1	2 layers	4.7	39	135	0.07
		2:1	2 layers	6.1	40	112	0.10

**Table 10. Effect of Modeling Assumptions on Results at Impact Speed of 11.5 mph**

Element Type	Integration Scheme	Element Aspect Ratio	Through Thickness Attribute	Residual Dent Depth (inches)	Residual Dent Width (inches)	Maximum Coupler Force (kips)	Max. Eff. Plastic Strain
Shell	Reduced	4:1	2 points	15.1	58	170	-
			5 points	15.3	59	174	-
		1:1	2 points	14.7	55	173	-
			5 points	15.0	59	168	-
	Full	4:1	2 points	14.4	62	200	0.07
			5 points	14.8	62	195	0.08
		1:1	2 points	14.2	60	199	0.17
			5 points	14.3	58	194	0.20
Solid	Reduced	8:1	2 layers	15.0	60	192	0.07
		2:1	2 layers	15.0	57	193	0.18
	Full	8:1	2 layers	11.6	54	241	0.08
		2:1	2 layers	14.3	56	200	0.13

Fluid-structure interaction is included in the finite element modeling to account for the inertial effects of fluid in the tank. The finite element analysis with fluid-structure interaction uses Arbitrary-Lagrangian-Eulerian (ALE) coupling.<sup>4</sup> The finite element model with fluid-structure interaction consists of four parts: (1) the tank car structure (Lagrangian mesh), (2) an air block surrounding the tank car structure (Eulerian mesh), (3) the liquid inside the tank (Eulerian mesh), and (4) vapor outage that fills the remainder of the tank (Eulerian mesh). The physical properties of the fluid inside the tank are adjusted according to the lightweight and test weight recorded for a given impact test.

Table 11 compares the results from the dynamic, nonlinear FEA with fluid-structure interaction to the test data for three different impact speeds. In these impact tests, the coupler struck the tank car head at the center of the end cap. The impact force measured at 10.2 mph is less than the impact force measured at 8.7 mph. In each case, the calculations for impact forces and residual dent dimensions (depth and width) over-predict the measurements.

<sup>4</sup> In the present context, a Lagrangian mesh is one that transforms according to its deformation; an Eulerian mesh is a fixed mesh in space through which material flows.

**Table 11. Comparison between FEA and RPI-AAR Head Impact Tests with 2% Outage**

(a) Residual Dent Depth (inches)

Impact Speed (mph)	Test	FEA	% diff
7.2	6.5	12.5	+92%
8.7	8.25	12.7	+54%
10.2	11.25	15.9	+41%

(b) Residual Depth Width (inches)

Impact Speed (mph)	Test	FEA	% diff
7.2	40	54.4	+36%
8.7	48	57.5	+20%
10.2	60	63.9	+7%

(c) Maximum Coupler Force (kips)

Impact Speed (mph)	Test	FEA	% diff
7.2	89	174	+96%
8.7	200.8	300	+49%
10.2	141	372	+164%

Figures 42 through 44 compare the calculated and measured impact forces and indentation dimensions (depth and width) for the various cases involving bare tank heads with different levels of outage. The calculated values for the case of 2 percent outage are clearly stiffer than the observed behavior, and required further refinement. The horizontal error bars in these figures indicate the range of calculated impact forces and indentation dimensions depending on the modeling assumptions for mesh density, element type, and integration scheme. The dynamic nonlinear finite element calculations for indentations and maximum coupler forces in empty tanks were within 25 percent of the RPI-AAR impact test data with the exception of the maximum coupler force at relatively low impact speed.

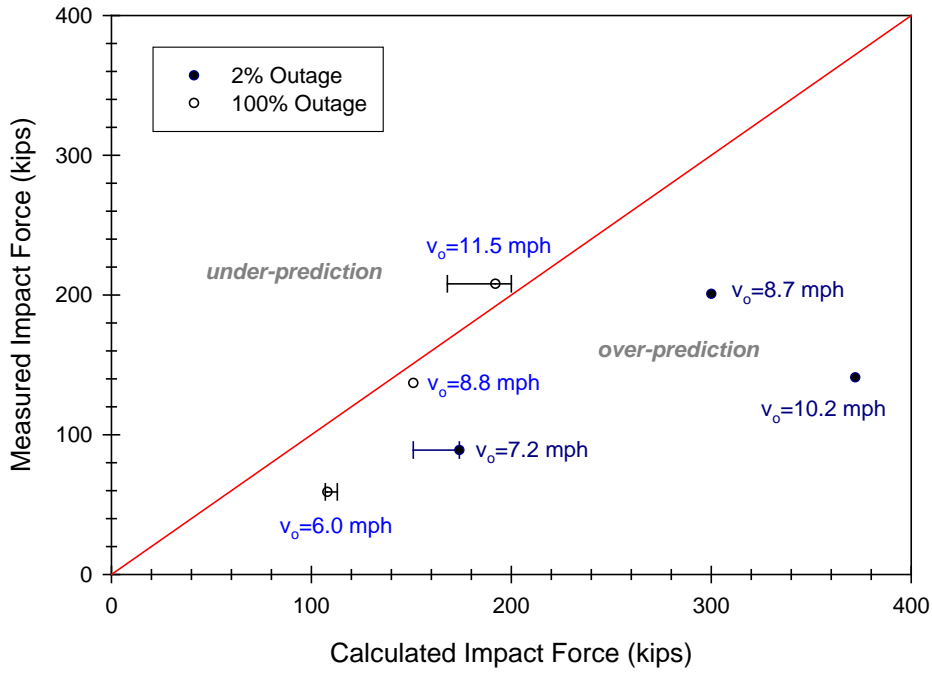


Figure 42. Comparison between Calculated and Measured Impact Forces

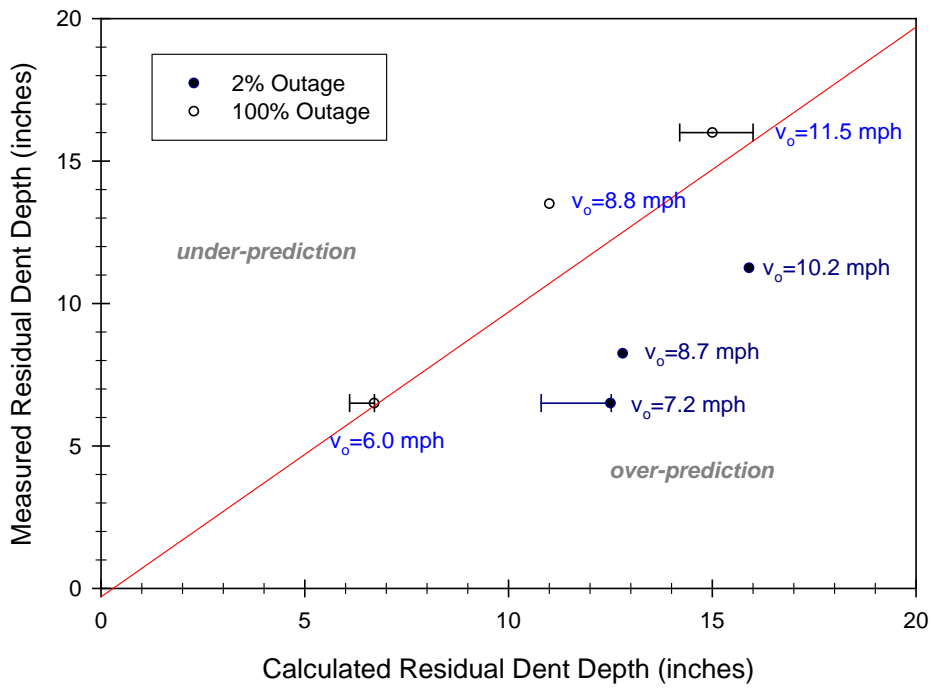
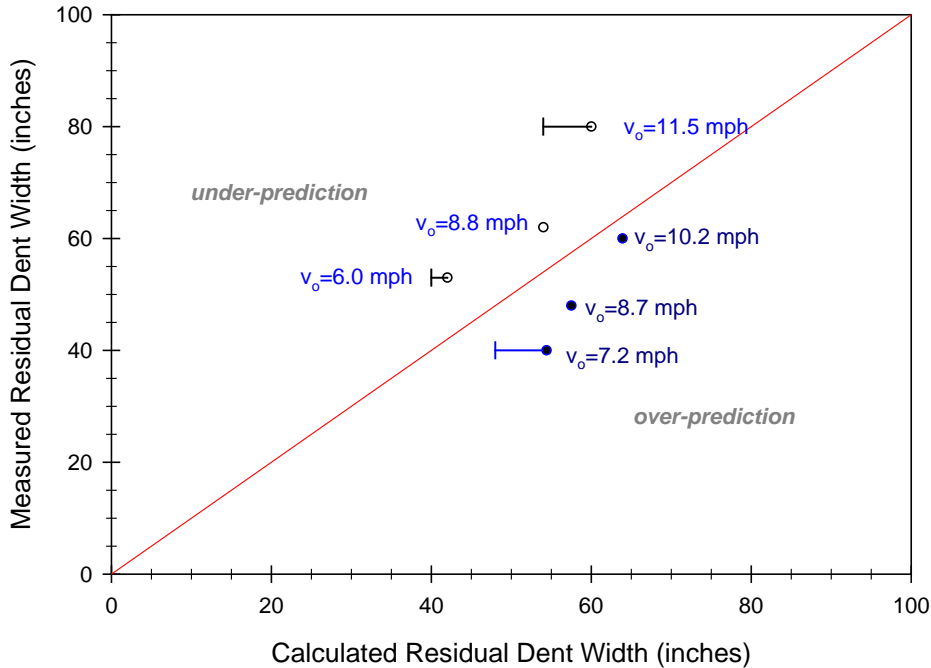


Figure 43. Comparison between Calculated and Measured Residual Dent Depths



**Figure 44. Comparison between Calculated and Measured Residual Dent Widths**

Finite element analyses were performed with different combinations of element types (solid and shell elements), integration schemes (reduced and fully integrated), and through-the-thickness characteristics (element aspect ratio or mesh density). Based upon these variations, the following results were observed:

- (1) Different analyses calculated similar indentations and coupler forces with the exception of the analysis with a relatively coarse mesh and fully integrated solid elements, which calculated stiffer behavior compared to the other analyses.
- (2) Maximum strains are consistent and reasonable for the analyses with finer meshes at low impact speed.
- (3) At higher impact speeds, maximum strains are consistent with the exception of the analyses with reduced integrated shell elements.

### 3.2.2 Shell Impacts

As part of the Next Generation Rail Tank Car Project, a series of full-scale tests were conducted to examine the structural behavior of chlorine tank cars under shell impacts. In these tests, a stationary tank car was positioned next to a concrete wall, as shown in Figure 45. The tank car contained water mixed with clay slurry to produce the density approximately equal to that of liquid chlorine. The outage in the tests was 10.6 percent with an internal pressure of 100 psi. A ram car weighing 286,000 lb with a rigid indenter was used to strike the side of the tank car at its center on the beltline. Moreover, these tests were conducted to provide data for validating the FEA models developed for shell impacts.



**Figure 45. Position of Tank Car in Full-Scale Tests**

Table 12 summarizes the three full-scale shell impact tests in terms of impact speeds and outcomes. The first test, called the Assurance Test (also referred to as Test 0), was conducted to understand the test environment and the gross motions of the cars during the impact test. Moreover, the cars in Test 0 were equipped with limited instrumentation. The cars in subsequent tests were heavily instrumented to provide redundant measurements for forces and displacements. In addition, different indenter sizes were used in the tests, which are denoted in the table. The indenter shape was a rectangular cross-section with rounded edges. The dimensions for each indenter face are listed in Table 13.

**Table 12. Summary of Full-Scale Shell Impact Tests**

	Impact Speed (mph)	Indenter Type	Outcome
Test 0	10	Large	Tank integrity maintained
Test 1	14	Large	Tank integrity maintained
Test 2	15	Small	Tank punctured

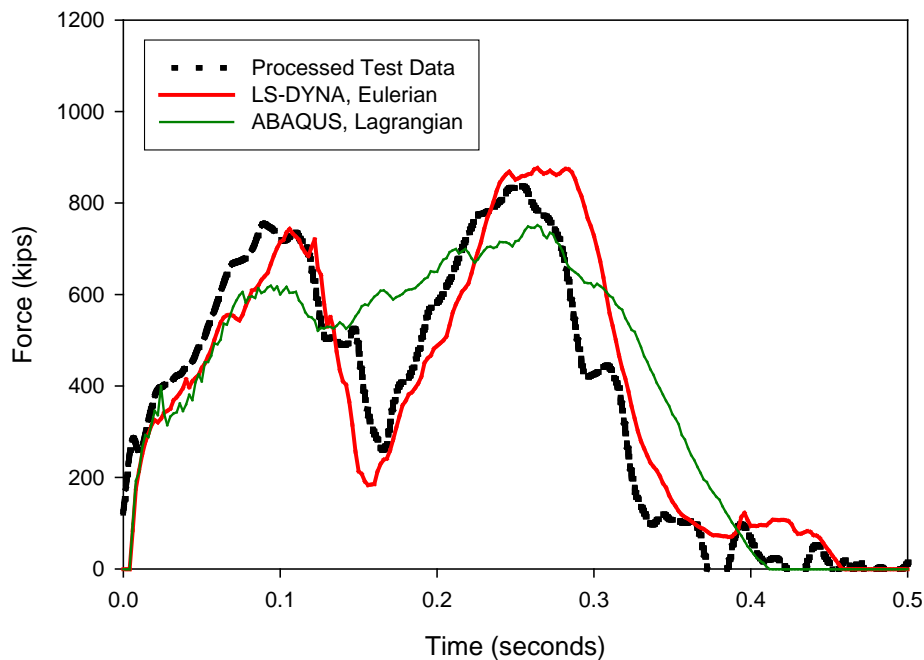
**Table 13. Indenter Face Dimensions**

Indenter Type	Height (inches)	Width (inches)	Edge Radii (inch)
Large	17	23	1
Small	6	6	½

Different mesh representations are used in the FEA models to account for fluid-structure interaction. Specifically, Lagrangian and Eulerian mesh formulations are used. In a Lagrangian mesh, the nodes follow the material as it deforms. An Eulerian mesh is fixed in space, and tracks the material passing through. A Lagrangian mesh is used to model the tank structure. Both Lagrangian and Eulerian mesh formulations are used to model the fluid.

The FEA models to simulate the full-scale tests do not include tank car components such as the manway, body bolsters, and draft sills. In addition, the presence of the outer steel jacket and thermal protection is ignored.

In all of the tests, the ram car was instrumented with accelerometers. The accelerometer data were filtered, and processed to provide forces. Figure 46 compares the force-time history as measured in Test 0 with those calculated from the FEA models using different fluid representations to account for fluid-structure interaction. The results suggest that the Eulerian fluid formulation provides more accurate results in terms of capturing the overall character of the force-time history. Moreover, these results suggest that the movement or sloshing of the fluid during the impact event plays a significant role in the force-time behavior.



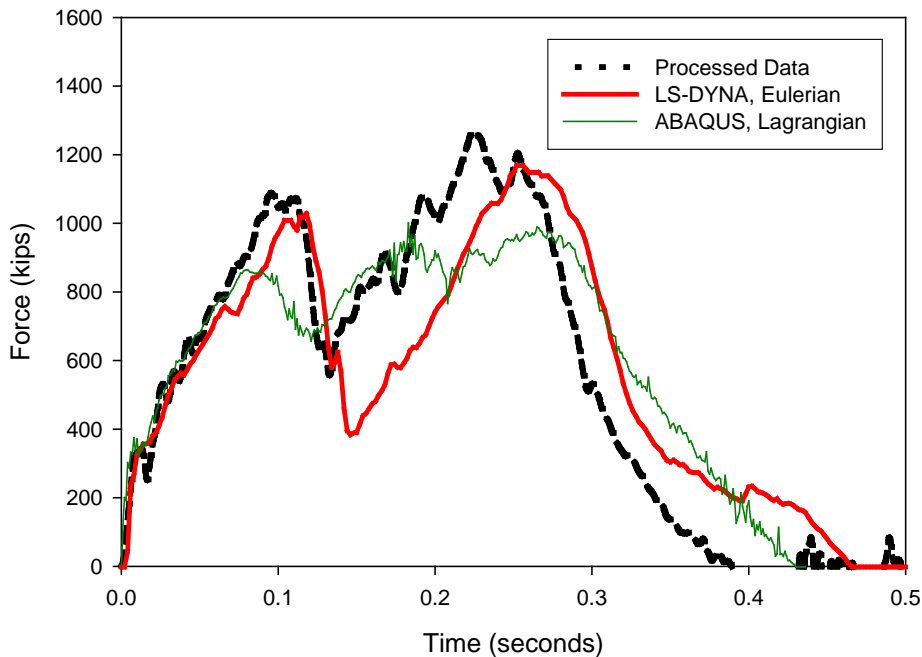
**Figure 46. Comparison of Force-Time Histories for Test 0**

Table 14 compares the maximum impact force measured in Test 0 with FEA results with different fluid formulations. The maximum impact force calculated using LS-DYNA with the Eulerian fluid formulation is within 5 percent of the test data, which is excellent agreement.

**Table 14. Comparison of Maximum Forces in Assurance Test**

	Maximum Force (kips)
Assurance Test	837
LS-DYNA, Eulerian	877
ABAQUS, Lagrangian	707

Figure 47 compares the force-time histories from the data in Test 1 and the FEA results with different fluid formulations. The FEA results with the Eulerian fluid formulation again show excellent agreement with the data in Test 1.



**Figure 47. Comparison of Force-Time Histories for Test 1**

Table 15 compares the maximum impact forces and maximum indentations from Test 1 and the FEA results using LS-DYNA and the Eulerian fluid formulation. The maximum impact forces are within 10 percent. The maximum indentation of 26 in was measured in the test with string potentiometers. The FEA prediction of 30 in for maximum indentation assumed mechanical properties based on minimum requirements for TC-128B tank car steel. After Test 1 was conducted, tensile tests were performed to determine the actual mechanical properties, which were roughly 10 percent greater than the minimum requirements for both yield and ultimate tensile strengths. The FEA calculations were performed with the actual properties, which resulted in slightly better agreement for both maximum impact force and maximum indentation.

**Table 15. Comparison between Test 1 and FEA**

	Maximum Force (kips)	Maximum Indentation (inches)
Test 1	1290	26
LS-DYNA, Eulerian <sup>(1)</sup>	1223	29
LS-DYNA, Eulerian <sup>(2)</sup>	1170	30

NOTES:

<sup>(1)</sup> Based on measured material properties from Test 1 tank car

<sup>(2)</sup> Based on assumed properties based on minimum requirements

Figure 48 compares force-indentation curves from Test 1 data and the FEA results. The curve representing the test data is a cross-plot of indentation-time history obtained from string potentiometers and force-time history from processed accelerometer data. The force-indentation curve from the FEA shows qualitative agreement with the test.

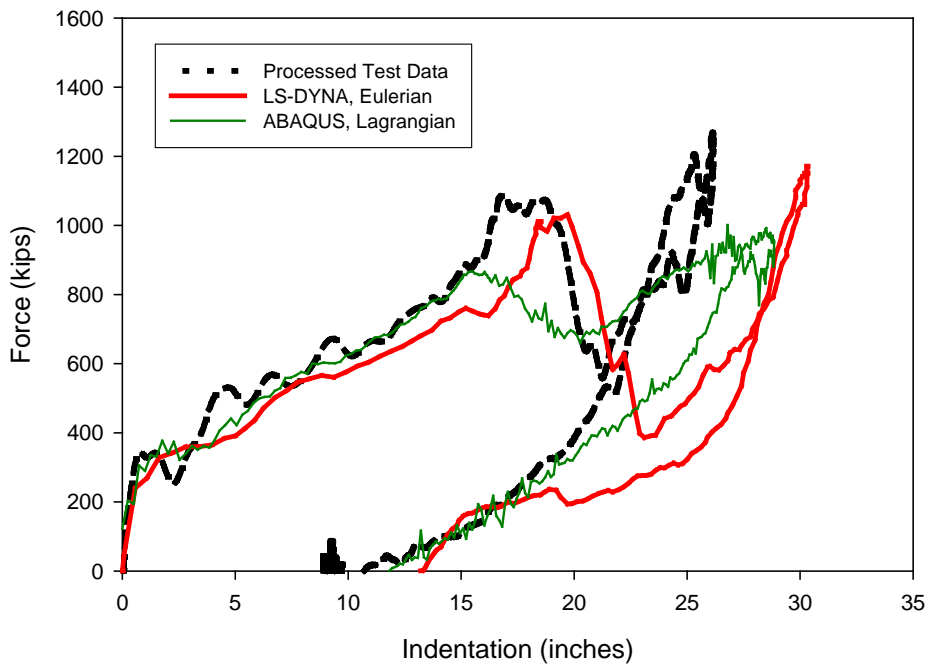


**Figure 48. Comparison of Force-Indentation Curves for Test 1**

The second full-scale shell impact test used an impactor with a smaller cross-sectional area than the previous tests to increase the likelihood of rupturing the tank. Moreover, the ram car in this test struck the side of the stationary tank car at impact speed of 15 mph, and punctured the tank.

Analyses of Test 0 and Test 1 demonstrated that the FEA with the Eulerian fluid formulation provides results that are in close agreement with the test data. However, the present capabilities of the software are such that material failure was incorporated into the FEA with the Lagrangian fluid formulation only. Moreover, material failure is assumed to initiate when the effective strain reaches a certain value for a given state of stress in terms of stress triaxiality [25]. Material failure criteria are discussed in greater detail in the following section of this report.

The accelerometer measurements in Shell Impact Test 2 were filtered and processed in the same manner as the previous tests. Figure 49 compares the force-time histories from Test 2 with finite element analyses with and without applying the failure criterion. The figure shows that the processed force data quickly drops off at about 90 milliseconds (ms), indicating the time at which failure of the tank initiated and eventually led to puncture. The data also indicates that the impact force at the time of failure was 910 kips. The force-time history curves from the FEA with and without the failure criterion are nearly identical up to 90 ms. The force drop-off calculated by the FEA with the failure criterion occurs slightly earlier than the test. In addition, the maximum force calculated by the FEA with the failure criterion is lower than the peak impact force measured in Test 2. These differences are attributed to the new skid design for Test 2 in which the tank car is positioned next to the wall. That is, the skid design may provide more structural stiffening to the tank than the previous outrigger design used in the previous tests. The overall character of the calculated force-time history resembles the test data reasonably well. FEA of Test 2 assumed material properties measured from the tank car used in Test 1, which are roughly about 10 percent greater than the minimum requirements for both yield strength and ultimate tensile strength.

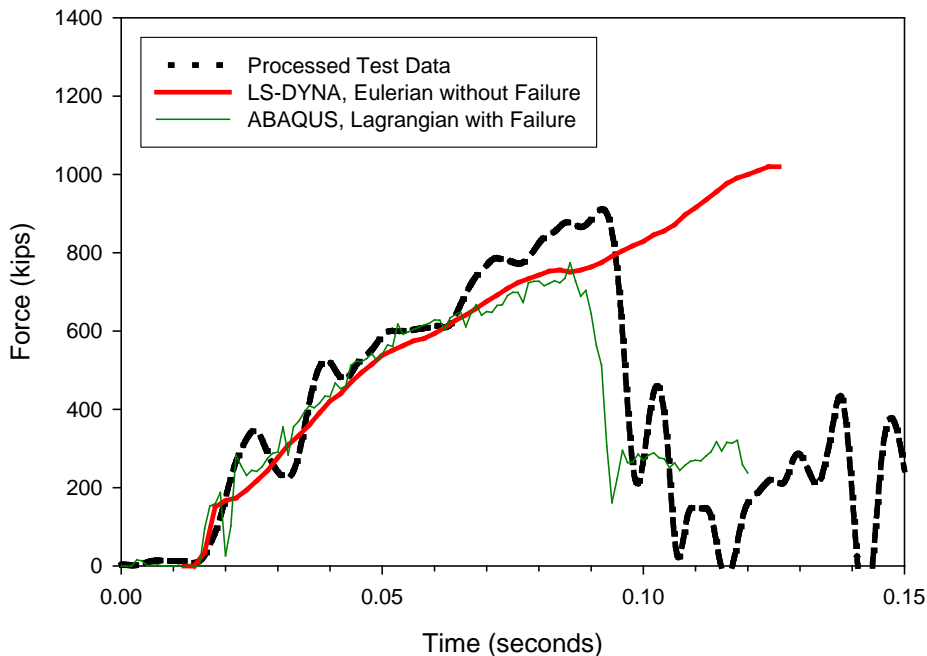


**Figure 49. Comparison of Force-Time Histories for Test 2**

### 3.2.3 Unnotched Charpy Tests

The pendulum impact tests, which are described in the section on Tank Car Steels Characterization, provided data that can be used to examine the effect of different material failure criteria on fracture energy. Elastic-plastic finite element analysis (FEA), assuming different criteria, was conducted to calculate the fracture energy and simulate the Bulk Fracture Charpy Machine (BFCM) tests [26]. Three material failure criteria are described briefly as follows.

- 1) *Gurson-Tvergaard*—This criterion was developed by Gurson [27] and Tvergaard [28] and [29] specifically for failure by ductile fracture. FEA applying this criterion to examine the puncture resistance of tank cars was proposed by Anderson and Kirkpatrick [30], and performed by Anderson et al. [31].
- 2) *Constant strain*—This criterion is the simplest to implement in FEA, and assumes that failure initiates when the effective strain reaches a critical level (e.g., 20 percent).
- 3) *Bao-Wierzbicki*—Effective strain to initiate failure depends on the general state of stress in terms of stress triaxiality [25].

Stress triaxiality is the portion of the stress tensor that is hydrostatic. Mathematically, it is the ratio of mean stress to von Mises equivalent stress, or

$$\eta = \frac{\sigma_m}{\sigma_e} \quad (2)$$

In terms of principle stresses, the mean stress and the effective or von Mises equivalent stress are defined as

$$\sigma_m = \frac{1}{3}(\sigma_1 + \sigma_2 + \sigma_3) \quad (3)$$

$$\sigma_e = \sqrt{\frac{1}{2}[(\sigma_1 - \sigma_2)^2 + (\sigma_2 - \sigma_3)^2 + (\sigma_3 - \sigma_1)^2]} \quad (4)$$

Mean or hydrostatic stress is associated with dilatation or the change in volume of a material element as it deforms. Effective or von Mises stress is directly related to distortional energy or the energy to change the shape of a material element as it deforms. Therefore, a physical interpretation of stress triaxiality is that it describes the general state of stress in a material element and is the ratio of volume change to shape change.

Figure 50 shows a schematic of effective strain to initiate failure as a function of stress triaxiality. The failure initiation envelope for the Bao-Wierzbicki (B-W) criterion is shown to consist of three regions representing different modes of failure. Region I is characterized by high values of stress triaxiality which promote the nucleation, growth, and coalescence of voids leading to ductile fracture. Region III is associated with negative stress triaxiality which represents shear fracture due to shear band localization. Region II comprises positive but low values of stress triaxiality representing mixed mode

fracture. The schematic also shows that zero stress triaxiality (i.e.,  $\eta$  equal to 0) is equal to a stress state of pure shear, and that the cusp between Regions I and II (which corresponds to  $\eta$  equal to  $1/3$ ) is equal to a stress state of uniaxial tension. In theory, the failure initiation envelope for a given material is developed through a series of physical tests. The complete series entails 11 tests with different specimen geometries to characterize different levels of near-constant stress triaxiality in the vicinity of failure. Such tests were conducted previously to develop failure initiation envelopes for 2024-T351 aluminum [32] and A710 steel [33]. In the FEA implementation, the failure initiation envelope is developed from a calibration method using measurements from standard uniaxial tensile tests [34]. The constant strain criterion is also shown in the schematic for comparison. Clearly, constant strain may be considered as a special case of the B-W failure envelope in which effective strain to initiate failure is independent of stress triaxiality. In addition, the Gurson-Tvergaard criterion may be considered as accounting for only Region I of the B-W failure envelope.

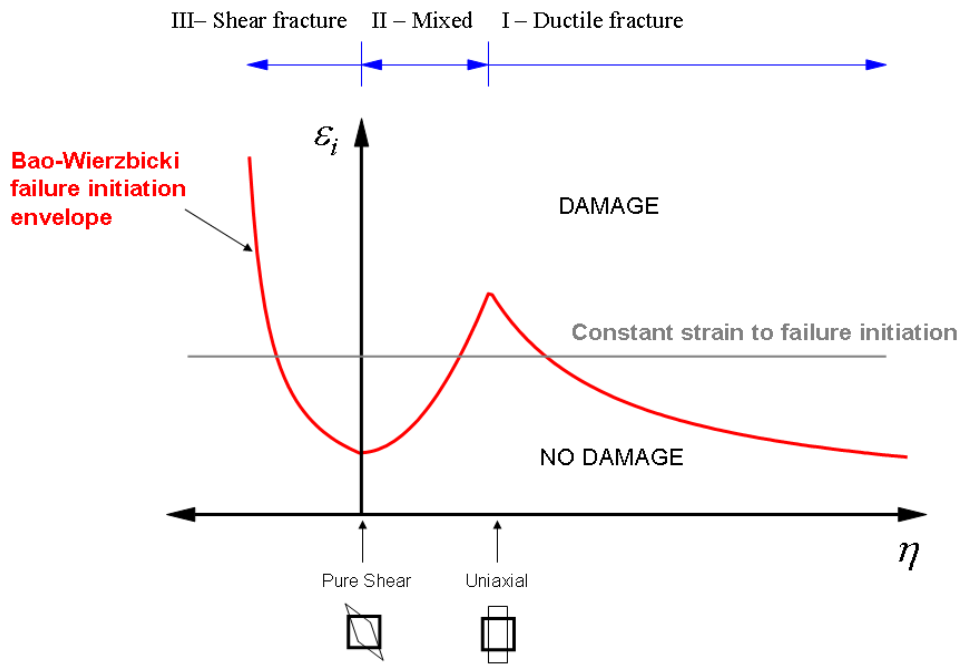


**Figure 50. Schematic of Failure Initiation Envelope based on Stress Triaxiality**

Failure initiation occurs when loading conditions induce effective plastic strains at levels above the limits suggested by Figure 50. Once failure initiates, damage is assumed to progress in the form of linear strain softening. Figure 51 illustrates this concept, in which the stress-strain behavior of a material element exhibits a linear decrease in stress with increasing strain beyond the strain to initiate failure,  $\epsilon_i$ . Modeling damage progression by strain softening helps minimize the mesh dependency of the numerical results [35].

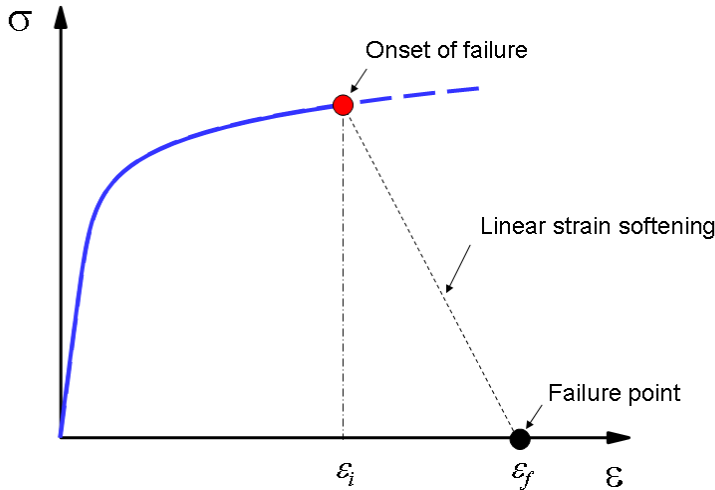
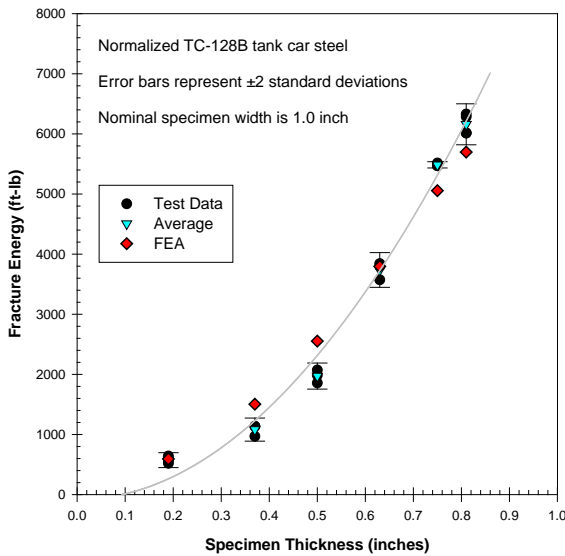
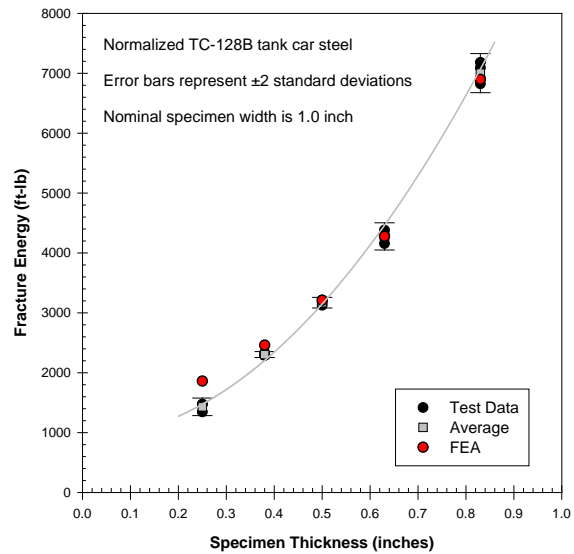


**Figure 51. Schematic of Linear Strain Softening**

Figure 52 compares BFCM test data for normalized TC-128B tank car steel using the two different strikers with FEA results based on the B-W criterion. The solid curve in the figure represents the result of a best-fit regression analysis through the BFCM data. Error bars on the data are two standard deviations above and below the mean value for a given specimen thickness. The close agreement between the test data and analysis is self-evident especially for the thicker specimens.



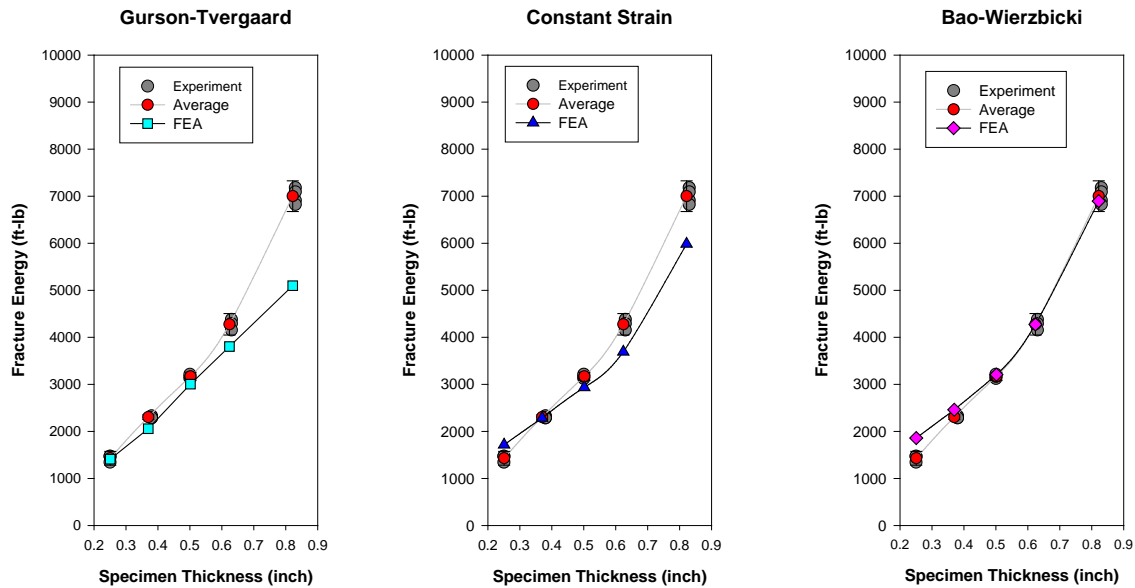
(a) Sharp Tup



(b) Blunt Tup

**Figure 52. Comparison of BFCM data for Normalized TC-128B with FEA assuming Bao-Wierzbicki Criterion**

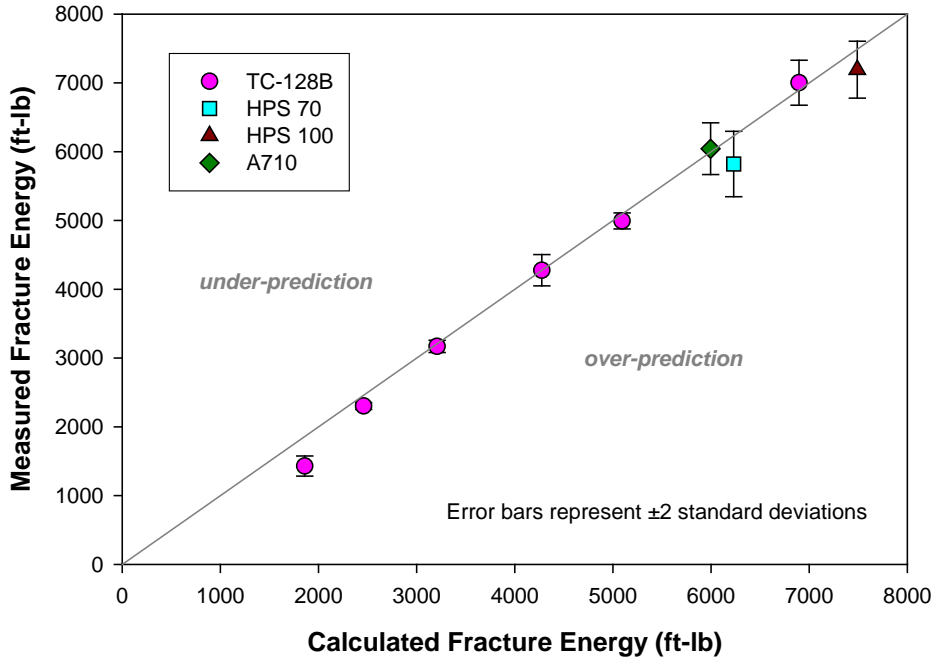
Figure 53 compares the BFCM test data (using a blunt striker) with FEA results assuming three different criteria. FEA results using the Gurson-Tvergaard (G-T) criterion were reported by Anderson et al. [31]. FEA results using constant strain and the Bao-Wierzbicki (B-W) criteria were reported by Yu et al. [26]. In applying the constant strain criterion, a critical value of 20 percent strain was assumed. Fracture energies calculated using the G-T criterion appear to vary linearly with specimen thickness. Assuming constant strain, the variation is nonlinear. The variation is also nonlinear in the case of the B-W criterion. In addition, the calculated fracture energies for the thinner specimens are not as accurate as those for the thicker specimens in the case of the B-W criterion. Mesh refinement may improve the calculated energies for the thinner specimens. However, the thicknesses of commodity tanks are usually greater than 0.5 inch. Moreover, for thicknesses of interest in tank car designs, fracture energies calculated using the B-W criterion are within excellent agreement of the measured fracture energies.



Error bars for experimental data represent  $\pm 2$  standard deviations

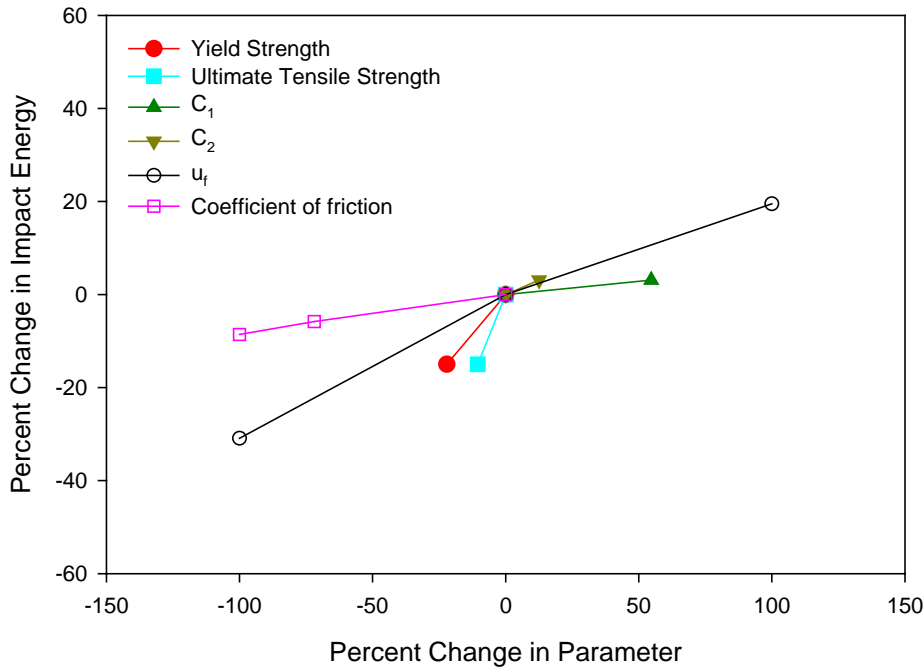
**Figure 53. Comparison of Different Failure Criteria with BFCM Test Data for TC-128B Tank Car Steel**

Figure 54 compares measured BFCM fracture energies (using the blunt striker) with those calculated using elastic-plastic FEA with the B-W criterion for different tank car steels. The mechanical properties for these materials are listed in Table 2. The figure shows excellent agreement between the experimental and calculated values for fracture energy. The close agreement provides confidence in applying the B-W criterion to examine material failure. Moreover, the application of the B-W criterion to the BFCM tests provides a benchmark to calculate puncture in the full-scale for application, which was accomplished and described previously.



**Figure 54. Comparison of Measured and Calculated Fracture Energies for Different Steels (Blunt Striker)**

Sensitivity studies were performed with the FEA model to simulate the BFCM test to examine the relative effect of different factors on calculated impact energy. The factors examined in the studies can be grouped into four categories: (1) plasticity (yield and ultimate tensile strengths), (2) fracture initiation ( $C_1$  and  $C_2$ ), (3) softening (failure displacement,  $u_f$ ), and (4) contact (coefficient of friction). In the sensitivity studies, each factor was varied from its baseline value, one at a time, while the other factors remained equal to the baseline values. Figure 55 summarizes the results of the sensitivity studies. The figure shows that varying the failure displacement by  $\pm 100$  percent changes the impact energy from about  $-30$  percent to about  $+20$  percent. Moreover, the slopes of the lines for each factor indicate their relative effect on the calculated impact energy. Thus, the plasticity parameters have the most significant effect on the calculated impact energy. The failure initiation parameters and the failure displacement have moderate effects. The coefficient of friction has a less significant effect.



**Figure 55. Percent Variation in Impact Energy with Parameter Changes**

### 3.3 Discussion and Summary

Finite element analysis (FEA) models are developed to estimate the response of the tank structure to collision events, such as the impact of a coupler from an adjacent rail car on the end cap (i.e., head) or side (i.e., shell) of a tank car. The structural response is calculated in terms of impact force as a function of indentation, or force-indentation characteristic.

Results from static FEA models are compared to closed-form solutions for ellipsoidal heads and cylindrical tubes. The closed-form or analytical solutions assume rigid-plastic material behavior, whereas the FEA models assume elastic-plastic material. The closed-form solutions also assume a concentrated load, whereas the FEA models assume that the load is applied through a rigid punch. Despite these differences, the force-indentation characteristics calculated by the FEA models and the closed-form solutions are in reasonable agreement for both head and shell deformations.

Static and dynamic, nonlinear FEA models produce nearly identical force-indentation characteristics for both head and shell impacts. Dynamic, nonlinear FEA models for head impact are also compared with lumped-parameter models, which give similar results in terms of impact force as a function of closing speed.

The comparisons between FEA models and closed-form solutions are valid for empty tanks. Similar comparisons for tanks containing lading cannot be made because no closed-form solutions are available. When the tank contains lading, the fluid and the tank structure both move and exert forces upon one another during the impact event. Different mesh representations are used in the FEA models to account for fluid-structure interaction. Development of computational models that include the multi-physics of fluid-structure interaction is a topic on the forefront of current research and development [36].

Results from dynamic nonlinear FEA with different fluid formulations are compared to data from full-scale tank car shell impact tests, which are shown to be in excellent agreement. Figure 56 overlays the measured and calculated force-indentation curves for the two full-scale shell impact tests (i.e., Tests 1 and 2). The figure also shows a regression curve that was generated from the calculated and measured curves for both tests. Moreover, the figure suggests indenter size has a relatively weak effect on force-deformation behavior for indentations less than 20 in, but indenter size appears to have a relatively strong effect on tank car puncture. Additional analyses confirm this conclusion [37].

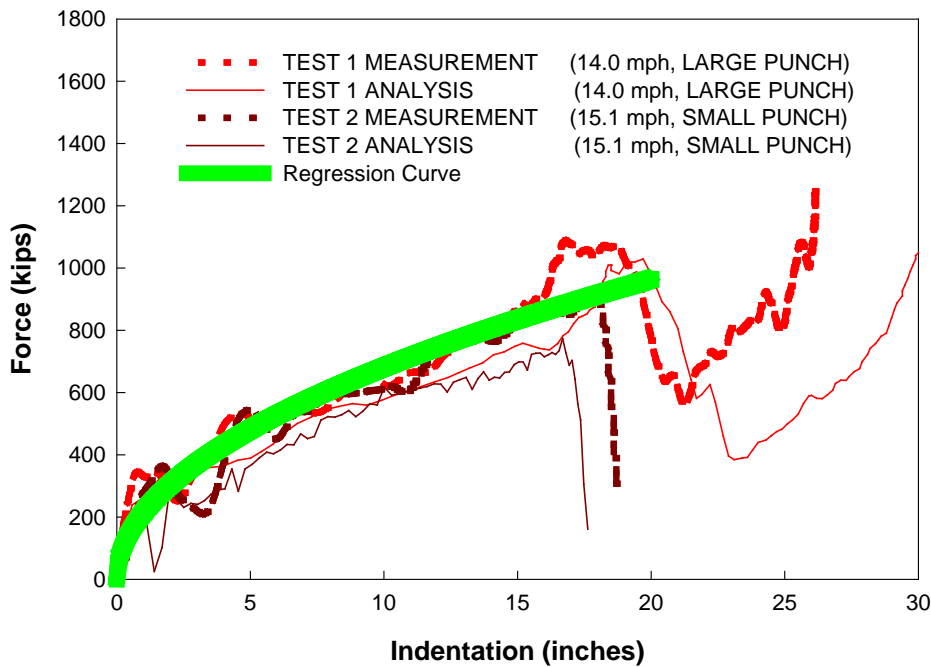


**Figure 56. Force-Indentation Characteristic for Shell Impact**

Material failure was predicted using a strain-based criterion, referred to as the Bao-Wierzbicki (B-W) criterion. In this criterion, the effective plastic strain to initiate failure depends on the general state of stress in the tank structure in terms of stress triaxiality. Implementation of the B-W criterion was validated using data from pendulum impact

tests conducted on unnotched Charpy specimens made from tank car steel. Results from the FEA simulations were shown to be in excellent agreement with the experimental measurements of fracture energy over a range of test specimen thicknesses. Moreover, FEA produced results within the narrow scatter band of test results for all specimens of thickness greater than 0.5 inch. These results are significant because the range of specimen thickness for which the analysis most accurately reproduced the experiment corresponds to that used in typical tank car construction.

The favorable FEA results of the unnotched Charpy specimens suggested that the failure criterion can be applied to examine puncture in the full-scale shell impact tests. In modeling material failure, accurate FEA results were obtained when solid (i.e., brick) elements were used at and around the impact location. For the simulation of the pendulum impact tests, sensitivity studies suggested that these elements must have an aspect ratio equal to one with a minimum of six elements through the thickness. This is accomplished by meshing a patch of solid elements of sufficient size at the impact location. This patch can be coupled to shell elements at locations away from the impact zone that do not require this special treatment. Shell elements in the impact zone do not produce accurate results when used in conjunction with the B-W criterion.

These mesh considerations were applied in the FEA simulations of the full-scale tank car shell impact tests. Figure 57 shows this patch of solid elements in the impact zone for the tank. In this figure, the patch of brick elements in the impact area is so fine that it is depicted as a solid area.

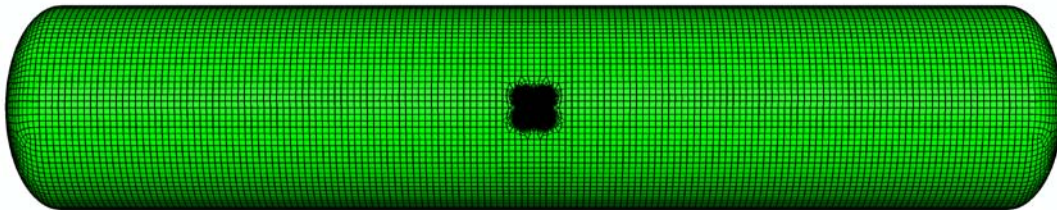
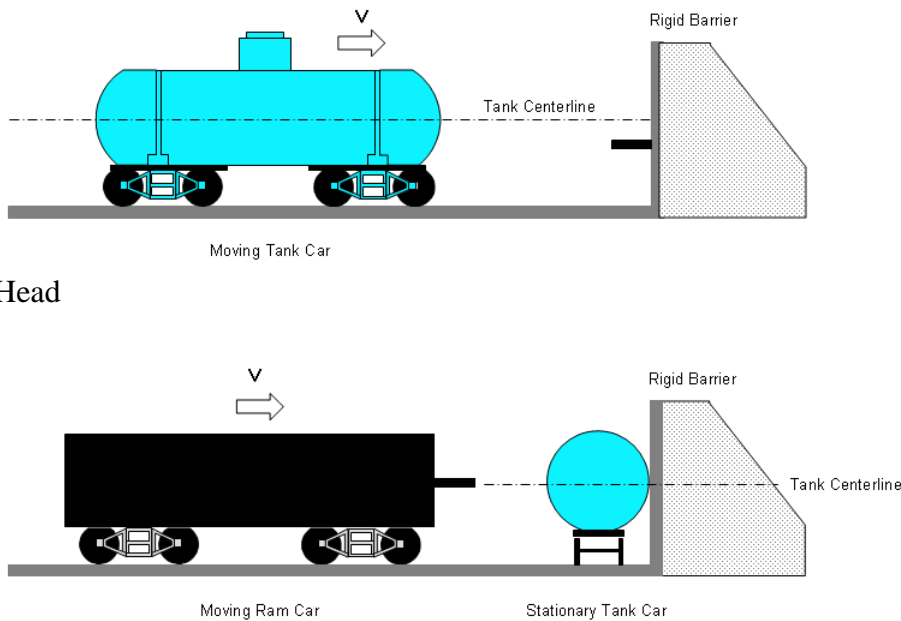


**Figure 57. Typical FEA Mesh for Full-Scale Shell Impact Simulations**

Moreover, an FEA framework for shell impacts has been developed that accounts for the following effects: (1) nonlinear material behavior using elastic-plastic constitutive models allowing for large deformations, (2) fluid-structure interaction using Lagrangian and Eulerian fluid mesh formulations while modeling the tank structure with a Lagrangian mesh, (3) material failure using a strain-based criterion that depends on the general state of stress in the tank structure.

The FEA framework was applied to examine the structural performance for a variety of tank car configurations under generalized head and shell impact scenarios. Figure 58 shows schematics of the generalized head and shell impact scenarios examined using the FEA framework. In the case of the head impact, the tank car travels into a rigid barrier with the indenter protruding from it. In the shell impact case, the tank car is stationary and is struck by a moving ram car with a rigid indenter protruding from it. The ram car weight is 286,000 lb. In addition, the figure shows that the impact location for head scenario is below the tank centerline, while the impact location for the shell scenario is coincident with the tank centerline. In both impact scenarios, the indenter face is 6 in by 6 in with edge radii of one-half inch.



(a) Head

(b) Shell

**Figure 58. Generalized Impact Scenarios Examined by FEA**

The FEA framework is applied to examine the structural performance of generic tank car configurations under the generalized head and shell impact scenarios. Table 16 lists the general attributes of these configurations. The baseline configuration is the same as the tank cars used in the full-scale shell impact tests described earlier. The second design configuration is the baseline tank with increased head and shell thicknesses. The thicker tank translates to a heavier car. In cases for the generalized head impact, the presence of a head shield is examined for both tank car configurations. In these cases, full-height, one-half-inch thick head shields are modeled. The mechanical properties assumed for the head shield material (A516-70) are listed in Table 2. In the baseline cases for both head and shell impacts and the case of the thicker baseline for the shell impact, the presence of the jacket (11-gage) is included.

**Table 16. Tank Car Configurations Examined by FEA**

	Baseline	Baseline with Increased Thickness
Nominal Tank Car Weight	263,000 lb.	286,000 lb.
Tank Inner Diameter	100 <sup>5</sup> / <sub>8</sub> inches	100 <sup>5</sup> / <sub>8</sub> inches
Outage	11%	11%
Internal pressure	100 psi	100 psi
Head thickness	0.828 inch	1.136 inches
Head material	TC-128B	A516-70
Shell thickness	0.777 inch	0.975 inch
Shell material	TC-128B	TC-128B

Structural performance is quantified in terms of puncture velocity, which is defined as the velocity at which puncture of the tank may be expected to occur, under the prescribed conditions. Table 17 lists the range of puncture velocities estimated from applying the FEA framework described in this document to the generalized head impact scenario. The table also lists the range of kinetic energies associated with the puncture velocities. The presence of a head shield and thickening the baseline tank increase the estimated puncture velocity slightly. Similarly, Table 18 lists the estimated ranges for puncture velocity and kinetic energy for the generalized shell impact scenario. The results from the FEA framework suggest a slight increase in puncture velocity from thickening the baseline tank.

**Table 17. Estimated Range of Puncture Velocity and Associated Kinetic Energy for Generalized Head Impact Scenario**

Configuration	Puncture Velocity Range (mph)	Kinetic Energy Range (Million ft-lb)
Baseline	8 – 10	0.6 – 0.9
Baseline with Head Shield	9.5 – 11.5	0.7 – 1.2
Baseline with Increased Thickness and Head Shield	10 – 12	0.9 – 1.4

**Table 18: Estimated Range of Puncture Velocity and Associated Kinetic Energy for Generalized Shell Impact Scenario**

Configuration	Puncture Velocity Range (mph)	Kinetic Energy Range (Million ft-lb)
Baseline	11 – 13	1.2 – 1.6
Baseline with Increased Thickness	12 – 14	1.4 – 1.9

## 4. TANK CAR STEELS CHARACTERIZATION

Southwest Research Institute (SwRI) carried out a laboratory testing program, under a task order contract with the Volpe Center, to examine the mechanical behavior of different tank car steels. Moreover, the testing program was conducted in response to recommendations made by the National Transportation Safety Board (NTSB) regarding the Minot derailment ([Appendix A](#)). This section briefly summarizes test results, and provides supplemental analysis and information. The SwRI testing program comprised three parts:

- 1) *Basic Material Characterization*—Basic material characterization included:
  - (a) Analysis of chemical composition;
  - (b) Testing for tensile properties, such as yield strength, ultimate tensile strength, percent elongation, and reduction in cross-sectional area; and
  - (c) Charpy V-Notch (CVN) impact testing at three temperatures: 0°F and ±50°F.
- 2) *High-Rate Fracture Toughness Testing*—Fracture toughness was measured at high strain rates, such as might be experienced in derailments, at two temperatures: 0°F and –50°F.
- 3) *Pendulum Impact Testing for Bulk Fracture Behavior*—An oversized, nonstandard pendulum impacting device was built to measure the energy to fracture unnotched Charpy specimens. The measurement of fracture energy was used to assess puncture resistance.

Specific details of the tests and results are described and presented in an extensive report prepared by SwRI [38].

A data dump from the Universal Machine Language Equipment Register (UMLER) database was performed by the AAR in April 2005 to examine the state of the pressure tank car fleet in terms of material distribution and year of manufacture. Figure 59 shows the makeup of the pre-1989 pressure tank car fleet in terms of fabrication material. The figure indicates that the vast majority of the fleet is fabricated from TC-128B. Other tank car steels makeup less than 7 percent of the fleet. Some entries in the UMLER database did not include material type, and are grouped in the “other” category.

Material for the testing program was obtained from 34 tank cars that were either retired from revenue service or were involved in an accident. For example, material was obtained from cars involved in the Minot accident that were examined by SwRI in litigation support for GATX (e.g., [39] and [40]). The tank car steels included: TC-128B (both non-normalized and normalized), A212, A515, and A285. Thirty-two of the 34 cars that were provided for this testing program were built prior to 1989. Samples were taken from both the head and shell of the tank.

Given cost and scheduling constraints, an engineering estimate of at least one car per year was sought as a sample rate. The adequacy of the sample size to draw definitive conclusions depends on the purpose of the study, population size, level of precision, level of confidence, and degree of variability. Estimates of minimum sample size for different levels of confidence and precision are given in [Appendix B](#).

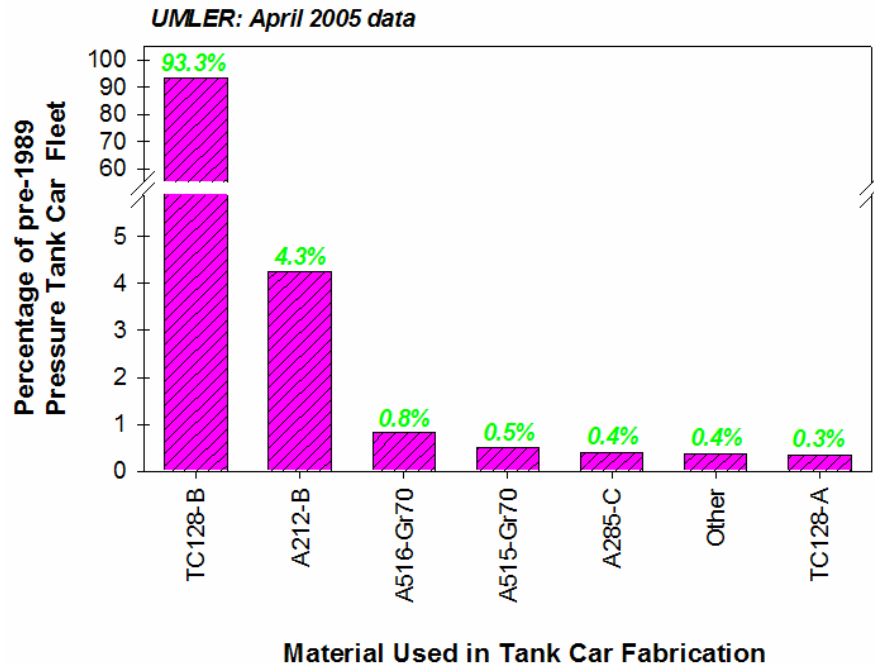


**Figure 59. Distribution of Steels in Pre-1989 Pressure Tank Car Fleet**

Figure 60 is an overlay of two plots. The bottom plot shows the cumulative percentage of pressure tank cars as a function of year of manufacture (i.e., built year) for (a) the whole fleet (represented by the green triangles) and (b) the pre-1989 fleet (blue squares). The top plot shows the makeup of the cars from which test material was obtained.

#### 4.1 Basic Material Characterization

Material characterization was conducted in accordance with the following standard test methods, which are published by the American Society for Testing and Materials (ASTM):

- 1) *Chemical analysis*—ASTM E415, “Standard Test Method for Optical Emission Vacuum Spectrometric Analysis of Carbon and Low-alloy Steel”
- 2) *Tensile properties*—ASTM A370—Standard Test Methods and Definitions for Mechanical Testing of Steel Products”
- 3) *Charpy impact energy*—ASTM E23, “Standard Test Methods for Notch Bar Impact Testing of Metallic Materials”

In the chemical analysis, 16 elements were measured and reported, even though the TC-128B composition specification calls for controlling only nine distinct elements. In summary, 59 of 61 samples (97 percent) met composition requirements for TC-128B.

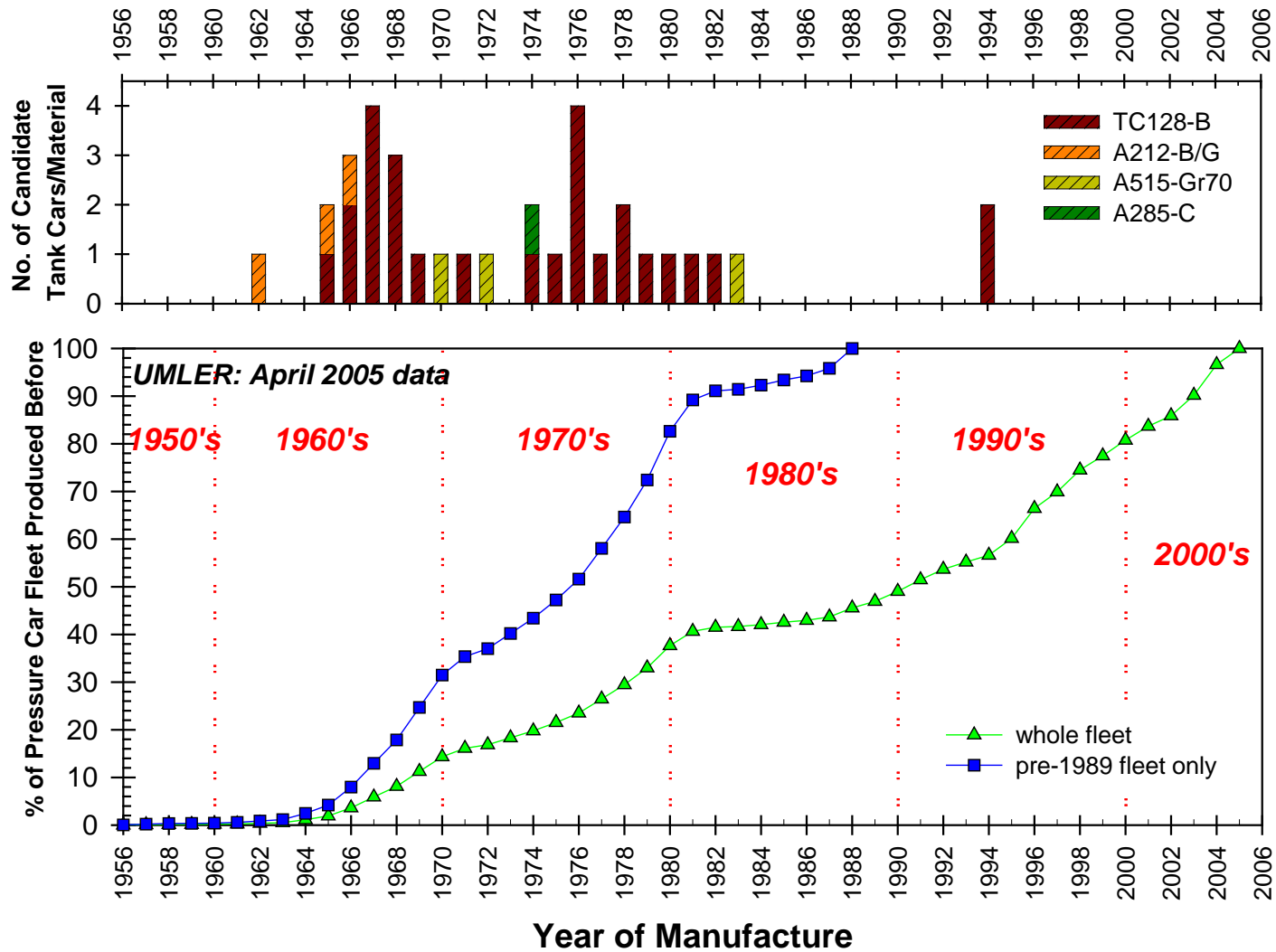


Figure 60. Cumulative Distribution of Pressure Tank Car Fleet and Tank Cars used for Testing

Tensile properties of interest were yield strength, ultimate strength, percent elongation at failure, and reduction of area. The gage length was generally 2 in, although material limitations occasionally required the use of sub-size specimens with smaller gage-lengths (1 in or 1.4 in). Tensile specimens were oriented transverse to the primary plate axis for the shell specimens. Head specimens were arbitrarily removed since the orientation of the plate prior to hot pressing the head was not known. Two replicate specimens were tested in all cases.

Tensile test measurements for TC-128B tank car steel are summarized in Table 19 in terms of the mean or average value and standard deviation. The table lists includes the number of test samples taken from the head and shell locations, *N*. For comparison, minimum requirements for TC-128B are listed in Table 20. In summary, 82 percent of the tested samples met the minimum requirement properties.

**Table 19. Summary of Tensile Test Measurements for TC-128B**

	<i>N</i>	Ultimate Tensile Strength (ksi)		Yield Strength (ksi)		Elongation (%)		Reduction in Area (%)	
		Mean	SD	Mean	SD	Mean	SD	Mean	SD
Head	42	87.7	5.23	62.3	4.01	29.2	2.76	62.1	4.35
Shell	80	89.3	7.36	60.5	7.66	24.8	2.95	50.2	4.91
H&S	122	88.8	6.61	61.1	6.67	26.3	3.58	54.3	7.39

**Table 20. Tensile Property Specifications for TC-128B**

Property	Allowable
Ultimate Tensile Strength	81 to 101 ksi
Yield Strength	Greater than 50 ksi
Elongation	Greater than 22%

Similarly CVN impact energies at three different temperatures are listed in Table 21. The relatively high values for standard deviation listed in the table indicate large scatter in impact energy for the range of temperatures.

**Table 21. Summary of CVN Impact Energies (ft-lb) at Three Temperatures**

	-50°F			0°F			50°F		
	<i>N</i>	Mean	SD	<i>N</i>	Mean	SD	<i>N</i>	Mean	SD
Head	36	16.9	10.92	45	35.5	20.72	36	54.4	30.35
Shell	74	6.3	4.59	96	12.5	6.78	74	21.0	9.39
H&S	110	9.8	8.79	141	19.9	16.80	110	31.9	24.54

Figure 61 compares CVN data from tank cars involved in three different accidents: three cars from Minot (GATX 47814, GATX 47837, and GATX 47982), one car from Graniteville (UTLX 900270), and one car from Macdona (ACFX 86305). The Charpy tests were conducted on material extracted from the shells of the tank cars. The Charpy test specimens were oriented in the transverse direction. The figure also shows measurements made by SwRI [40] (represented by the open symbols in the figure) and by NTSB [41] (solid symbols) for the three cars involved in the Minot accident. The SwRI measurements were all taken at 0°F, while the NTSB data cover a range of temperatures. Regression curves are fit to the NTSB data. The figure shows significant scatter among different cars. Moreover, the figure also shows inherent scatter associated with CVN impact energy as a measure of impact resistance, as characterized by the error bars for measurements at the same temperature.

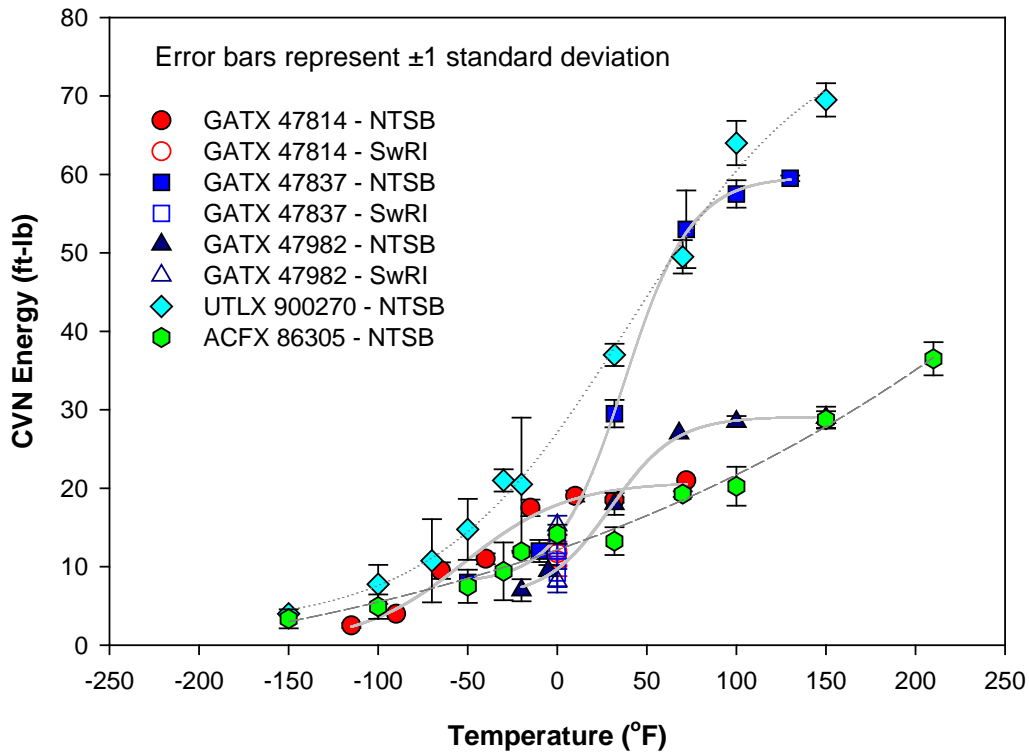


**Figure 61. CVN Data for Cars Involved in Three Different Accidents**

## 4.2 High-Rate Fracture Toughness

Toughness is a term that is loosely used to characterize the resistance to failure of metal with a sharp crack, notch, or similar stress concentrator. Moreover high values of toughness are generally recognized as a desirable property for structural steel.

The word ‘toughness’ is used for two separate quantities: impact toughness and fracture toughness. Impact toughness is an energy measurement (e.g., Joules or ft-lb) which is commonly obtained from the CVN test. Fracture toughness is a calculated value for the critical stress intensity factor (in units of MPa- $\sqrt{m}$  or ksi- $\sqrt{\text{inch}}$ ) based on standard tests. Relationships between these quantities are empirical. The relationships have been validated over many years for structural steels in moderate section thickness. This has permitted the more readily available Charpy impact data to be used as an indicator to the adequacy of the fracture toughness. The widespread use of the CVN test stems from economics—it is the least expensive compared to other tests. But the conversion from Charpy impact energy to fracture toughness is somewhat problematic because the CVN test uses a specimen that contains a blunt notch rather than a sharp crack.

Fracture toughness changes with temperature—as temperature decreases, steel becomes more brittle and is more susceptible to fracture. Such changes occur gradually over a range of temperature. The temperature at which the fracture behavior of steel changes from ductile to brittle is called the ductile-to-brittle transition temperature. The transition temperature for normalized steel is lower than that of non-normalized steel.

AAR Specification M-1002 requires that heads and shells of all pressure tank cars built after January 1, 1989, must be constructed of normalized steel. Normalization is a heat treating process that produces a finer and more abundant pearlitic microstructure, which is intended to make the steel stronger and harder compared to non-normalized steel.

Fracture toughness is also affected by loading rate—as the rate of loading or strain rate increases, steel becomes more susceptible to fracture. Performing a fracture mechanics test at relatively high loading rates rather than a CVN test is intended to provide a more realistic assessment of impact resistance. Moreover, measurement of high-rate fracture toughness in tank car steels has been limited to those conducted previously by SwRI in litigation support for GATX (e.g., [39] and [40]).

The tests performed by SwRI did not adhere precisely to ASTM standards for fracture toughness<sup>5</sup> due to inherent circumstances. For example, the material obtained for the testing program is thinner than what is typically considered for plane-strain conditions. In addition, since the material was obtained from tank cars, it is curved, which limits the size of the test specimens. Finally, testing is performed at both low temperature and high loading rate with strain rates on the order of 5 inch per inch per second, which has serious implications with regard to transducer performance and data integrity. For example,

---

<sup>5</sup> For example, ASTM E399: “Standard Test Method for Linear-Elastic Plane-Strain Fracture Toughness  $K_{IC}$  of Metallic Materials,” and ASTM E1820, “Standard Test Method for Measurement of Fracture Toughness,” addendum for Rapid Loading Fracture Toughness Determination.

applying the method described in ASTM E1820 requires highly accurate crack extension measurements which are not practical when the time to peak load is on the order of 1/1000th of a second.

A consequence of the somewhat nonstandard testing procedure adopted by SwRI is that fracture toughness is reported in terms of  $K_{max}$  (maximum stress intensity factor calculated using peak load observed in the fracture test) rather than  $K_{IC}$  (plane-strain fracture toughness calculated using procedures in ASTM E399). The merits of applying this so-called  $K_{max}$  approach are discussed in detail in the technical report prepared by SwRI [38].

A framework for interpreting fracture toughness values was developed previously by Anderson and McKeighan [42]. Classifications for different values of fracture toughness obtained from the  $K_{max}$  approach were defined as follows:

- |  |                     |
|--|---------------------|
| • Less than 50 ksi- $\sqrt{\text{in}}$     | Poor toughness      |
| • 50 – 100 ksi- $\sqrt{\text{in}}$         | Adequate toughness  |
| • 100 – 200 ksi- $\sqrt{\text{in}}$        | Good toughness      |
| • Greater than 200 ksi- $\sqrt{\text{in}}$ | Excellent toughness |

The vast majority of material in the testing program fell into the adequate or good category. A limited number of samples fell into the poor category, but were confined to the lowest temperature results ( $-50^{\circ}\text{F}$ ).

Table 22 summarizes the high-rate fracture toughness tests conducted on TC-128B tank car steel obtained from retired cars built prior to 1989. The table lists the number of tests, average or mean value, and standard deviation at the two test temperatures ( $-50^{\circ}\text{F}$  and  $0^{\circ}\text{F}$ ) for material taken from the head and the shell of the retired cars. For instance, 51 tests were performed on shell material; 24 tests on material from heads. The statistics are based  $K_{max}$  measurements reported by McKeighan [38]. The average fracture toughness for the head material is generally higher than that for the shell. In addition, average fracture toughness values for both head and shell material decrease with lower temperature. The standard deviation indicates the variability in the data.

Similarly, Table 23 summarizes the high-rate fracture toughness data from six cars involved in the Minot accident, each of which was also built prior to 1989. The material in these tests was also TC-128B, and was obtained from the shells of the tank cars. The statistics are based on  $K_{max}$  measurements conducted as part of litigation support for GATX [40]. The trend of decreasing fracture toughness with temperature is evident again in these data. The average fracture toughness at  $0^{\circ}\text{F}$  is slightly higher for the Minot cars than for the retired cars. In addition, the standard deviations for the Minot cars are slightly less than those for the retired cars, indicating less scatter in the data.

**Table 22. Summary of High-Rate Fracture Toughness Data for Retired Cars**

	Temperature (°F)	Number of tests	Average (ksi-√in)	Standard Deviation (ksi-√in)
Shell	-50	16	53.8	17.8
	0	35	82.1	22.6
Head	-50	8	73.5	24.2
	0	16	98.8	25.4

**Table 23. Summary of High-Rate Fracture Toughness Data from Minot Cars**

Temperature (°F)	Number of tests	Average (ksi-√in)	Standard Deviation (ksi-√in)
0	13	90.6	17.2
37	21	98.7	10.7

Fracture toughness data for steels tend to be highly scattered, especially in the ductile-to-brittle transition region. The SwRI high-rate fracture toughness data confirms this tendency. Two methods to quantify scatter in fracture toughness data have been developed previously, and are described briefly as follows.

- 1) *Master Curve Method*—ASTM standard E1921-03 [43] describes a methodology<sup>6</sup> to account for scatter in fracture toughness data in the ductile-to-brittle transition region, which is based on two general observations:
  - (a) Scatter in fracture toughness data in the transition region follows a characteristic statistical distribution that is the same for all ferritic steels, and
  - (b) The shape of the fracture toughness versus temperature curve in the transition range is virtually identical for all ferritic steels. The only difference between steels is the absolute position of the curve on the temperature axis.
 In this methodology, fracture toughness data are assumed to vary according to a Weibull distribution function.
- 2) *Basis Tolerance Limits* [45]—Statistical tolerance limits provide a range in which some percentage of a sample population will lie. In quality control applications, the extreme (lower) percentile of the distribution is targeted as the tolerance limit. For example, a tolerance limit called the B-basis is defined as the value at which 10 percent of the total population will lie below with a 95 percent confidence level. A more stringent tolerance limit is the A-basis, which is the value at which 1 percent of the total population will lie below at 95 percent confidence level.

<sup>6</sup> The master curve method has been used to establish fracture toughness requirements for crack initiation and crack arrest conditions in nuclear reactor pressure vessel steels [44].

The procedures to calculate A- and B-basis values depend on the assumed statistical distribution function and sample size.

Figure 62 shows results from applying these two methods to the SwRI fracture toughness ( $K_{max}$ ) data from the shells of retired cars made from TC-128B. Fracture toughness data for the two different temperatures are included to show the extent of scatter. The figure shows three curves estimated from applying the master curve method: the dotted curve labeled  $K_{max(0.90)}$  represents 90th percentile or upper bound, the solid curve labeled  $K_{max(0.50)}$  represents the median or 50th percentile curve, and the dashed curve labeled  $K_{max(0.10)}$  represents 10th percentile or lower bound of the data. The fracture toughness master curves were generated from applying procedures described by McCabe et al. [44], but without censoring the data.<sup>7</sup> Nonparametric B-basis values<sup>8</sup> for the two test temperatures are also shown in the figure for comparison, which are less than the 10th percentile values calculated from the master curve method.

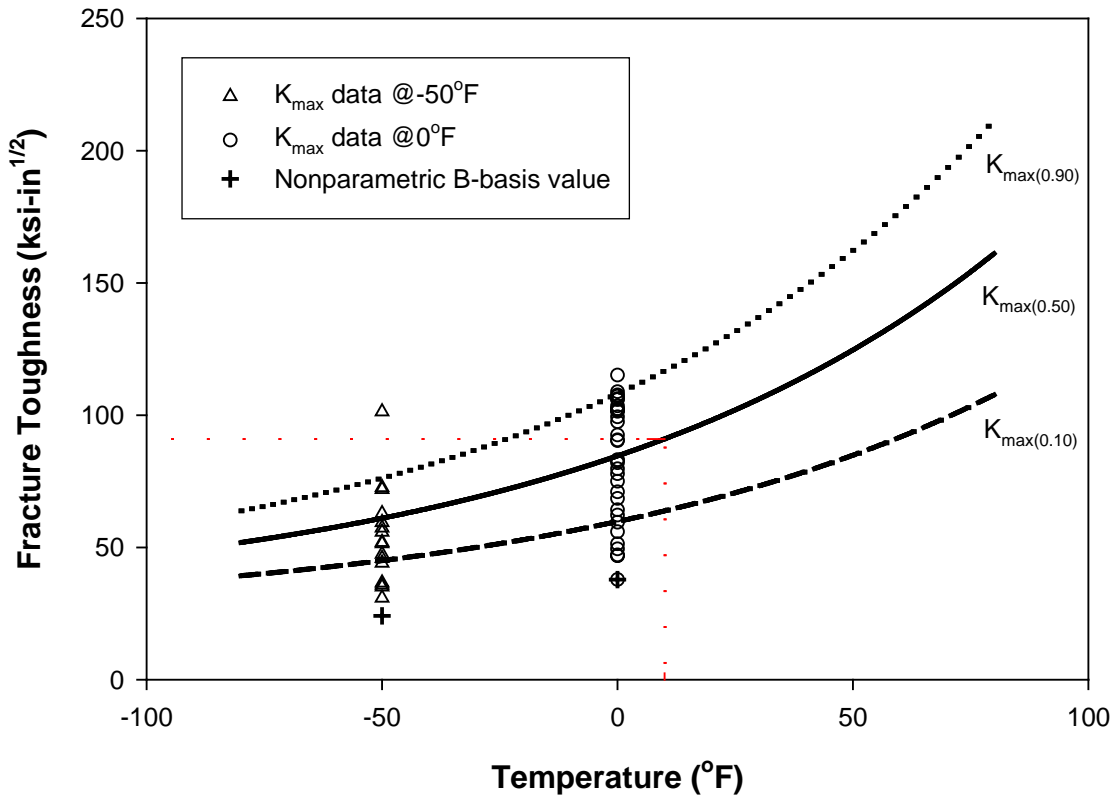


**Figure 62. Fracture Toughness Master Curve Applied to Shell Data from Retired Cars**

<sup>7</sup> The data should be censored to exclude tests in which evidence exists of significant ductile tearing [46].

<sup>8</sup> Nonparametric means that no statistical distribution function was assumed.

Similarly Figure 63 shows the results from applying the master curve method and estimating the basis tolerance limits to  $K_{max}$  data from the shells of Minot cars made from TC-128B tank car steel. The variability or scatter appears to reduce with increased temperature. The master curves for the Minot cars are shifted toward the right on the temperature scale compared to those for retired cars. The shift in temperature is reflected through the reference temperature, which by definition is the temperature at which the median fracture toughness is equal to 100 MPa- $\sqrt{m}$  or 91 ksi- $\sqrt{in}$ .

Table 24 lists the reference temperatures for the two sets of data as estimated by the master curve method. Generally speaking, high toughness steels have a low reference temperature and low toughness steels have a high reference temperature. Moreover, the basic premise of the master curve method is that a wide range of ferritic steels fit one universal curve for toughness as a function of temperature, and the only difference between different grades and heats of steels is the absolute position of the curve with respect to temperature.

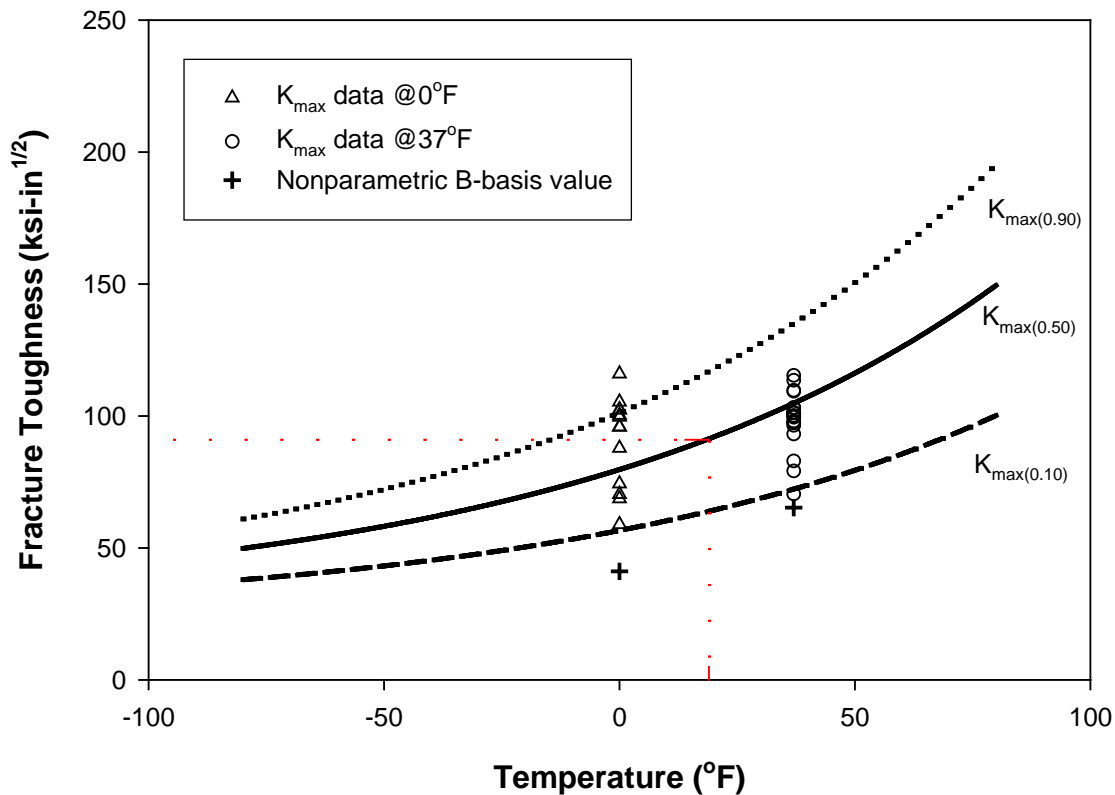


**Figure 63. Fracture Toughness Master Curve Applied to Shell Data from Minot Cars**

**Table 24. Estimated Reference Temperatures**

	$T_o$ (°F)
Retired Cars Only	10.0
Minot Cars Only	19.0

Table 25 lists the tolerance limits estimated for high-rate fracture toughness based on the data from the retired cars and the Minot cars. The 10th percentile limit is calculated using the master curve method. Procedures to calculate the B-basis depend on the assumed statistical distribution function and sample size. The B-basis values shown in the two previous figures are calculated assuming nonparametric statistics using the Hanson-Koopmans method [47]. Except for the retired cars at  $-50^{\circ}\text{F}$ , the nonparametric B-basis value is the most conservative (i.e., pessimistic or worst case) tolerance limit. Moreover, in two previous figures, the test data lie above or close to the nonparametric B-basis tolerance limit, and some of the data lie below the 10th percentile curve from the master curve method.

**Table 25. Estimated Tolerance Limits for High-Rate Fracture Toughness (in  $\text{ksi}\sqrt{\text{in}}$ )**

	Retired Cars		Minot Cars	
	$-50^{\circ}\text{F}$	$0^{\circ}\text{F}$	$0^{\circ}\text{F}$	$37^{\circ}\text{F}$
10 <sup>th</sup> percentile	45.0	59.8	56.5	72.2
Normal B-basis	17.5	42.9	53.6	78.4
Lognormal B-basis	27.2	46.0	57.2	78.7
Weibull B-basis	18.8	45.3	54.7	77.6
Nonparametric B-basis	24.1	37.8	41.1	65.2

Figure 64 shows the test data from the retired cars plotted as high-rate fracture toughness ( $K_{\text{max}}$ ) as a function of CVN energy at a temperature of  $0^{\circ}\text{F}$ . The error bars represent variability in the measurements in terms of one standard deviation above and below the mean value. The figure also shows the Roberts-Newton equation, which is assumed to be a lower-bound relation for CVN energy and fracture toughness [48]. Similarly, Figure 65 shows measurements of high-rate fracture toughness as a function of CVN energy at a temperature of  $-50^{\circ}\text{F}$ . Except for a few outliers, the test data lie above the Roberts-Newton equation. In two of the outliers, the variability in both CVN energy and measured fracture toughness was quite large in comparison to the other data. Moreover, it appears that Roberts-Newton equation provides a reasonable lower-bound relationship between CVN energy and  $K_{\text{max}}$  for non-normalized TC-128B tank car steel.

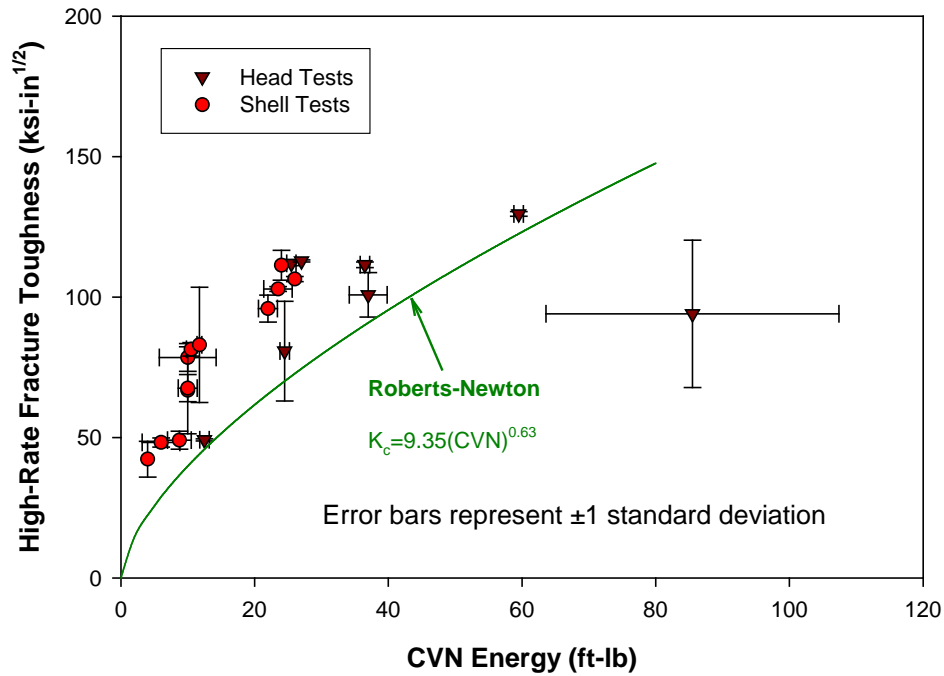
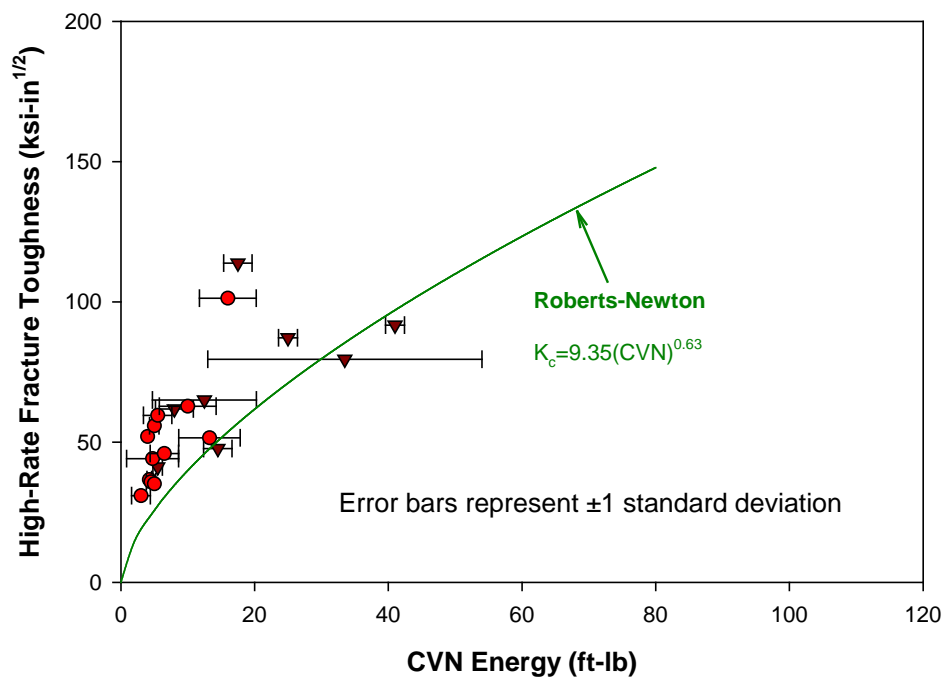


Figure 64. High-Rate Fracture Toughness as a Function of CVN Energy at 0°F



**Figure 65. High-Rate Fracture Toughness as a Function of CVN Energy at  $-50^{\circ}\text{F}$**

### **4.3 Pendulum Impact Testing of Bulk Fracture Behavior**

Standard tests for toughness contain stress concentrations (e.g., a blunt notch in the Charpy test and a sharp crack in the ASTM fracture mechanics tests) to ensure that material failure will initiate and propagate. In a structure without preexisting stress raisers, the mechanics of material failure under impact loading conditions are not well understood. Moreover, the meaning of fracture toughness in a structure without a preexisting crack is unclear.

A nonstandard pendulum impact test was developed to measure the energy to fracture unnotched Charpy specimens. An oversized pendulum test fixture, BFCM, was built by SwRI to accommodate the energy levels needed to break the unnotched specimens (Figure 66). The measurement of fracture energy was used to assess puncture resistance.



**Figure 66. Oversized, Nonstandard Pendulum Impactor**

Figure 67 shows a drawing of BFCM test specimen. The trapezoidal ends of the specimen self-engage into the test fixture so they are held fixed as the impact load is applied through the pendulum. In this drawing, the test section is 6-inches long, and the specimen width is 1 in. Two impact tups were used in the tests: a blunt tup with a 0.5-inch wide contact surface and a sharp tup with a 0.125-inch wide contact surface. Figure 68 shows the dimensions of the two impact tups.

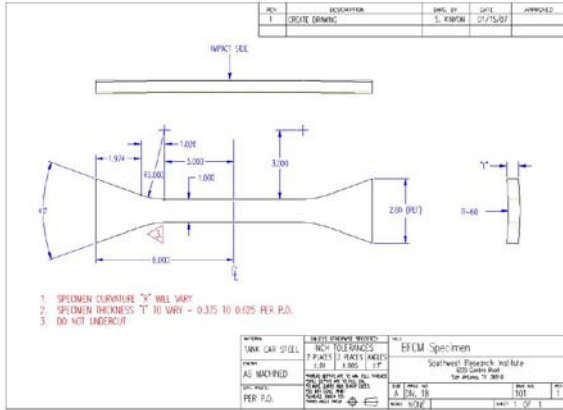
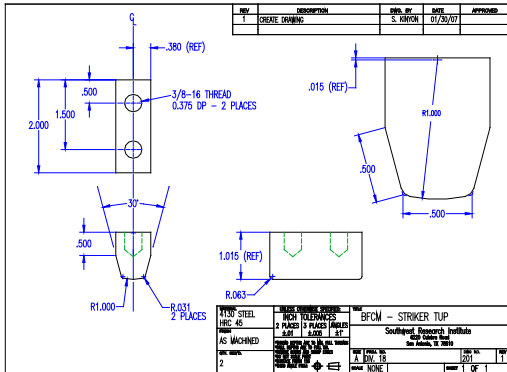
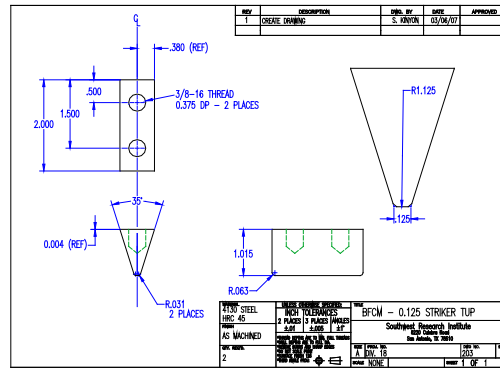


Figure 67: BFCM Test Specimen



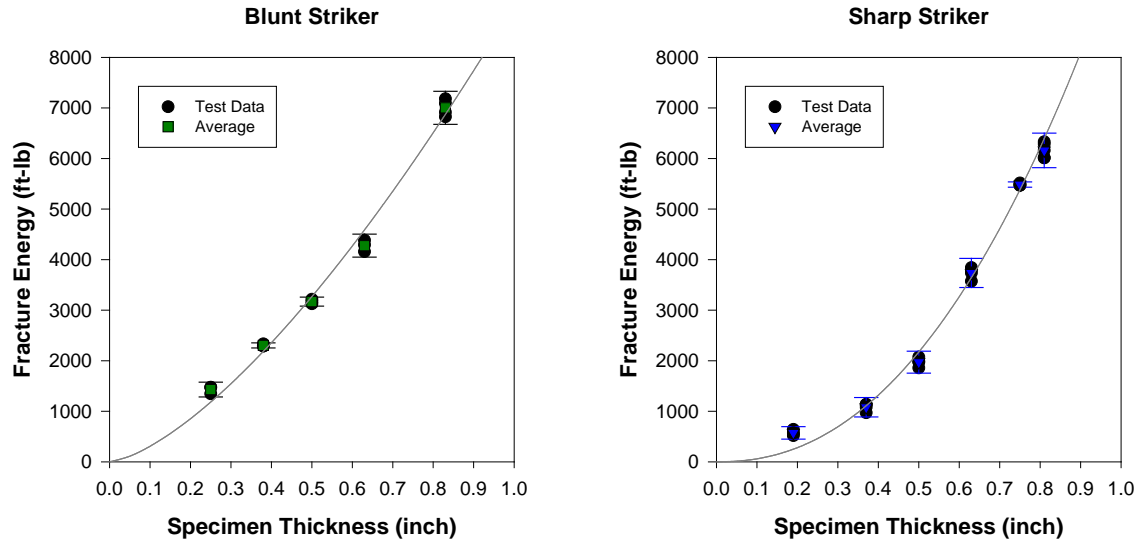
(a) Blunt Tip



(b) Sharp Tip

Figure 68. Impact Tups Used in BFCM Tests

Figure 69 shows data from the BFCM tests conducted on specimens made from normalized TC-128B tank car steel with varying thicknesses and using the two different strikers or tups. The figure also shows regression curves of the test data for the two different tups. The error bars represent variability in the test measurements for fracture energy in terms of two standard deviations above and below the average for a given specimen thickness. The data in the figure indicates that more energy is required to fracture an unnotched specimen with the blunt tup than with the sharp tup. The data can be used to validate potential material failure criteria that are incorporated into finite element analysis to examine tank integrity.



Error bars represent  $\pm 2$  standard deviations. Nominal specimen width is 1.0 inch

**Figure 69. Fracture Energies for TC-128B Measured in BFCM Tests**

#### 4.4 Discussion and Summary

The results of the fracture toughness tests are scattered by a factor of about four. This would require a safety factor of at least two in a quality assurance (QA) specification. In other words, the samples taken from a production heat would have to average at least twice the toughness required for service.

At present, the cause of the scatter is unknown. If it is the test protocol, then a better procedure might reduce the scatter enough to allow a more reasonable safety factor in a QA specification. However, inherent material variability might be the cause of the scatter. In the latter case, it is doubtful that a workable QA specification could be devised, for two reasons.

First, the performance goal may require a very expensive material. Alternatively, an unacceptable gain in structure weight may be required in order to decrease applied stresses enough to meet the safety factor with achievable material performance.

Second, the specification does not provide an absolute safety guarantee because some small percentage of the material might not have the minimum necessary toughness. For example, even an A-basis specification (no more than one percent below minimum) leaves the risk that one thousand cars in a fleet of one hundred thousand might have insufficient toughness. Also a subtle potential for error exists in the specification itself. A- and B-basis values are usually derived from given numbers of samples, without regard to the relation between sample and production volume. There is no problem when the samples are items such as light bulbs—one sample “volume” is the same as one

production “volume.” However, using a few samples to measure the toughness of a heat of steel is equivalent to testing on the order of one ten-thousandth of the material volume. One must question whether an A- or B-basis derived from such tests reflects the true scatter in performance.

The large scatter observed in the high-rate fracture toughness measurements makes it unlikely that a practical specification of minimum fracture toughness can be devised to guarantee the prevention of unstable fracture in railroad tank cars subject to derailment forces. A specification of average fracture toughness is possible and could serve to decrease the population of cars at risk of fracture.

With respect to the pressure tank car fleet as a whole, the cold weather risk associated with non-normalized tank car steel may be mitigated by taking some combination of any of the following actions on such cars: (1) retire early, (2) reconfigure for non-hazardous/non-pressure commodities, and (3) transfer to service on exclusively southern routes.

## 5. Conclusions

This report describes engineering studies conducted and managed by the Volpe Center on the structural integrity of railroad tank cars under accident loading conditions. The following conclusions are made based upon the results to date.

### *Derailment Dynamics*

The lumped-parameter models developed to examine the gross motions of rail cars in a generalized train derailment were verified through various comparisons.

- (1) The similarity of results from the purpose-built and ADAMS models suggests that the dynamics are being correctly calculated for the assumed scenarios in both models.
- (2) The purpose-built and ADAMS models produce similar results to those from a simulation model developed previously. The previous model reproduced the number of derailed cars in an actual derailment.

Sensitivity studies using the derailment dynamics models indicate that train speed and friction have the most significant effect on the derailment outcome in terms of either the number of derailed cars, maximum closing speed, or peak coupler force.

For flat terrain and train speeds not exceeding roughly 40 mph, the maximum closing speeds between cars engaging in post-derailment collisions appear to average about one-half the initial train speed.

The derailment dynamics models produce simulated car-to-car impacts that generally occur in accidents and lead to release of lading; namely, head and shell impacts. Moreover, the simulated car-to-car impacts are useful to represent idealized scenarios that can be analyzed for performance evaluations.

### *Structural Response*

The nonlinear (i.e., elastic-plastic material behavior with large deformations) FEA models developed to examine the structural response (i.e., force-indentation behavior) for head and shell deformations were also verified through various comparisons.

- (1) The force-indentation behavior calculated by static, nonlinear FEA for head and shell deformations are in reasonable agreement with closed-form solutions.
- (2) Static and dynamic, nonlinear FEA models produce nearly identical force-indentation characteristics.
- (3) Dynamic, nonlinear FEA, and lumped-parameter models produce nearly identical results for impact force as a function of closing speed.

Dynamic, nonlinear FEA models for shell impacts with fluid-structure interaction were validated with data obtained from full-scale tank car tests:

- (1) Calculated peak impact forces are within 10 percent of test data, and maximum indentations are within 15 to 20 percent.

(2) Puncture in the second full-scale shell impact test was predicted using a material failure criterion based on the general state of stress in the shell, or stress triaxiality.

Based on comparisons between FEA and full-scale shell impact test data, peak impact forces and maximum indentations depend on impact speed. In addition, indenter size appears to have a relatively weak effect on the force-indentation characteristic, but a strong effect on puncture.

Elastic-plastic FEA of unnotched Charpy specimens made from different tank car steels provided a benchmark case to examine material failure criteria. FEA used in conjunction with a criterion based on the general state of stress in terms of stress triaxiality (i.e., Bao-Wierzbicki [25]) were in excellent agreement with measured fracture energies.

Finite element procedures will remain useful for predicting structural response of any new car designs that might differ from current practice. Research employing these procedures is ongoing to develop alternative or improved designs for tank cars carrying hazardous materials [49] and [50].

#### *Tank Car Steels Characterization*

No clear trends were observed between chemical composition, tensile properties, Charpy impact energies, or fracture toughness values and tank car build date.

The extent of scatter observed in the measurements of fracture toughness was quite large, which obscures making definitive conclusions regarding toughness variation with age.

The large scatter makes it is unlikely that a practical specification of minimum fracture toughness can be devised to guarantee the prevention of unstable fracture in railroad tank cars subject to derailment forces. A specification of average fracture toughness is possible and could serve to decrease the population of cars at risk of fracture.

## 6. References

- [1] Treichel, T., "List of Accident-Caused Releases of Toxic Inhalation Hazard (TIH) Materials from Tank Cars, 1965-2005," RSI-AAR Railroad Tank Car Safety Research and Test Project, Report No. RA 06-05, June 2006.
- [2] National Transportation Safety Board, "Derailment of Canadian Pacific Railway Freight Train 292-16 and Subsequent Release of Anhydrous Ammonia Near Minot, North Dakota January 18, 2002," Railroad Accident Report NTSB/RAR-04/01, March 2004.
- [3] National Transportation Safety Board, "Collision of Union Pacific Railroad Train MHOTU-23 With BNSF Railway Company Train MEAP-TUL-126-D With Subsequent Derailment and Hazardous Materials Release, Macdona, Texas, June 28, 2004" Railroad Accident Report NTSB/RAR-06/03, July 2006.
- [4] National Transportation Safety Board, "Collision of Norfolk Southern Freight Train 192 With Standing Norfolk Southern Local Train P22 With Subsequent Hazardous Materials Release at Graniteville, South Carolina January 6, 2005," Railroad Accident Report NTSB/RAR-05/04, November 2005.
- [5] Tyrell, D.C., Jeong, D.Y., Jacobsen, K., Martinez, E., "Improved Tank Car Safety Research," *Proceedings of the 2007 ASME Rail Transportation Division Fall Technical Conference*, RTDF2007-46013, September 2007.
- [6] Yang, T.H., Manos, W.B., Johnstone, B., "Dynamic Analysis of Train Derailments," *ASME Winter Annual Meeting*, ASME Paper 72-WA/RT-5, 1972.
- [7] Birk, A.M., Anderson, R.J., Coppens, A.J., "Computer Simulation of a Derailment Accident, Part I – Model Basis," *Journal of Hazardous Materials* 25, pp. 121-147, 1990.
- [8] Birk, A.M., Anderson, R.J., Coppens, A.J., "Computer Simulation of a Derailment Accident, Part II – Sample Simulation," *Journal of Hazardous Materials* 25, pp. 149-165, 1990.
- [9] Toma, E.E., "A Computer Model of a Train Derailment," Ph.D. Thesis, Kingston, Ontario, Canada: Department of Mechanical Engineering, Queen's University, 1998.
- [10] Han, H.S., Koo, J.S., "Simulation of Train Crash in Three Dimensions," *Vehicle System Dynamics* 20, pp. 435-450, 2003.
- [11] Jeong, D.Y., Lyons, M.L., Orringer, O., Perlman, A.B., "Equations of Motion for Train Derailments," *Proceedings of the 2007 ASME Rail Transportation Division Fall Technical Conference*, RTDF2007-46009, September 2007.

- [12] Paetsch, C.R., Perlman, A.B., Jeong, D.Y., “Dynamics Simulation of Train Derailments,” *Proceedings of 2006 ASME International Mechanical Engineering Congress and Exposition*, IMECE2006-14607, November 2006.
- [13] Grange, J.S., *Report of the Mississauga Railway Accident Inquiry*, Hull, Quebec: Canadian Government Publishing Centre, 1981.
- [14] *LS-DYNA3D User’s Manual, Version 940*, Livermore, CA: Livermore Software Technology Company.
- [15] *ABAQUS User’s Manual*, Pawtucket, RI: Hibbit, Karlsson & Sorensen Inc.
- [16] Cook, R.D., Malkus, D.S., Plesha, M.E., *Concepts and Applications of Finite Element Analysis*, 3rd Ed., New York, NY: John Wiley & Sons, 1989.
- [17] Roache, P.J., *Verification and Validation of Computational Science and Engineering*, Albuquerque, NM, Hermosa Publishers, 1998.
- [18] American Society of Mechanical Engineers, “Guide for Verification and Validation in Computational Solid Mechanics,” ASME V&V 10-2006, New York, NY, December 2006.
- [19] Phillips, E.A., Olsen, L., “Final Phase 05 Report on Tank Car Head Study,” RPI-AAR Tank Car Safety Research and Test Project, Report No. RA-05-1-17, July 1972.
- [20] Tang, Y.H., Yu, H., Gordon, J.E., Priante, M., Jeong, D.Y., Tyrell, D.C., Perlman, A.B., “Analyses of Full-Scale Tank Car Shell Impact Tests,” *Proceedings of the 2007 ASME Rail Transportation Division Fall Technical Conference*, RTDF2007-46010, September 2007.
- [21] de Oliveria, J.G., Weirzbicki, T., “Crushing Analysis of Rotationally Symmetric Plastic Shells,” *Journal of Strain Analysis for Engineering Design* 17, pp. 229-23, 1982.
- [22] Riks, E., “An Incremental Approach to the Solution of Snapping and Buckling Problems,” *International Journal of Solids and Structures* 15, pp. 524-551, 1979.
- [23] Wierzbicki, T., Suh, M.S., “Indentation of Tubes Under Combined Loading,” *International Journal of Mechanical Sciences* 30, pp. 229-248, 1988.
- [24] Jeong, D.Y., Tang, Y.H., Yu, H., Perlman, A.B., “Engineering Analyses for Railroad Tank Car Head Puncture Resistance,” *Proceedings of 2006 ASME International Mechanical Engineering Congress and Exposition*, IMECE2006-13212, September 2006.

- [25] Bao, Y., Wierzbicki, T., "On fracture locus in the equivalent strain and stress triaxiality space," *International Journal of Mechanical Sciences* 46, pp. 81-98, 2004.
- [26] Yu, H., Jeong, D.Y., Gordon, J.E., Tang, Y.H., "Analysis of Impact Energy to Fracture Unnotched Charpy Specimens Made from Railroad Tank Car Steel," *Proceedings of the 2007 ASME Rail Transportation Division Fall Technical Conference*, RTDF2007-46038, September 2007.
- [27] Gurson, A.L., "Continuum Theory of Ductile Rupture by Void Nucleation and Growth: Part 1 – Yield Criterion and Flow Rules for Porous Ductile Media," *Journal of Engineering Materials and Technology* 99, pp. 2-15, 1977.
- [28] Tvergaard, V., "Influence of Voids on Shear Band Instabilities under Plane Strain Conditions," *International Journal of Fracture* 17, pp. 389-407, 1981.
- [29] Tvergaard, V., "On Localization in Ductile Materials Containing Spherical Voids," *International Journal of Fracture* 18, pp. 237-252, 1982.
- [30] Anderson, T.L., Kirkpatrick, S.W., "Quantifying and Enhancing Puncture Resistance in Railroad Tank Cars Carrying Hazardous Materials, Phase I: Preliminary Study," Structural Reliability Technology, Inc. Draft Report Prepared for The Chlorine Institute, 2006.
- [31] Anderson, T.L., Rose, B., McKeighan, P.C., Kirkpatrick, S.W., "Quantifying and Enhancing Puncture Resistance in Railroad Tank Cars Carrying Hazardous Materials, Phase II: Development and Validation of a Puncture Resistance Evaluation Methodology," Quest Reliability LLC Draft Report Prepared for The Chlorine Institute, 2007.
- [32] Bao, Y., Wierzbicki, T., "Determination of Fracture Locus for the 2024-T351 Aluminum," Impact & Crashworthiness Laboratory, Massachusetts Institute of Technology, Report No. 81, 2002.
- [33] Bao, Y., Bai, Y., Wierzbicki, T., "Calibration of A710 Steel for Fracture," Impact & Crashworthiness Laboratory, Massachusetts Institute of Technology, Report No. 135, 2004.
- [34] Lee, Y.W., Wierzbicki, T., "Quick Calibration for Industrial Use," Impact & Crashworthiness Laboratory, Massachusetts Institute of Technology, Report No. 115, 2004.
- [35] Hillerborg, A., Modeer, M., Petersson, P.E., "Analysis of crack formation and crack growth in concrete by means of fracture mechanics and finite elements," *Cement and Concrete Research* 6, 1976, pp. 773-782.

- [36] Thilmann, T., "Tying Two Forces," *Mechanical Engineering* 129, New York: American Society of Mechanical Engineers, May 2007: 34-37.
- [37] Tang, Y.H., Yu, H., Gordon, J.E., Jeong, D.Y., Perlman, A.B. "Analysis of Railroad Tank Car Shell Impacts Using Finite Element Method," *Proceedings of the 2008 IEEE/ASME Joint Rail Conference*, JRC2008-63014, April 2008.
- [38] McKeighan, P.C., "Mechanical Properties of Tank Car Steels Retired from the Fleet," Southwest Research Institute Report to the Volpe Center, August 2008.
- [39] McKeighan, P.C., "High Rate Fracture Toughness, Tensile Properties, CVN and Composition of Various TC-128B Steels, Phase A: Pre-1989 GATX Tank Cars and Modern Vintage Plate," Interim Report, Southwest Research Institute Project No. 18.11388, June 2005.
- [40] McKeighan, P.C., "High Rate Fracture Toughness, Tensile Properties, CVN and Composition of Various TC-128B Steels, Phase B: Tank Cars Involved in the 2002 Minot Incident," Interim Report, Southwest Research Institute Project No. 18.11388, June 2005.
- [41] National Transportation Safety Board, Materials Laboratory Factual Report, Report No. 03-042, April 2003.
- [42] Anderson, T.L., McKeighan, P.C., "The Interpretation of Fracture Toughness Magnitudes for Tank Car Steels: Relating K-based Toughness Range to Material Adequacy," August 2005.
- [43] ASTM Standard E1921-03, "Standard Test Method for Determination of Reference Temperature,  $T_o$ , for Ferritic Steels in the Transition Range," *Annual Book of ASTM Standards*, Vol. 03.01, West Conshohocken, PA: ASTM International, 1998.
- [44] McCabe, D.E., Merkle, J.G., Wallin, K., *Introduction to the Development and Use of the Master Curve Method*, West Conshohocken, PA: ASTM International, 2005.
- [45] Department of Defense, "Metallic Materials and Elements for Aerospace Vehicle Structures," Department of Defense Handbook, MIL-HDBK-5J, 2003.
- [46] E-mail communication with T.L. Anderson.
- [47] Hanson, D.L., Koopmans, L.H., "Tolerance Limits for the Class of Distribution with Increasing Hazard Rates," *Annals of Mathematical Statistics* 35, pp. 1561-1570, 1964.

- [48] Barsom, J.M., Rolfe, S.T., *Fracture and Fatigue Control in Structures: Applications of Fracture Mechanics*, 3rd ed. West Conshohocken, PA: ASTM International, 1999; 126.
- [49] Tyrell, D.C., Jacobsen, K., Talamini, B., Carolan, M., “Developing Strategies for Maintaining Tank Car Integrity During Train Accidents,” *Proceedings of the 2007 ASME Rail Transportation Division Fall Technical Conference*, RTDF2007-46015, September 2007.
- [50] Carolan, M., Talamini, B., Tyrell, D.C., “Update on Ongoing Tank Car Crashworthiness Research: Predicted Performance and Fabrication Approach,” *Proceedings of the 2008 IEEE/ASME Joint Rail Conference*, JRC2008-63052, April 2008.

## **APPENDIX A - NTSB RECOMMENDATIONS FROM THE MINOT ACCIDENT**

The NTSB released its accident report on the Minot derailment on March 15, 2004, and made the following recommendations to the FRA:

*Require all railroads with continuous welded rail track to include procedures (in the programs that are filed with the Federal Railroad Administration) that prescribe on-the-ground visual inspections and nondestructive testing techniques for identifying cracks in rail joint bars before they grow to critical size. (R-04-1)*

*Establish a program to periodically review continuous welded rail joint bar inspection data from railroads and Federal Railroad Administration track inspectors and, when determined necessary, require railroads to increase the frequency or improve the methods of inspection of joint bars in continuous welded rail. (R-04-2)*

*Instruct Federal Railroad Administration track inspectors to obtain copies of the most recent continuous welded rail programs of the railroads that fall within the inspectors' areas of responsibility and require that inspectors use those programs when conducting track inspections. (R-04-3)*

*Conduct a comprehensive analysis to determine the impact resistance of the steels in the shells of pressure tank cars constructed before 1989. At a minimum, the safety analysis should include the results of dynamic fracture toughness tests and/or the results of nondestructive testing techniques that provide information on material ductility and fracture toughness. The data should come from samples of steel from the tank shells from original manufacturing or from a statistically representative sampling of the shells of the pre-1989 pressure tank car fleet. (R-04-4)*

*Based on the results of the Federal Railroad Administration's comprehensive analysis to determine the impact resistance of the steels in the shells of pressure tank cars constructed before 1989, as addressed in Safety Recommendation R-04-4, establish a program to rank those cars according to their risk of catastrophic fracture and separation and implement measures to eliminate or mitigate this risk. This ranking should take into consideration operating temperatures, pressures, and maximum train speeds. (R-04-5)*

*Validate the predictive model the Federal Railroad Administration is developing to quantify the maximum dynamic forces acting on railroad tank cars under accident conditions. (R-04-6)*

*Develop and implement tank car design-specific fracture toughness standards, such as a minimum average Charpy value, for steels and other materials of construction for pressure tank cars used for the transportation of U.S. Department of Transportation class 2 hazardous materials, including those in low-temperature service. The performance criteria must apply to the material orientation with the minimum impact resistance and take into account the entire range of operating temperatures of the tank car. (R-04-7)*

## APPENDIX B – ESTIMATION OF SAMPLE SIZE AND CONFIDENCE LEVEL

Determining an appropriate sample size is affected by a number of factors, including the purpose of the study, population size, level of precision, level of confidence or risk, and degree of variability. One method is to use a formula for sample size for the mean:<sup>9</sup>

$$n = \left( \frac{z_{\alpha/2} \cdot \sigma}{E} \right)^2$$

where  $z_{\alpha/2}$  is the abscissa of the standard normal distribution curve that cuts off an area  $\alpha$  at the tail,  $\sigma$  is the standard deviation, and  $E$  is the desired level of precision. Table B.1 lists the values of  $z_{\alpha/2}$  depending on the level of confidence.

**Table B.1: Critical Values for Different Levels of Confidence**

<i>Level of Confidence</i>	$z_{\alpha/2}$
95%	1.96
90%	1.645
80%	1.282

This formula states that higher levels of confidence and greater precision require larger sample sizes. Table B.2 lists results from using this formula to estimate the minimum sample sizes at different levels of confidence and precision.

**Table B.2: Minimum Sample Sizes for Different Levels of Confidence and Precision**

<i>Level of Confidence</i>	$E = \sigma$	$E = 0.5\sigma$	$E = 0.25\sigma$
95%	4	16	62
90%	3	11	44
80%	2	7	27

For example, Table B.2 indicates that at least four samples are needed in order to achieve a 95% level of confidence that the average fracture toughness for a given population will be within one standard deviation. At least 16 samples are needed in order to achieve the same level of confidence that the average fracture toughness will be within one-half

<sup>9</sup> iSixSigma Staff. "How to Determine Sample Size, Determining Sample Size," *iSixSigma.com* (July 9, 2000). <http://www.isixsigma.com/library/content/c000709a.asp>

standard deviation. In this method, the sample size estimate is strongly influenced by the population variance.